ROLE OF SURFACE CHEMISTRY IN IMPROVING PERFORMANCES OF ELECTRONIC DEVICES

by

Bo Yuan

A dissertation submitted to the Faculty of the University of Delaware in partial fulfillment of the requirements for the degree of Doctor of Philosophy in Chemistry and Biochemistry

2017 Fall

© 2017 Bo Yuan
All Rights Reserved

ROLE OF SURFACE CHEMISTRY IN IMPROVING PERFORMANCES OF ELECTRONIC DEVICES

by

Bo Yuan

Approved: ____
Brian Bahnson, Ph.D.
Chair of the Department of Chemistry and Biochemistry

Approved: ____
George Watson, Ph.D.
Dean of the College of Arts and Sciences

Approved: ____
Ann L. Ardis, Ph.D.
Senior Vice Provost for Graduate and Professional Education

I certify that I have read this dissertation and that in my opinion it meets the academic and professional standard required by the University as a dissertation for the degree of Doctor of Philosophy.

Signed: ____

Robert L. Opila, Ph.D.
Professor in charge of dissertation

I certify that I have read this dissertation and that in my opinion it meets the academic and professional standard required by the University as a dissertation for the degree of Doctor of Philosophy.

Signed: ____

Sharon Neal, Ph.D.
Co-chair of dissertation committee

I certify that I have read this dissertation and that in my opinion it meets the academic and professional standard required by the University as a dissertation for the degree of Doctor of Philosophy.

Signed: ____

Murray Johnston, Ph.D.
Member of dissertation committee

I certify that I have read this dissertation and that in my opinion it meets the academic and professional standard required by the University as a dissertation for the degree of Doctor of Philosophy.

Signed: ____

Cecil Dybowski, Ph.D.
Member of dissertation committee

I certify that I have read this dissertation and that in my opinion it meets the academic and professional standard required by the University as a dissertation for the degree of Doctor of Philosophy.

Signed: ____

Venkateswara Pallem, Ph.D.
Member of dissertation committee

ACKNOWLEDGEMENTS

For me, this is definitely the most important and emotional part throughout writing of the dissertation. It is a great pleasure to acknowledge all my mentors, colleagues, friends and family who offered me endless support in the past four years. Without them, I would not be able to finish this dissertation.

First and foremost, I would like to express my deepest gratitude to my advisor Dr. Robert Opila. I am very blessed to have this privilege to work in his group. He is a true role model for me for his kindness, knowledge and enthusiasm. He is very supportive to the students and I appreciate all his contribution of times, ideas and funding support in my PhD pursuit. His mentorship undoubtedly guides and motivates me to become a better person in professional career.

I would also like to thank all my committee members: Dr. Murray Johnston, Dr. Cecil Dybowski, Dr. Sharon Neal and Dr. Venkat Pallem for their encouragement, valuable inputs and insightful comments during accomplishment of this dissertation.

I was fortunate to have many industry connections during my PhD. I want to thank Dr. Chen Xu for being my mentor when I interned in Bell Labs. My project would not be possible without his guidance. He led me to a whole new world of electronics reliability. I would also like to thank Debbie Fleming, Dr. Holly Robin, and Richard Popowich for their support in setting up experiments in the labs and kind invitation to their Bocce games! Special thanks also go to Dr. Sherwin Kahn and Dr. Marc Benowitz for their management support for the mixed flowing gas project.

I would like to send my sincere appreciation to my manger Dr. Venkat Pallem in American Air Liquide DRTC for his support in the atomic layer etching project. This opportunity has prepared me a professional career in the field of semiconductor fabrication and I truly appreciate it. I am also grateful to Dr. Xiangyu Guo, Dr. James Royer and Fran Kaiser for helping me set up the new etching tool. I was really frustrated at the beginning but eventually this experience turned out to be one of the greatest assets I gained from my PhD.

I would also like to thank my fellow groupmates: Kevin Jones, Meixi Chen, Xi Lin, James Hack, Abhishek Lyer and Zijian Wang. I really enjoyed all the fun times we spent in and out of the lab. And special thanks go to Kevin Jones for teaching me everything about XPS and Auger.

My time in UD has become so joyful and memorable because of my friends. I want to thank Chunting Zhang for her unconditional support. She is always there when I need her help. And I would like to specially thank Yuejun Yan. We always have good discussion in many topics and she is the one who encouraged me to look for new opportunities for the next stage of my life. I am lucky to meet all my friends in the US. I cannot name you all but you will always be remembered.

Lastly, I must thank my parents for their continuous support and encouragement. My father is now pursuing PhD at his 50s. His attitude and enthusiasm really inspired me. We were arguing about who will be the first Dr. Yuan in our family and I wish him the best in his pursuit of PhD ☺. My parents raised me with great love and I can never say enough how much I love them.

TABLE OF CONTENTS

LIST OF TABLES x
LIST OF FIGURES vi
ABSTRACT xv

Chapter

1. INTRODUCTION 1

  1.1 Surface Chemistry Analytical Techniques 1

    1.1.1 X-ray Photoelectron Spectroscopy 1
    1.1.2 Atomic Force Microscopy 3
    1.1.3 Scanning Electron Microscopy and Energy Dispersive X-ray Microscopy 4

  1.2 Fabrication Processes 5

    1.2.1 Deposition Methods 5
    1.2.2 Etching Methods 6
    1.2.3 Photolithography 8

  1.3 Dissertation Objective and Outline 10

2. OPTICAL PERFORMANCE: TANTALUM PENTOXIDE MOTH-EYE ANTIREFLECTION COATINGS IN TANDEM SOLAR CELLS ON SILICON. 11

  2.1 Introduction 11

    2.1.1 III-V Tandem Solar Cells on Si Substrate 11
    2.1.2 Objectives of Antireflection Coatings (ARCs) 13

      2.1.2.1 Introduction 13
      2.1.2.2 ARCs on III-V Tandem Cells 15

    2.1.3 Optical Modeling: Finite Difference Time Domain (FDTD) 16

  2.2 Experimental Methods: Fabrication of Moth-eye Nanostructures 17

2.3 Experimental Results and Discussion 19

2.3.1 SEM of Moth-eye Nanostructures 19
2.3.2 Optical Measurements 20

2.4 Optical Modeling and Optimization 21

2.5 Conclusions 26

2.6 Acknowledgement 26

3. RELIABILITY PERFORMANCE: CORROSION BEHAVIOR OF SILVER AND COPPER UNDER MIXED FLOWING GAS TESTS 27

3.1 Introduction 27

3.1.1 Electronics Reliability in Data Centers 27
3.1.2 Ag and Cu Corrosion under Harsh Environments 28
3.1.3 Relative Humidity Fluctuation Effect on Metal Corrosion 31

3.2 Accelerated corrosion testing 31

3.2.1 Clay Test 32
3.2.2 Flowers of Sulfur (FOS) 32
3.2.3 Mixed Flowing Gas (MFG) 32

3.3 Project Objectives 33

3.4 Experimental Methods 35

3.4.1 MFG System Setup 35
3.4.2 In-situ Cl_2 Monitoring Method 37
3.4.3 Test Conditions for Accelerated Ag and Cu Corrosion in the MFG Chamber 39
3.4.4 RH Cycling Experiments 41
3.4.5 Test Methods for Corrosion Products Quantification 43

3.4.5.1 Weight Gain Measurement 43
3.4.5.2 Cathodic Reduction 43
3.4.5.3 Other Analytical Techniques 44

3.4.6 Chamber Validation 44

3.5 Results and Discussion 45

3.5.1 Effects of Cl_2 Concentration on Accelerated Ag and Cu Corrosion 45
3.5.2 Effects of NO_2 Concentration on Accelerated Ag and Cu Corrosion 50
3.5.3 Effects of High Cl_2 with High NO_2 Concentration on Ag and Cu Corrosion 51
3.5.4 Effects of RH on Accelerated Ag and Cu Corrosion 52
3.5.5 Effects of Temperature on Accelerated Ag and Cu Corrosion........ 53
3.5.6 Effects of RH Cycling on Ag and Cu Corrosion........ 54

3.6 Conclusions 60

3.7 Acknowledgement........ 61

4. ETCHING PERFORMANCE: ATOMIC LAYER ETCHING OF IRON AND COBALT IN MAGNETIC TUNNEL JUNCTION 62

4.1 Introduction 62

4.1.1 Magnetic Random Access Memory (MRAM)........ 62
4.1.2 Magnetic Tunnel Junction (MTJ) Patterning 64
4.1.3 Atomic Layer Etching (ALE)........ 66

4.2 Experimental Methods........ 70

4.2.1 Etching Chamber Setup........ 70
4.2.2 Etching Chamber Validation 72

4.2.2.1 Temperature Calibration........ 72
4.2.2.2 SiO_2 Etching Rate........ 73

4.2.3 Sample and Materials Information 75

4.3 Results and Discussion........ 77

4.3.1 Self-limiting Behavior of ALE Process........ 77
4.3.2 Thermal Etching Rates of Fe and Co 80
4.3.3 AFM of Pristine and Etched Co Samples........ 82

4.4 Conclusions 83

4.5 Acknowledgement........ 84

5. SUMMARY AND FUTURE WORK........ 85

5.1 Optical Performance........ 85

5.2 Reliability Performance 86
5.3 Etching Performance 86
5.4 Final Remarks 88

REFERENCES 89

Appendix

COPYRIGHT PERMISSIONS 99

LIST OF TABLES

Table 2.1 ICP etching parameters for fabrication of Ta_2O_5 moth-eye structures......... 19

Table 3.1 ISA 71.04-2013 Classification of reactive environments 30

Table 3.2 Gas concentrations of Telcordia and Nokia MFG tests 33

Table 3.3 IPC 5 days MFG exposure round robin results 34

Table 3.4 Test conditions for accelerated Ag and Cu corrosion in the MFG chamber 40

Table 3.5 MFG test condition for chamber validation 45

Table 3.6 Mass comparisons for corrosion products of Ag and Cu after 40 hours exposure in MFG 49

Table 3.7 Atomic ratios of O, S and Cl for Ag and Cu coupons after 24 hours exposure in the MFG chamber under condition II (RH = 66%) and III (RH = 82%) . 53

Table 3.8 Comparison of Ag corrosion products weight gain and thickness after 2 days exposure in MFG under 52%-35% RH cycling by different techniques...... 57

Table 3.9 Comparison of Cu corrosion products weight gain and thickness after 2 days exposure in MFG under 52%-35% RH cycling by different techniques...... 57

Table 4.1 Etching conditions for examining self-limiting behavior of Cl_2 and Hfac reactions in Fe and Co ALE. T = 170°C. 77

Table 4.2 Optimized ALE conditions for Fe and Co.. 81

Table 4.3 RMS measured by AFM for selected Co samples 82

LIST OF FIGURES

Figure 1.1 Schematic of an AFM. 3

Figure 1.2 Schematic of sputter deposition chamber. 6

Figure 1.3 Illustration of anisotropic etching (R=0) and isotropic etchin (R=1). 8

Figure 1.4 Process flow of photolithography. 9

Figure 2.1 Normally incident ($\Theta_i \approx 0°$) light in three different media (assume medium 1 and 2 are infinite materials). 14

Figure 2.2 Schematic of GaAsP/SiGe tandem solar cells on Si substrate. 18

Figure 2.3 SEM image of Ta_2O_5 moth-eye structures at 50° relative to normal. Dimensions are corrected for tilt angle. 20

Figure 2.4 Measured total reflection for bare tandem cell (black) and tandem cell with fabricated moth-eye (red). 21

Figure 2.5 Simplified diagram of FDTD model. 22

Figure 2.6 Comparison of simulation and experimental results for moth-eye structures with base diameter of 350 nm and height of 425 nm. 23

Figure 2.7 Contour plot for total weighted absorption as a function of diameter and height of moth-eye structures and DLARCs thickness. Blue arrows denote parameters that produced highest weighted absorption. For moth-eye structures (a), base diameter of 520 nm with cone height of 550 nm gives the best result (absorption of 97.8%). For DLARCs (b), 40 nm SiN_x with 50 nm SiO_2 gives the highest absorption (95.8%). 25

Figure 2.8 Measured total reflection for bare tandem cell (solid black), tandem cell with fabricated moth-eye (dotted red) and simulated total reflection of tandem cell with optimized DLARCs (dotted orange) and optimized moth-eye structures (solid green). 25

Figure 3.1 MFG chamber used in this work 36

Figure 3.2 A gas dry placed between the MFG chamber and the Cl_2 detector to adjust the RH of sample gas. 37

Figure 3.3 Schematic of the Cl_2 detector. (1) Chemcassette® tape (2) LED light which can illuminate sample stain (3) Detector (4) Sample inlet (5) Sample outle 38

Figure 3.4 Detected Cl_2 concentration from the Chemcassette® detector as a function of sample gas RH under two conditions: all gases present in the chamber (orange) and only Cl_2 in the chamber (red). 38

Figure 3.5 Schematic diagram of the MFG system with a 3-way solenoid valve for RH cycling experiments (corrosive gases generation system and antechamber are not shown). 42

Figure 3.6 (a) 52%-35% RH cycles measured by the RH sensor (only two cycles are shown here). Each cycle is 20 mins and data point is recorded every 30 seconds; (b) Corrosive gas concentrations used in the MFG chamber. 43

Figure 3.7 Ag (a) and Cu (b) corrosion rates for chamber validation experiments. Each data point shows result from one run. 45

Figure 3.8 Weight gain per area of Ag (left) and Cu (right) coupons under condition I (black, 20 ppb Cl_2) and II (red, 95 ppb Cl_2). 46

Figure 3.9 Schematic of Cu corrosion mechanism. 47

Figure 3.10 Cathodic reduction plots for Ag (left) and Cu (right) after 40 hours exposure in the MFG chamber under test conditions I (black, 20 ppb Cl_2) and II (red, 95 ppb Cl_2). 48

Figure 3.11 The surface morphology comparisons of Ag coupons during different exposure times in the MFG chamber under test conditions I (a) and II (b). 49

Figure 3.12 Weight gain per area of Ag (left) and Cu (right) coupons under conditions I (black, 200ppb NO_2) and IV (red, 700ppb NO_2). 50

Figure 3.13 Weight gain per area of Ag (left) and Cu (right) coupons under conditions I (black, 20 ppb Cl_2 and 200 ppb NO_2) and V (red, 95 ppb Cl_2 and 850 ppb NO_2). 51

Figure 3.14 Weight gain per area of Ag (left) and Cu (right) coupons under conditions II (black, RH = 66%) and III (red, RH = 82%). 52

Figure 3.15 Weight gain per area of Ag (left) and Cu (right) coupons after 72 hours exposure in the MFG chamber under conditions VI (black, T = 40°C) and VII (red, T = 30°C). 54

Figure 3.16 Comparisons of weight gain per area plots of Ag and Cu coupons after 2 days chamber exposure under RH cycling conditions and constant RH conditions. 56

Figure 3.17 Cathodic reduction plots for corroded Ag (a) and Cu (b) coupons under 52%-35% RH cycling condition and constant 52% and 35% conditions. 58

Figure 3.18 Surface morphology of Ag coupons after 2 days exposure in MFG chamber at (a) 52%-35% RH cycling, (b) constant 35% RH and (c) constant 52% RH. Scale bar is 10 μm. 58

Figure 3.19 EDX spectra for Ag and Cu coupons after 2 days exposure in MFG chamber at (a) 52%-35% RH cycling, (b) constant 52% RH and (c) constant 35% RH. 59

Figure 4.1 Simplified schematic of magnetic tunnel junction element at two distinct resistance states. 64

Figure 4.2 Process flow of one ALE cycle. 68

Figure 4.3 Schematic of the ALE tool setup. 71

Figure 4.4 Five thermocouples placed on Si wafer surface for temperature calibration. 72

Figure 4.5 ALE tool temperature calibration plot. 73

Figure 4.6 (a) SiO_2 coupons map on the sample stage. Gas flow is from right to the left. (b) Etching conditions for SiO_2. 74

Figure 4.7 Etching rates of SiO_2 coupons at different locations on the stage. 75

Figure 4.8 Cross-section of two types of metal samples. 76

Figure 4.9 (a) EDX (10kV) spectrum of a 50nm Co sample. (b) Cross-sectional SEM of a 300nm Co film 76

Figure 4.10 Structure of Hexafluoroacetylacetone. 76

Figure 4.11 Self-limiting plots for Cl_2 reaction in the Fe and Co ALE. (a) M/Ti ratio versus Cl_2 exposure time; (b) M/Ti ratio versus Cl_2 flow rate. Temperature is 170°C. 78

Figure 4.12 Self-limiting plots for Hfac reaction in the Fe and Co ALE. (a) M/Ti ratio versus Hfac exposure time; (b) M/Ti ratio versus Hfac partial pressure. Temperature is 170°C. 79

Figure 4.13 (a) Reduced thickness of Co under different temperatures and ALE cycles. (b) Etching rate of Co as a function of temperature. 81

Figure 4.14 (a) Reduced thickness of Fe under different temperatures and ALE cycles. (b) Etching rate of Fe as a function of temperature. 82

Figure 4.15 AFM image for (a) pristine Co; (b) Etched Co under 140°C after 45 cycles. 83

Figure 5.1 Schematic of in-situ XPS system. 87

ABSTRACT

Surface science and chemistry have been researched in many different disciplines. In this dissertation, the role of surface chemistry in improving performances of electronic devices are discussed. Three different perspectives: optical, reliability, and etching performance in targeted applications are investigated.

In the first topic, Ta_2O_5 moth-eye structures as broadband antireflection coatings (ARCs) in dual junction solar cells on Si substrates are reported. Wafer-scale sub-wavelength structures are directly patterned on the top of tandem cells by using deep UV photolithography and plasma etching. These processes give moth-eye structures with an aspect ratio of 1.2, which results in excellent antireflection properties with an average reflectance of 7% over the entire 400-1100nm range. Further optimizations of moth-eye and traditional double layer antireflection coatings (DLARCs) on the device using the finite-difference time-domain (FDTD) method are performed. Optimized moth-eye structures outperform optimized traditional DLARCs with reflection as low as 2.2% from 400-1100nm.

In the second topic, the mixed flowing gas (MFG) test is used to study accelerated Ag and Cu corrosion behavior in highly corrosive environments. Synergistic effects between Cl_2 and H_2S on Ag corrosion rate in the MFG chamber are presented. Effects of relative humidity (RH), RH cycling, NO_2 concentration and

temperature on Ag corrosion are also investigated using a combination of analytical techniques such as weight gain, cathodic reduction, and SEM/EDX. Cu coupons are used with Ag coupons for direct comparison and reference to chamber corrosivity. The Ag corrosion mechanism is proposed, which enables the establishment of new MFG test conditions to simulate Ag corrosion in more aggressive environments.

In the third topic, thermal atomic layer etching using sequential reactions of Cl_2 and Hexafluoroacetylacetone (Hfac) is proposed to etch Fe and Co. Self-limiting behavior of both Cl_2 and Hfac steps at 170°C is first found and a range of etching temperatures from 140°C to 185°C is investigated. The etching rates of Fe and Co can be achieved as low as 0.3nm/cycle and 0.2nm/cycle respectively at 140°C. Atomic force microscopy (AFM) is also used to compare surface morphology of the pristine and etched Co samples. This work provides the patterning solution for achieving high-density magnetic random access memory (MRAM) devices.

Chapter 1

INTRODUCTION

Surface chemistry can be defined as understanding of reactions which occur between adjacent phases, such as solid-gas or solid-liquid etc. [1]. Extensive research on surface chemistry has been focused on a variety of applications [1][2] and the scale ranges from micrometers to nanometers. In this dissertation, the role of surface chemistry in the electronic industry is discussed. Specifically, we want to use understanding of surface chemistry to improve the performances of electronic devices. Three different projects described in the dissertation, including applications in photovoltaic (PV), electronics reliability, and memory device fabrication, are all connected through surface science.

In this chapter, instrumentations used for surface analysis are first introduced. Comprehensive analytical techniques are important tools for understanding surface phenomena. The fabrication processes utilized in the chapter 2 and 4 are discussed. Surface chemistry plays a key role in achieving the desired output from these processes. Lastly, the objective and outline of this dissertation are briefly summarized.

1.1 Surface Chemistry Analytical Techniques

1.1.1 X-ray Photoelectron Spectroscopy

X−ray photoelectron spectroscopy (XPS), also known as electron spectroscopy for chemical analysis (ESCA), is one of the most powerful and commonly used analytical techniques in the field of surface science [3]. In XPS, the X-ray is generated when high-

energy electrons emitted from a heated filament (cathode) strike an anode target. Magnesium and aluminum are the two most common materials as X-ray sources. Due to the photoelectric effect, an electron can be ejected from the sample when the X-ray energy is sufficient to overcome the energy barrier for emission. The ejected electron has kinetic energy, which is dependent on the X-ray energy and the binding energy of its original atomic orbitals. Since only electrons within the top few layers are able to escape from the material without energy loss, XPS is a very surface-sensitive (0-10nm) technique. XPS is usually operated under ultra-high vacuum (~10^{-9} torr) to keep substrates clean.

The binding energy of the electron can be calculated as below [4]:

$$E_{BE} = E_{h\nu} - E_{KE} - \phi \tag{1.1}$$

where E_{BE} is the binding energy of the core electron, $E_{h\nu}$ is the X-ray energy, E_{KE} is the kinetic energy of excited photoelectron recorded by the detector, ϕ is the work function of the spectrometer and the value is either known or a constant in a given system.

In a typical XPS spectrum, each characteristic peak indicates the binding energy of a specific element in its atomic state. The binding energy is also affected by the chemical state of the atom. Electrons ejected from oxidized atoms tend to have higher binding energy than electrons from atoms with reduced chemical states. Besides the elemental information, the atomic ratio of each element can be calculated by integrating the peak area and applying the sensitivity factor, which is determined by the system.

In this work, a PHI 5600 system with an Al Kα monochromatic X-ray source ($E_{h\nu}$ = 1486.6 eV) or Mg Kα anode ($E_{h\nu}$ = 1253.6 eV) is used. The detector is placed at 45° offset from the sample.

1.1.2 Atomic Force Microscopy

Atomic force microscopy (AFM) provides surface topographical information with excellent high resolution (sub-nm) [5]. The AFM probe consists of a cantilever with a tip at its end. A laser beam is used to hit the flat top of the cantilever and the position of the reflected beam is tracked by a position-sensitive photodiode. When the tip scans the sample surface, the deflection of cantilever is recorded through the signal changes of this laser beam. Figure 1.1 shows the schematic of an AFM.

There are three different scanning modes in AFM: contact mode, tapping mode and non-contact mode. Definitions and theories of these modes are based on inter-atomic force between the tip and the sample surface.

In the contact mode, the tip is usually in close contact with the sample surface where the force between them is repulsive. In this mode, the tip-surface force or height is constant so that the deflection of cantilever can be used as input to move the scanner in the z direction and then generate an image. This mode is the most straightforward mode in AFM, however, it is aggressive which can lead to surface damage of the sample or tip.

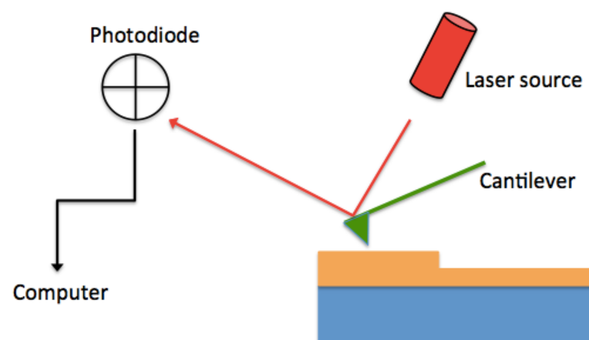

Figure 1.1 Schematic of an AFM.

In the non-contact mode, the tip-surface force is attractive indicating the tip is close to the sample surface but not touching it. The tip in this mode oscillates in a resonance frequency and detection of such frequency is an indirect measurement of surface topography. The non-contact mode provides relatively low resolution compared with the contact mode.

Tapping mode takes the advantages of both the contact mode and the non-contact mode. In the tapping mode, the tip oscillates at a closer distance than in the non-contact mode. Therefore, it has enhanced resolution by intermittently contacting the sample surface. It also has sufficient amplitude to limit possible damage of the samples. Tapping mode is usually used to analyze soft or fragile samples.

The AFM used in chapter 4 is a NX20 model from Park Systems. Non-contact tips (OMCL-AC160TS, Park Systems) are used to analyze metallic samples and a scan size of $10\mu m \times 10\mu m$ is chosen for each experiment.

1.1.3 Scanning Electron Microscopy and Energy Dispersive X-ray Microscopy

Scanning electron microscopy (SEM) uses a focused beam of electrons to generate images with topographical information of the sample. From the electron-sample interaction, a variety of signals are created including secondary electrons, X-rays, and backscattered electrons etc. There are various detectors in the SEM system for different applications. Detection with the secondary electron is the most common way to study surface morphology of the material. Energy dispersive X-ray microscopy (EDX) is often used in conjunction with SEM. In EDX, characteristic X-rays are generated by incident electrons and collected by the detector to determine elemental information about the sample. The counts and energy of X-rays are plotted in the EDX spectrum. Although

EDX and XPS can both be used to perform elemental analysis of a sample, XPS is a surface-sensitive technique whereas, EDX is usually used for bulk sample measurement since generated X-rays can penetrate deeper compared with photoelectrons.

1.2 Fabrication Processes

Advanced semiconductor manufacturing requires sequential, sophisticated process steps to fabricate integrated circuits (ICs). In this dissertation, various fabrication methods such as deposition, etching (removal) and photolithography are utilized in the targeted applications. There are tremendous efforts in each of these disciplines to push the physical limits of semiconductor fabrication. Many reviews have focused on the development and future scope of each fabrication method [6][7][8][9][10].

1.2.1 Deposition Methods

Layers of different materials have to be deposited during the IC fabrication process. Semiconductor deposition can be generally divided into two groups. One is called chemical vapor deposition (CVD) and the other one is physical vapor deposition (PVD). The principle of the CVD process involves the use of a precursor gas to react with the substrate material and deposit a thin film on its surface. Such reaction can be facilitated by either heating the substrate to a high temperature or applying radio frequency (RF) power on the electrodes to ionize gaseous species and form more reactive ions to react on the surface. The CVD process is strongly dependent on the surface chemistry and provides the growth mechanism for a variety of materials using different deposition precursors.

In the PVD process, there is no chemical reaction involved and a target is put into the system to serve as the deposition source material. Sputter deposition is the most

common PVD process. Figure 1.2 shows the schematic of a sputter deposition chamber. The sputtering target (cathode) and the substrate (anode) are put on two electrodes. RF power is usually applied to both electrodes to generate gaseous plasma. When sputtering gas is introduced into the chamber, it can be ionized to form ions and electrons. These ions are accelerated onto the target due to the electric field and can strike out the atoms or molecules of the target. These particles can then reach out to the surface of the substrate and form thin films on it. Argon has been widely used as the sputter gas since it is chemically inert and requires relatively low ionization energy. Sputter deposition is widely used as a deposition method to grow metallic and metal oxides films.

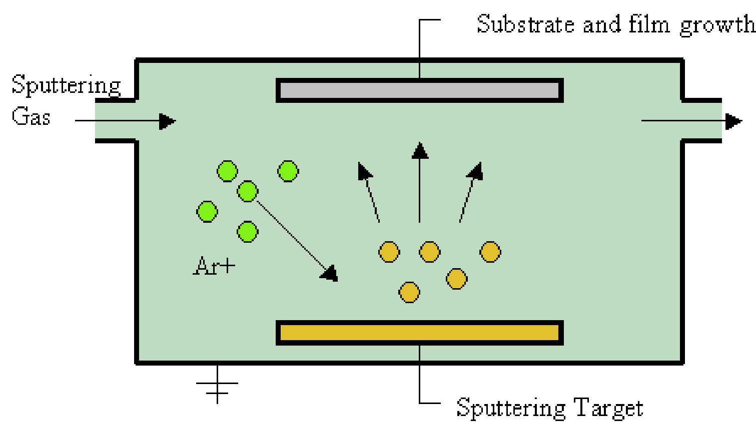

Figure 1.2 Schematic of a sputter deposition chamber.

1.2.2 Etching Methods

In contrast to deposition, etching is the process step to remove materials to create desired features in electronic devices. It can be categorized as wet etching or dry etching. The process flow for both types includes transport of etchants to the sample surface,

surface reaction to produce soluble or volatile species, and transport of products away from the sample.

The principle of wet etching is to use chemical solutions to react with the substrate and form soluble compounds in the solution. This technique is widely used in the Si wafer cleaning process, and hydrofluoric acid is the most common etchant to remove away native oxide on the Si surface. Wet etching requires a simple setup and is highly sensitive to the etchant and the substrate.

Dry etching, as opposed to wet etching, is a vapor phase process. Dry etching often refers to plasma etching and operates under vacuum conditions. Similar to vapor-phase deposition, there are generally two types of dry etching: physical sputtering and reactive ion etching (RIE). In physical sputtering, an inert gas (e.g. argon) ions are used to bombard the to-be-etched substrate. This process is driven by momentum transfer of Ar^+ and atoms in the substrate during the collision. Since there is no chemistry involved, physical sputtering usually yields very low selectivity. In RIE, chemically reactive species are ionized under RF power for reaction with the substrate to form volatile species, which can be pumped out of the chamber. Since reactive ions are involved, this process is highly selective depending on the etching chemistry.

The advantage of dry etching compared with wet etching is its anisotropy. The etching isotropy, R, can be defined using the equation below:

$$R = \frac{Horizontal\ etching\ rate\ (r_h)}{Vertical\ etching\ rate\ (r_v)} \tag{1.2}$$

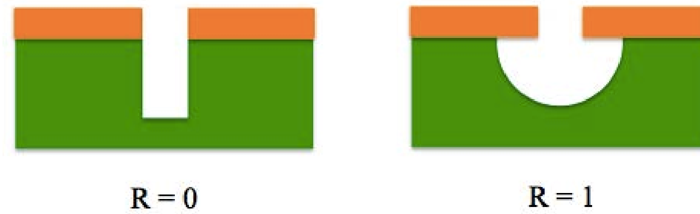

Figure 1.3 Illustration of anisotropic etching (R=0) and isotropic etching (R=1).

Figure 1.3 shows the comparison of anisotropic etching and isotropic etching. In anisotropic etching, materials are removed in a specific direction. The horizontal etching rate tends to be zero or much smaller than the vertical etching rate. As for isotropic etching, the horizontal etching rate is the same as the vertical etching rate. Wet etching is highly isotropic and therefore is not desired in complicated IC fabrication processes.

1.2.3 Photolithography

Photolithography, also known as UV lithography, is a critical process in patterning semiconductor devices. Planar films are usually not desired in high-density semiconductor chips. Devices with patterned features need excellent accuracy in photolithography. Unlike deposition and etching, photolithography usually involves a sequence of steps. Figure 1.4 demonstrates the process flow of photolithography. The process starts with the substrate having deposited material on it. The first step is to coat photoresist (PR) on the substrate by using spin coating. A soft bake is used to remove the solvent from the PR. The second step is mask alignment, during which the mask has to be perfectly aligned with the substrate to transfer the exact pattern onto the surface. After this step, the PR is exposed to high density ultraviolet (UV) light through the pattern on the mask. This exposure step is the most important part in the process since it controls the resolution of the technique, which depends on several parameters such as UV light source, optics apertures etc.

If the PR is a positive resist, the areas exposed to the UV light can be removed during the development step (see Figure 1.4). Exposure of the resist under UV light changes the chemical structure of the PR so that it becomes soluble in the developer. However, if the PR is a negative resist, the areas not exposed to the UV light are to be removed. The exposed areas become polymerized under UV and are more difficult to be dissolved in the developer solution. Post-bake is used to harden the PR and make it more adhesive to the sample surface. After this step, the PR is patterned on the surface. Dry etching is usually used to etch the exposed material while the PR is considered to be a hard mask to protect the underneath layer. Once the etching is finished, a stripping step is used to remove the PR material. Oxygen plasma (ashing) is one of the common methods to etch away the PR. Simple solvents can also be utilized to remove PR residuals.

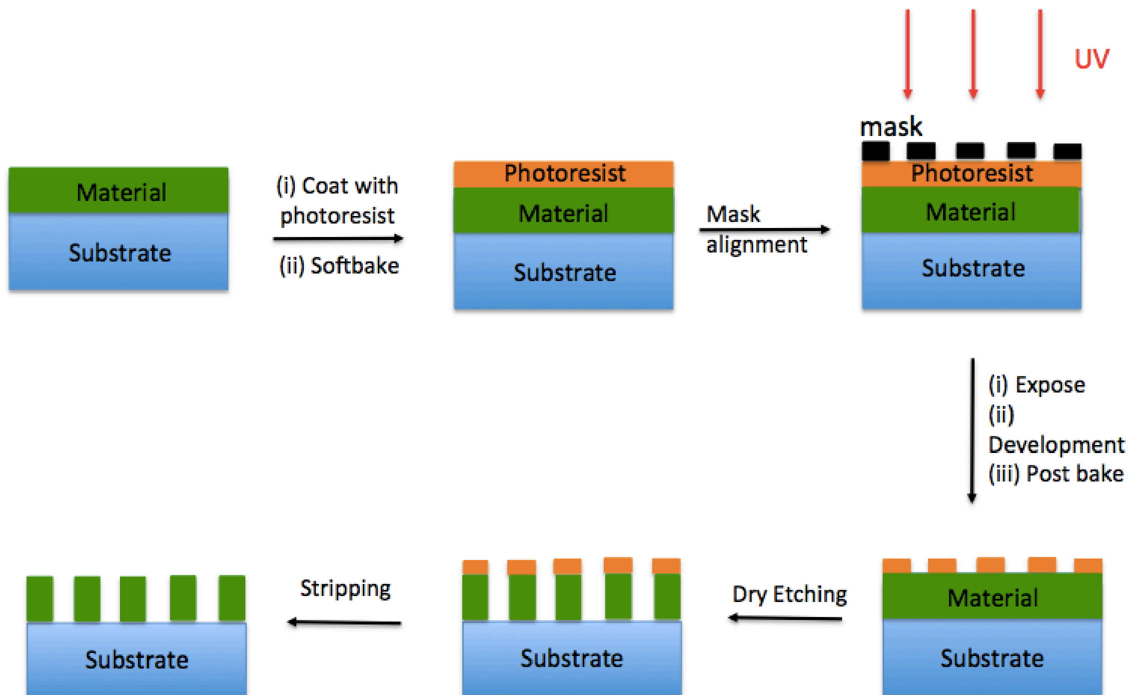

Figure 1.4 Process flow of photolithography.

1.3 Dissertation Objective and Outline

The main objective of this dissertation is to utilize knowledge of surface chemistry to propose new approaches to enhance performances of electronic devices. Three different aspects: optical, reliability, and etching performance in targeted applications will be discussed in the following chapters.

Chapter 2 covers a novel fabrication method to pattern Ta_2O_5 moth-eye antireflection coatings to improve optical performance of III-V tandem solar cells on Si substrate. Optical simulations to optimize these moth-eye nanostructures is described as well. Chapter 3 investigates effects of different parameters (Cl_2, temperature etc.) on accelerated Ag and Cu corrosion in a mixed flowing gas chamber. A proposed Ag corrosion mechanism enables establishment of new accelerated testing conditions to evaluate reliability of immersion Ag surface finishes on printed circuit boards. Chapter 4 discusses deployment of an atomic layer etching technique to improve etching performance of magnetic tunnel junctions. This highly controlled etching method is a key factor to achieve high-density magnetic random access memory devices. Chapter 5 summarizes the major contributions of this dissertation and provides some perspectives of the future work.

Chapter 2

OPTICAL PERFORMANCE: TANTALUM PENTOXIDE MOTH-EYE ANTIREFLECTION COATINGS IN TANDEM SOLAR CELLS ON SILICON

2.1 Introduction

2.1.1 III-V Tandem Solar Cells on Si Substrate

Silicon solar cells have the longest production history in the photovoltaic (PV) industry and accounted for about 94% of the total production in 2016 [11]. This dominant position in PV technology is largely due to silicon's natural abundance and the cost-effective growth and fabrication processes in comparison to other solar cell materials. The theoretical maximum efficiency for a single junction Si solar cell is around 33% [12] and it can be further limited to 29.1% due to the factors such as Auger recombination and free carrier absorption [13][14]. The current world record efficiency of a lab mono-crystalline Si solar cell is reported as 26.6% in 2017 [15], which is only increased by absolute 1% compared with the previous record efficiency of 25.6% in 2014 [16]. These results suggest that there is only a little room for improvement of single-junction Si solar cells efficiency.

Due to the ability to exploit multiple absorption bands, multijunction solar cells (MJSCs) are the most efficient solar cells ever developed [17]. MJSCs (also referred to tandem cells) typically have two or more active subcells in which the high-bandgap top cell can absorb high energy photons while low-bandgap bottom cell absorbs photons with relatively lower energy. The more junctions the solar cell has, the higher theoretical efficiency it can achieve [18]. Thermalization losses can be reduced in this multijunction system [19]. III-V compounds are usually the choice of materials used in MJSCs because

of their suitable optical and material properties to absorb light in the solar spectrum. The record efficiency for III-V MJSCs was reported as 46.5% at 324x suns [20] with a four-junction cell structure of GaInP/GaAs//GaInPAs/GaInAs.

Nevertheless, III-V tandem solar cells turn out to be extremely expensive and are mainly used for space and highly concentrated terrestrial solar power plants [21]. One of the main sources of the solar cell cost is from the starting substrate. GaAs and Ge substrates are often used in III-V tandem cells because they are lattice-matched with the active device layers to enable direct epitaxy growth of III-V. However, GaAs and Ge are significantly more expensive than Si, which makes the III-V tandem cells less competitive for large-scale deployments.

It is in this context that research on fabricating multijunction devices directly on Si platforms has gained increasing interest [22][23]. Since the Si substrate is lattice mismatched with most III-V materials, direct growth of III-V on Si is extremely challenging [22]. The lattice mismatch can very likely cause formation of defects and dislocations, which is unfavourable to achieve high efficiency solar cells.

The metamorphic Si_xGe_{1-x} buffer layer developed by AmberWave [24] has been used between Si substrate and the bottom SiGe cell to bridge the lattice constant of the two layers and provide a low-dislocation interface [25]. In our previous work, the theoretical limit of GaAsP/ SiGe tandem cells on Si was reported and a potential efficiency of 40% was expected to be achieved [26]. Much of the focus has been placed on fabrication and characterization of III-V structures [27] following this simulation. However, antireflection coatings have not been applied in the previous cell structures.

2.1.2 Objectives of Antireflection Coatings (ARCs)

2.1.2.1 Introduction

The short circuit current density of the solar cells can be calculated as follow:

$$J_{sc} = \frac{q}{hc}\int_{\lambda} \lambda' A(\lambda') Irrd(\lambda') d\lambda' \quad (2.1)$$

In equation (2.1), J_{sc} is the short circuit current density, q is the charge of an electron, h is Planck's constant, c is the speed of light, λ is the wavelength, A represents the absorption of the solar cell and *Irrd* is the solar irradiance spectrum [28][29].

The efficiency of the solar cell can be expressed as:

$$Efficiency = \frac{J_{sc} \times V_{oc} \times FF}{P_{in}} \quad (2.2)$$

where V_{oc} is the open circuit voltage, FF is the fill factor, and P_{in} is the power incident on the solar cell. We see that the solar cell efficiency is directly related to the short circuit current (J_{sc}).

Antireflection coatings (ARCs) are indispensable to achieve high efficiency solar cells since it can be used to reduce the light reflection on the front surface of the solar cells and therefore couple the maximum amount of light into the device. Increase of light absorption leads to increase of J_{sc}.

Light reflection happens when the light hits the interface between two media with a refractive index difference. To simplify the case, imagine we only have normally incident light on the interface of two media; according to Fresnel's equation, the reflection coefficient can be calculated as

$$r_{12} = \frac{n_1 - n_2}{n_1 + n_2} \quad (2.3)$$

where n_1 is the refractive index of the first medium and n_2 is the refractive index of the second medium. The reflectance, which is the ratio of the reflected power and incident power, can be described as the square of the magnitude of the reflection coefficient [30]:

$$R = \left| r_{12} \right|^2 \times 100 \tag{2.4}$$

If a single layer of ARC is added between the two layers, namely there are three different media, light reflections happen twice (see Figure 2.1, assume $\Theta_i \approx 0°$). One reflection is at the interface of medium 1 and the AR coating, and the other is at the interface of the AR coating and medium 2.

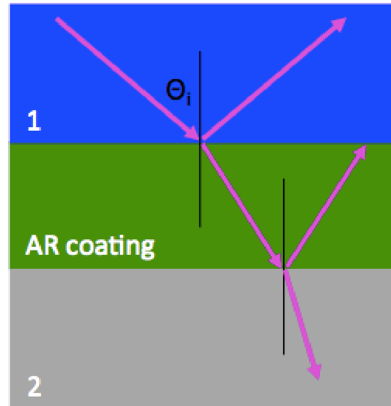

Figure 2.1 Normally incident ($\Theta_i \approx 0°$) light in three different media (assume medium 1 and 2 are infinite materials).

If we want to have the total reflectance close to zero, based on the principle of interference effect of light, destructive interference of these two reflected light waves needs to be achieved. In this case, the thickness of the AR coating is set to be λ/4 and the magnitudes of the reflectance of the two reflected lights are the same, which can be demonstrated as:

$$\left|\frac{n_1 - n_0}{n_1 + n_0}\right|^2 = \left|\frac{n_0 - n_2}{n_0 + n_2}\right|^2 \tag{2.5}$$

where n_1 is the refractive index of medium 1, n_0 is the refractive index of AR coating and n_2 is the refractive index of medium 2. After solving equation (2.5), it shows that:

$$n_0 = \sqrt{n_1 n_2} \tag{2.6}$$

This equation suggests the ideal refractive index of the AR coating should be determined by the product of the refractive indices of the top and bottom materials. Another key element for choosing an AR coating is that the material should have a relatively large bandgap so that it is "transparent" to the solar device and the light can pass through the coating without being absorbed. Typical AR coating materials include MgF_2, ZnO, and TiO_2.

The drawback for such a single AR coating is that it can only eliminate the reflection at a single wavelength, which is not sufficient for achieving low reflection across a broad range of wavelengths. By adding multiple AR coatings, antireflection performance can be enhanced at different wavelengths [31], but it also increases the manufacturing cost.

2.1.2.2 ARCs on III-V Tandem Cells

AR coating design is especially important and challenging in tandem solar cells [32]. Since tandem solar cells can absorb light over a wider range of wavelength compared with the single junction solar cells, a broadband AR coating is needed to couple more light into the device. Also, due to the fact that tandem cells are usually connected in series, the short circuit current (J_{sc}) is limited by the subcell that provides the lowest current. Therefore, the overall performance of the AR coating is evaluated by

the current-limiting subcell. Interference-based AR coatings are usually used in tandem solar cells [33]. As mentioned, however, they are limited to low reflection at a single or few wavelengths. More importantly, the material with an ideal refractive index might not be available in nature. Any deviation of the coatings from optimum might increase current mismatch of the tandem cell device [32].

Recently, antireflective nanostructures have been proposed as a solution to achieve low reflection across a broad spectral band, which is more forgiving of current mismatched subcells [34][35]. Such sub-wavelength nanostructures usually have a tapered geometry, which provides a gradient change rather than abrupt steps in the refractive index from air to the top semiconductor layer. Reflection thus can be efficiently decreased over a broad wavelength range and at all angles of incidence [36]. The specific type of nanostructures we used in this work is called the "moth-eye" structure, which was first reported in 1973 [37]. We present a description of the fabrication of broadband Ta_2O_5 moth-eye ARCs for tandem solar cells on Si. Ta_2O_5 has been chosen as the material of interest because of its matched refractive index with the tandem cell top layer in addition to its low extinction coefficient across the spectrum.

2.1.3 Optical Modeling: Finite Difference Time Domain (FDTD)

The finite difference time domain (FDTD) method is used to simulate the performance of moth-eye AR coatings optically. It was first proposed by Yee [38] to analyze the scattering of an electromagnetic pulse from a perfectly conducting cylinder. This method has been extended to study the reflection, transmission and propagation of light within complex geometries based on the differential formulations of the Maxwell's equation [39]. The FDTD method can not only be used to solve electromagnetic

equations for a planar structure but also for two-dimension and three-dimensional structures. It is capable of solving Maxwell's equation in the time domain rather than in the frequency domain, which makes the frequency band spectrum realized in a single simulation. However, the FDTD method can sometimes be time-consuming.

In this work, the commercial software package, 'FDTD Solutions' by Lumerical (Lumerical Solutions, Inc. Canada) is used. When modeling a 3D structure using FDTD, the geometry and optical properties (n & k) of each different material involved, along with any optical input sources and monitors, must be clearly specified and the simulation region and boundary types must also be defined. The perfectly matched layer (PML) is the most commonly used edge condition, in which incident light is strongly absorbed. The geometry is discretized into a mesh of cuboids known as Yee cells [38] and Maxwell's time-dependent curl equations are solved at nodes across these cells.

2.2 Experimental Methods: Fabrication of Moth-eye Nanostructures

The schematic of the tandem cells can be seen in Figure 2.2. The SiGe layer is grown by using reduced pressure chemical vapor deposition (RPCVD) on a (100) CZ Si substrate. The III-V layers growth are completed by using a metal organic chemical vapor deposition (MOCVD) tool from Veeco. The details of fabrication procedure of this dual junction solar cells have been described elsewhere [27]. The SiGe bottom cell is considered to be the current-limiting subcell of the full device.

The cell is first treated with NH_4OH: H_2O_2: H_2O (7:35:160) to remove the uppermost GaAsP contact layer. 25 nm GaInP is deposited on the GaAsP top cell as a window layer. Directly patterning the moth-eye structures by using this window layer on our device is not feasible. Cone-shaped moth-eye structures are fabricated in the

following fashion. First, Ta_2O_5 is deposited onto the window layer of the solar cell structure using a Veeco Nexus Dual-Beam ion beam deposition system. The deposition beam (aimed at the Ta target) parameters are 1200 V, 420 mA, with Xe at 5.2 sccm. The assist beam (aimed at the substrate) parameters are 50 V, 310 mA, with O_2 at 20 sccm. Deposition is carried out for 85 minutes on the sample at 40 degrees relative to normal. The resulting films are approximately 580 nm in thickness, as measured by a Woollam M2000DI variable angle spectroscopic ellipsometer system over the wavelength range of 400-1100 nm.

GaAsP	Contact Layer
GaInP	Window Layer
GaAsP	III-V Top Cell
GaInP	BSF
GaAsP	Tunnel Junctions
GaInP	III-V Nucleation
SiGe	Bottom Cell
SiGe	Graded Buffer
Si	Substrate

Figure 2.2 Schematic of GaAsP/SiGe tandem solar cells on Si substrate.

After deposition, the samples are patterned using 248 nm deep UV (DUV) lithography on an ASML 5500/300 system. The full wafer pattern is made by stitching together 4mm × 4mm areas of dense hexagonal close packed arrays consisting of 150 nm dots spaced with a 350 nm pitch. The lithography process proceeds as follows. A DUV antireflective coating, AR2-600, is first spun at 3.5 krpm for 30s and baked for 60s at 210°C on a hot plate. Shipley UVN 2300-0.5 is then coated at 2.5krpm for 30s and baked

for 60s at 110°C on a hot plate. The pattern is exposed with a dose of 109mJ using a system numerical aperture of 0.63 with annular illumination conditions (S_o=0.8, S_i=0.5). The sample is developed for 20s using AZ300MIF developer. Following lithography, the sample is etched in a Panasonic E640 inductively coupled plasma etching system at 15°C substrate temperature. The sample is mounted to a 6" silicon wafer carrier using Santovac 5 oil to provide thermal contact between the sample and wafer carrier. Etching is executed in 3 steps. Gases, powers, and etched materials are indicated in Table 2.1. During the etching of the Ta_2O_5 in step 2, the photoresist (PR) mask is also etched into a cone shape due to physical sputtering. CHF_3 polymer sidewall passivation and the PR ablation together lead to the final moth-eye structures.

Table 2.1 ICP etching parameters for fabrication of Ta_2O_5 moth-eye structures

Etch Step	1	2	3
Material	AR2 between dots	Ta_2O_5	Residual PR Mask
Gas	O_2	CHF_3	O_2
Flow (sccm)	40	40	40
ICP Power (W)	75	500	200
Sample Power (W)	75	200	100
Time (m:s)	0:40	4:40	3:20

2.3 Experimental Results and Discussion

2.3.1 SEM of Moth-eye Nanostructures

Moth-eye Ta_2O_5 nanostructures are shown in Figure 2.3. The cone height of these nanostructures is 425 nm and their base diameter is 350 nm, which gives an aspect ratio (cone height/base diameter) of 425/350≈1.2. Closely packed nanocones indicate there is no obvious discontinuity of refractive index between air and the top semiconductor layer.

A proof of concept Ta_2O_5 moth-eye structures fabricated directly on III-V/SiGe solar cell on Si for ARCs has thus been shown here.

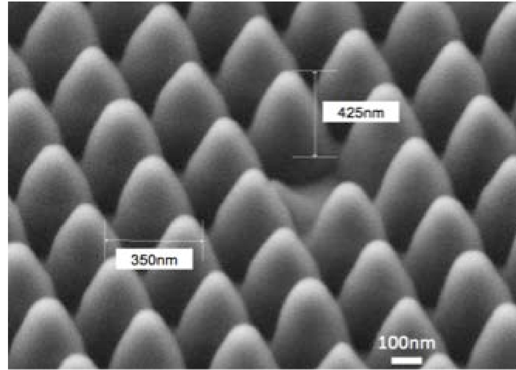

Figure 2.3 SEM image of Ta_2O_5 moth-eye structures at 50° relative to normal. Dimensions are corrected for tilt angle. © 2017 IEEE.

2.3.2 Optical Measurements

The total optical reflectivity of the solar cell with the patterned moth-eye structures is measured from 400-1100 nm by using a UV-visible-IR spectrometer fitted with an integrating sphere (Perkin-Elmer Lambda 750) at an angle of incidence of 8 degrees from normal. Figure 2.4 compares the reflectance from a bare dual junction cell without ARCs and the same cell with patterned Ta_2O_5 moth-eye structures. The bare solar cell shows an average reflectance of 35% over the measured spectral range. However, the cell with Ta_2O_5 moth-eye structures shows an average absolute reflectance decrease of 28% over 400-1100 nm. For wavelengths above 700 nm, since the absorption coefficient of the GaAsP layer drops off rapidly [40], interference patterns occur because the light reaches various interfaces throughout the III-V stack and most prominently between the III-V and SiGe.

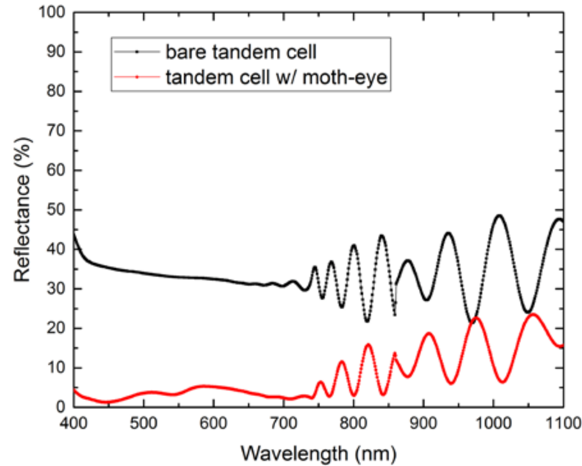

Figure 2.4 Measured total reflection for bare tandem cell (black) and tandem cell with fabricated moth-eye ARCs (red).

2.4 Optical Modeling and Optimization

FDTD simulations are first validated by comparing with experimental results. Parameter sweeps are then used to further optimize the device geometries and explore the limits of the antireflection approaches. Two antireflection schemes are simulated, one of the device structure with conventional double layer antireflection coatings (DLARCs) and one of device structure with Ta_2O_5 moth-eye antireflection hemispheres on top.

The initial material geometries are chosen to match those of the physical device and the optical properties of each material are determined either using Lumerical's present material database or from ellipsometry measurements and model fitting [40]. A plane wave source is placed at normal incidence to the front surface of the modeled structure and a 2D frequency-domain field and power (FDFP) monitor is placed behind the source in order to calculate reflectance. The simulation boundaries are specified as PML in the +/- z direction, resulting in a semi-infinite SiGe substrate. In the +/- x and y directions the simulation boundaries are specified as periodic, creating an effectively

infinitely wide periodic device. Figure 2.5 shows the simplified schematic of the FDTD model. The wavelength range of the results is set from 400nm to 1100nm with 300 frequency points recorded by the monitor.

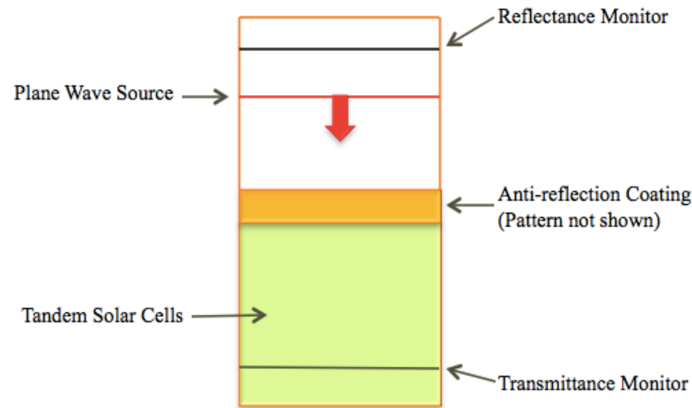

Figure 2.5 Simplified diagram of FDTD model.

The FDTD model and simulation technique are first validated by comparison of Ta_2O_5 moth-eye ARCs simulation results with experimental results at fabricated dimensions: base diameter of 350 nm and height of 425 nm (see Figure 2.6). Observed variations between simulation and experimental results may be due to several reasons. Firstly, in FDTD the optical data for a material must be fitted to a continuous equation, thus introducing some error to the data in cases where the model fit is not ideal. Additionally, curved surfaces such as those of the Ta_2O_5 layer are discretised into Yee cells using a staircase like approximation, which can lead to some error. Accuracy can be improved by defining smaller mesh cells at the expense of increased simulation time and memory usage (in this case a mesh size of 15 nm in the Ta_2O_5 layer is used). Finally, for speed and efficiency purposes the simulation has been carried out at normal incidence whereas the measurements are determined at an angle of 8 degrees. It is also important to note that the optically modelled geometry is specified as being perfectly periodic with

each moth eye having the exact same dimensions and no variation in layer thickness. In reality, this will not be the case for any physical device and therefore disagreement between measurements and simulation may arise. Despite these discrepancies, the agreement between simulation and measurement has shown to be good, indicating that the FDTD technique can provide an efficient method for further optimization of the ARC coating.

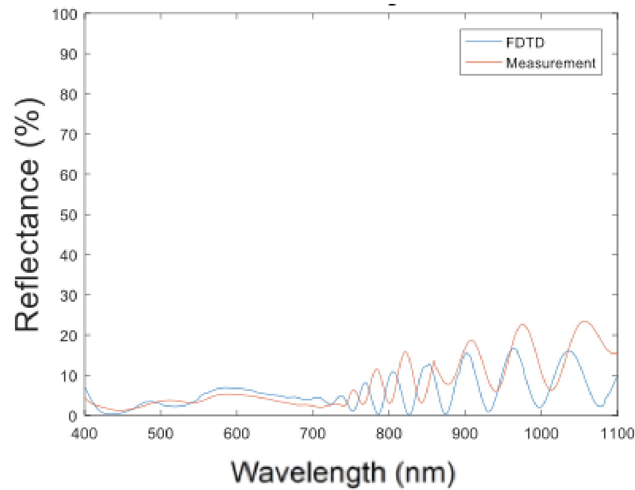

Figure 2.6 Comparison of simulation (blue) and experimental (red) results for moth-eye structures with base diameter of 350 nm and height of 425 nm.

The traditional double layer antireflection coatings (DLARCs) used in this work consist of SiO_2 and SiN_x layers. DLARCs are optimized using a dual parameter sweep of the SiO_2 and SiN_x layer thicknesses. For each layer, the thickness is varied between 0 and 160 nm, in intervals of 10 nm, resulting in 289 full simulations in total. Broadband reflectance result is acquired for each case and the total weighted absorption is then calculated by using equation (2.7). The Ta_2O_5 moth-eye antireflection hemispheres are optimized by sweeping the height and diameter of the hemispheres. Hemisphere height

varies from 100 to 600 nm in interval steps of 25 nm while hemisphere diameter changes from 120 to 620 nm in interval steps of 100 nm. The modeled hemispheres are arranged in a hexagonal pattern, matching that of the experimental device. Throughout optimization, the spacing of the x and y boundaries is adjusted such that the pitch of the simulated hemisphere pattern is equal to the hemisphere diameter, creating a close packed array. For each parameter tested, broadband reflectance result is acquired and total weighted absorption is then calculated. Contour plots showing the resulting weighted absorption for both moth-eye and DLARCs parameter sweeps are presented in Figure 2.7 (a) and (b) respectively.

$$A = 1 - R = 1 - \frac{\sum_{400}^{1100} (R(\lambda) * AM1.5(\lambda))}{\sum_{400}^{1100} AM1.5(\lambda)} \tag{2.7}$$

where A is weighted absorption; R is weighted reflectance; $R(\lambda)$ is reflectance at wavelength λ; AM1.5 spectrum is taken from tabulated values of the ASTM G173-03 [29].

The optimized DLARCs design of 50 nm SiO_2 with 40 nm SiN_x gives the best weighted absorption result of 95.8% and base diameter of 520 nm with height of 550 nm gives the best moth-eye structures with weighted absorption of 97.8% from 400-1100 nm. Figure 2.8 also shows broadband reflectance results for the optimized DLARCs and moth-eye structures. An absolute reflectance decreases of 9.7% for the optimized moth-eye structure is shown compared with optimized DLARCs from 770-1100 nm, which is within the absorption range of the current-limiting SiGe bottom cell. More light will then be absorbed in the SiGe subcell, which will lead to an increase of cell current.

Fabrication of this optimized moth-eye geometry can be achieved by tuning parameters of the template used for plasma etching.

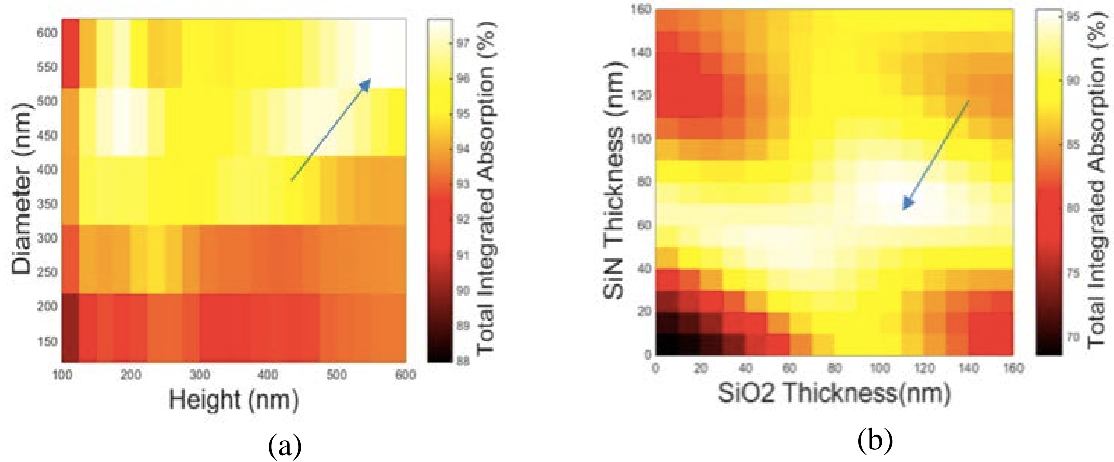

Figure 2.7 Contour plot for total weighted absorption as a function of diameter and height of moth-eye structures and DLARCs thickness. Blue arrows denote parameters that produced highest weighted absorption. For moth-eye structures (a), base diameter of 520 nm with cone height of 550 nm gives the best result (absorption of 97.8%). For DLARCs (b), 40 nm SiN_x with 50 nm SiO_2 gives the highest absorption (95.8%). © 2017 IEEE.

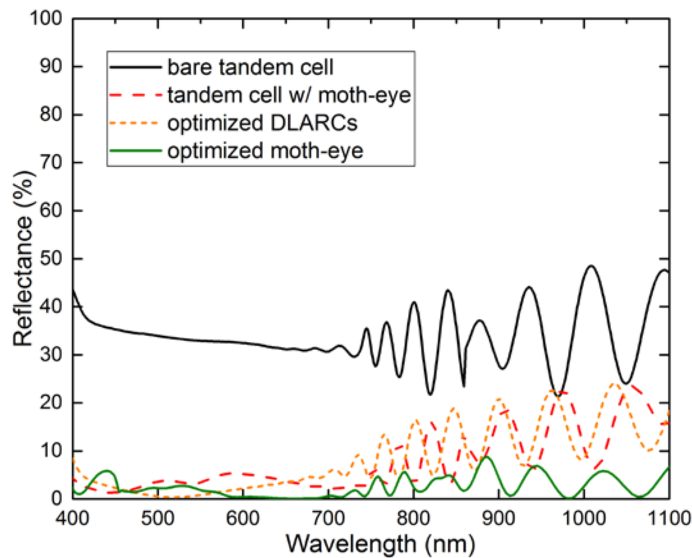

Figure 2.8 Measured total reflection for bare tandem cell (solid black), tandem cell with fabricated moth-eye (dotted red) and simulated total reflection of tandem cell with optimized DLARCs (dotted orange) and optimized moth-eye structures (solid green).

2.5 Conclusions

In summary, a simple, cost-effective approach to fabricate sub-wavelength structured Ta_2O_5 moth-eye ARCs on dual junction GaAsP/SiGe solar cells on Si is developed. This type of ARCs shows excellent broadband antireflective performance: an average reflectance of 7% is achieved from 400-1100 nm. FDTD simulations are used to optically optimize moth-eye structures and traditional DLARCs. With simulated parameters sweeps, further optimization of the moth-eye pattern geometry can achieve reflection as low as 2.2% from 400-1100 nm. It shows that optimized moth-eye structures outperform traditional DLARCs in longer wavelength from 550-1100 nm. Future work will focus on testing antireflective performances of moth-eye structures at different incident angles and improving tandem cells performances by patterning Ta_2O_5 ARCs.

2.6 Acknowledgement

This work is supported by Australian Renewable Energy Agency (ARENA). Part of this work is carried out at University of California, Santa Barbara Nanofabrication Facility, supported by the National Science Foundation and the National Nanofabrication Infrastructure Network (NNIN).

Chapter 3

RELIABILITY PERFORMANCE: CORROSION BEHAVIOR OF SILVER AND COPPER UNDER MIXED FLOWING GAS TESTS

3.1 Introduction

3.1.1 Electronics Reliability in Data Centers

Data center operation usually requires reliable power supplies, data communication connections and an environmental control system to maintain the appropriate temperature and relative humidity (RH) for the information technology (IT) equipment [41]. The energy consumption in the data centers can be significant. Electricity usage in US data centers is increased by 4% from 2010-2014, which is significantly lower than the 24% increase from 2005-2010 and nearly 90% increase from 2000-2005 [42]. This efficiency improvement is largely due to the adoption of airside economizers in the cooling system of the data centers.

Airside economizers are utilized to take advantage of favorable outdoor air (when outdoor temperature is lower than indoor temperature) to cool down the indoor environment while keeping the mechanical cooling system off. Since the data centers must be operated at 24/7, 365 days per year schedule, economizers can make use of low temperature air at nights to achieve free cooling and reduce the data centers operational cost. ASHRAE (American Society of Heating, Refrigerating and Air-Conditioning Engineers, Inc.) standard 90.1-2016 provides detailed requirements for the use of airside economizers [43].

There are also concerns from the data center operators that using airside economizers might contribute to IT equipment failures. The reasons are as follows:

- Introduction of outdoor air into the data centers might increase the contaminant concentrations in the airflow.
- The cycling on and off of the cooling system can cause rapid changes of relative humidity, which will facilitate condensation on the electronic surface.

In 2011, ASHRAE Technical Committee (TC) 9.9 published a white paper titled with "Gaseous and Particulate Contamination Guidelines For Data Centers" [44]. The document claimed that there is an increasing number of corrosion-related equipment failures found in the data centers located in the emerging market such as Asia Pacific and China (APAC) where unusually high concentrations of corrosive gases are observed.

3.1.2 Ag and Cu Corrosion under Harsh Environments

There are two common corrosion-related equipment failures caused by airborne contamination [44]:

- Copper and silver creep corrosion on the printed circuit boards (PCBs)
- Corrosion of silver termination in surface-mounted components

Cu is widely used in the PCBs due to its superior electrical conductivity. When the Cu surface is exposed to high sulfur-containing pollutants such as H_2S and SO_2, pure Cu metal will easily turn into Cu_2S. High concentrations of H_2S and SO_2 are usually found in places near paper factories and oil refineries. Creep corrosion occurs when copper sulfide migrates over the PCB surface without the influence of an electrical field, which leads to short circuit on the circuit board. Atmospheric corrosion behavior of Cu has been reviewed in many publications [45][46][47].

Tin-lead hot air solder level (HASL) is one of the most common surface finishes on the PCBs, which can protect the copper surface from deterioration and oxidization. It

has great solderability and desired resistance to corrosion. However, according to the restriction of hazardous substances (RoHS) directives adopted by the European Union in 2003, lead was forbidden in the electronic components or equipment. It took significant amount of time for PCB manufacturers to investigate and adopt alternative materials to replace lead-based surface finishes. Lead-free materials such as immersion silver (ImAg), immersion tin (ImSn), organic solder solderable preservatives (OSP), electroless nickel immersion gold (ENIG) have been considered as promising replacements for the traditional lead-tin finishes [48].

There is no existing perfect surface finish that can be used in all the situations and each surface finish has its own advantages and disadvantages [49]. Immersion silver (ImAg) has been used as one of the most desirable materials thanks to its maintaining solderability and good conductivity [50]. With ImAg, however, hardware has been shown to be more susceptible to harsh environments [48][51][52]. Exposure to highly polluted environments often results in visible tarnishing of coating and creep corrosion. The creeping of the corrosion products has been found as a major failure mode for electronic equipment in high sulfur environment [51][53]. The formation of silver sulfide under those conditions can also lead to loss of silver metallization and eventually open circuit on the PCBs. Ag corrosion in highly polluted environments therefore has gained an increased level of interest in the electronics industry recently.

The corrosion behavior of Ag in the atmosphere has been extensively studied for decades [46][54][55]. Ag corrosion is generally considered to be sensitive to UV light [56], H_2S [46][54] and oxidizing agents such as ozone and Cl_2 [56]. AgCl and Ag_2S are

the two most common corrosion products in the field, with Ag_2S usually dominating under indoor exposure [55].

Due to the fact that environmental contaminants are usually difficult to monitor and control, ISA (International Society of Automation) 71.04-2013 provides a classification system to evaluate corrosive potential of an environment towards electronic equipment based on Cu and Ag corrosion rates [57]. Pairs of Ag and Cu coupons were placed in data centers at various locations for 30 days and corrosion products thicknesses were calculated by cathodic reduction. Four levels of environmental severities (G1 Mild, G2 Moderate, G3 Harsh and GX Severe) are defined (see Table 3.1). With increasing level of severity, the corrosion probability in the environment escalates dramatically. Severity level G1 represents an environment that is sufficiently controlled and corrosion is not a factor to determine equipment reliability whereas for GX level, only specially designed and packaged equipment would be expected to survive.

Table 3.1 ISA 71.04-2013 Classification of reactive environments

Severity Level	G1	G2	G3	GX
	Mild	Moderate	Harsh	Severe
Copper Reactivity Level (in Å/month)	< 300	< 1000	< 2000	≥ 2000
Silver Reactivity Level (in Å/month)	< 200	< 1000	< 2000	≥ 2000

Equipment reliability has to be assessed before their deployment in any of these environments. However, atmospheric corrosion is a lengthy process and it usually takes relatively long time to see material degradation. Accelerated corrosion testing therefore has been developed to simulate corrosion behavior under certain environmental conditions (see section 3.2).

3.1.3 Relative Humidity Fluctuation Effect on Metal Corrosion

As mentioned in section 3.1.1, one of the concerns in the use of airside economizers is the rapid relative humidity fluctuations when the cooling system is cycling on and off. ISA71.04-2013 standard also posits that severity level can be increased by one level for a RH rate of change greater than 6% per hour. It suggests that cycling of the RH should be considered as a key factor to assess harsh environments. However, no experimental data or literature is provided to support this statement. Anecdotal evidence for the potential effect of RH cycling on the metal corrosion has been reported, where the corrosion rate in data centers with large humidity variations appears to be higher than data centers with small humidity variations [58]. However, contaminant species and their concentrations in these data centers were not monitored and controlled. It is unknown whether the corrosion rate difference observed between the different data centers is due to the difference in RH variation or corrosive gas concentrations. Testing with well-controlled conditions is therefore needed to fully understand the role of RH fluctuations on metal corrosion rate.

3.2 Accelerated Corrosion Testing

The equipment manufacture users can not afford to wait for a long period of time to test product reliability. To solve this issue, accelerated corrosion tests are developed to 1) simulate corrosion behavior of electronic equipment (or parts) under laboratory test conditions in a reasonable test period; 2) investigate effects of key parameters (such as gas concentrations, relative humidity, temperature etc.) in metal corrosion and propose corrosion mechanism. Clay test, flowers of sulfur test and mixed flowing gas test are the most commonly adopted accelerated corrosion testing in the electronic industry.

3.2.1 Clay Test

Clay test was discussed by R. Schueller [53] where the modeling clay was used as the sulfur containment to corrode printed wire assemblies (PWAs). Clay is usually wet with a small amount of water and placed in a container with tested samples. The container is heated by a microwave oven to 45-55°C where clay starts to produce sulfur vapor. The advantages of the clay test are that it can provide real sulfur contamination and is easy to setup. However, the clay test requires periodic heating and sulfur is the only corrosion contaminant, which is not adequate to fully simulate field corrosion.

3.2.2 Flowers of Sulfur (FOS)

Flowers of sulfur (FOS) test was initially used to test porosity of metallic coatings [59] and extensive studies were conducted to test electronics reliability based on the modified FOS chamber [60][61]. The FOS chamber contains flowers of sulfur and saturated potassium chloride solution, which serve as sulfur contamination and the humidity source respectively. Since the solution is saturated, relative humidity in the test chamber will keep at a known level at certain temperature. The FOS test requires relatively low setup cost and test variables are easily controlled.

3.2.3 Mixed Flowing Gas (MFG)

The mixed flowing gas (MFG) test has been developed since the late 1980s and is regarded as the most comprehensive corrosion test for electronic equipment [62]. Unlike other corrosion tests, which only have sulfur contamination, multiple sulfur-containing contaminants (H_2S, SO_2), nitrogen dioxide and molecular chlorine are involved in the MFG system. Relative humidity and temperature are also carefully controlled and

monitored. A MFG chamber is used in this work to study Ag and Cu corrosion behavior under different test conditions.

There are many MFG test conditions developed to simulate North American environmental conditions, such as Battelle [62] and Telcordia [63], which are generally followed in industry. One day Cu corrosion rate in a Telcordia environment can simulate one year Cu corrosion in an ISA71.04 G1 environmental condition [57]. However, these testing conditions have failed to represent the corrosion effects in the emerging market, especially the Asia Pacific and China (APAC) region [64].

To better simulate more aggressive environments for worldwide market, Nokia [65] has successfully developed a new test condition with significantly higher H_2S concentration (see Table 3.2). The reasons for increasing H_2S concentration are that 1) metal sulfides are found to be the most important corrosion products to cause creep corrosion in the field and 2) Cu corrosion rates are linearly dependent on the H_2S concentration up to 1700ppb.

Table 3.2 Gas concentrations of Telcordia and Nokia MFG tests

	H_2S	SO_2	NO_2	Cl_2
Telcordia	100 ppb	200 ppb	200 ppb	20 ppb
Nokia	1700 ppb	200 ppb	200 ppb	20 ppb

3.3 Project Objectives

The IPC 3-11g committee is working on adopting Nokia testing condition as an industry standard and has conducted a round robin testing (see Table 3.3) by using the same MFG condition. The relative humidity in the Nokia condition is ~69% and the temperature is 40°C.

Table 3.3 IPC 5 days MFG exposure round robin results

	CALCE*	Battelle	Nokia
Cu (nm)	~3720	~3780	~3670
Ag (nm)	~740	~350	~200

* Center of Advanced Life Cycle Engineering, University of Maryland

There are two questions raised from the round robin test results:

- Cu shows similar and consistent corrosion rates among the three labs, on the other hand, Ag corrosion rates show large variations. The Ag corrosion rate from CALCE is three times larger than the Nokia result.
- Cu corrosion rates are observed to be much higher than silver corrosion rates. However, it is reported that silver corrosion rates are poorly correlated with copper corrosion rates in field conditions [66].

To answer the first question, it is necessary to compare the differences of sample preparation and test conditions among the three labs. Through investigation, it is realized that all corrosive gases concentrations are well monitored during the MFG tests except Cl_2. Cl_2 is usually the first gas added into the MFG chamber and after the addition of the other three gases, Cl_2 concentration can not be monitored by the detector again. Historically, the Cl_2 concentration is assumed to be constant however this adds large uncertainties to the MFG test. Cu coupons are used to be the standard material to evaluate the corrosivity levels of the MFG conditions. The Cl_2 monitoring technology was not paid as much attention previously since Cu corrosion is not sensitive to Cl_2 concentration, especially under such high H_2S level (1700ppb). However, it is recognized that Cl_2 might play an important role in accelerated Ag corrosion. Therefore, one of the objectives of this work is to explore a reliable way to monitor Cl_2 concentration continuously during the MFG tests.

For the second question, where Ag corrosion rates are much lower than Cu, a new MFG test condition is needed for Ag corrosion to clarify discrepancies between field exposure and laboratory accelerated test. In order to achieve that, several key parameters on Ag and Cu corrosion in the MFG testing need to be investigated.

As mentioned before, ISA 71.04 -2013 claims that RH cycling will have an effect on the Ag and Cu corrosion rate, however a reliable and well-controlled laboratory test is needed to provide experimental results to validate the statement. In this work, for the first time RH fluctuations are achieved in the MFG chamber and the effect on the corrosion behavior of Ag and Cu are studied.

In summary, there are three project objectives in this work:

- Explore a reliable way to monitor Cl_2 concentration in-situ during the MFG tests.
- Investigate effects of different parameters (gas concentrations, RH and temperature) on accelerated Ag corrosion to initiate new MFG conditions for Ag.
- Examine the effect of RH cycling on Ag and Cu corrosion and provide operational guidelines to data centers.

3.4 Experimental Methods

3.4.1 MFG System Setup

The MFG system used in this work consists of a gas generation system, an exposure chamber and the monitoring system. Figure 3.1 shows the MFG chamber located in Nokia Bell Labs. The gas generation system has been described in detail elsewhere [67][68]. In order to achieve gas concentrations as low as few ppb, a stream of prepurified, dry air is used as the carrier gas to dilute the corrosive gases. RH in the chamber can be adjusted by passing a portion of this dry gas stream through a water

bubbler and is monitored continuously by a RH sensor in the chamber. There is a 0.5 L antechamber for premixing the gases before their injection into the chamber. This design allows even dispersion of gas mixtures. The internal gas concentrations after leaving the chamber are monitored using specific gas detectors. A gas sample dryer (PD-50T-12-MPP, Perma Pure LLC) is placed between the MFG chamber and the Cl_2 detector (SPM Flex, Honeywell) to adjust the RH of the mixed gas into the detector (Figure 3.2). Nafion® tubes are used in the dryer which show no absorption and extreme resistance to the corrosive gases in the MFG chamber.

Figure 3.1 MFG chamber located in Nokia Bell Labs.

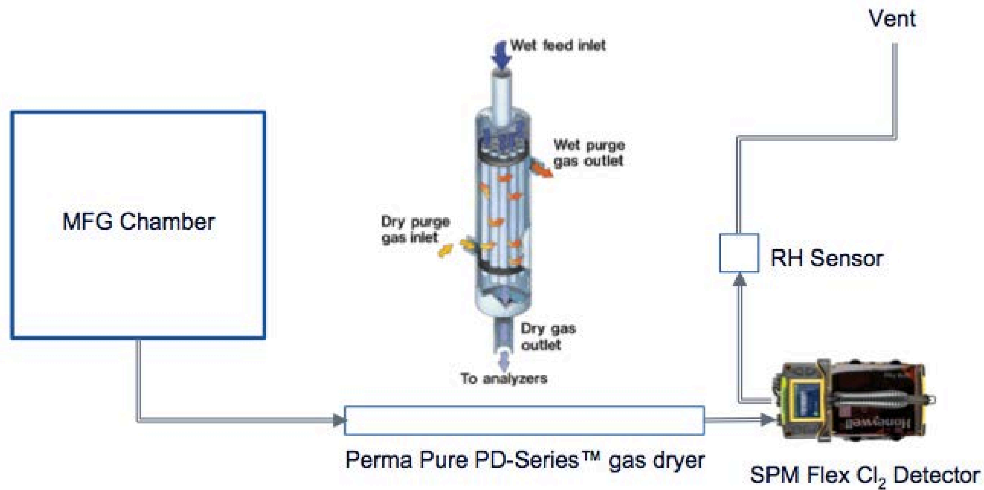

Figure 3.2 A gas dry placed between the MFG chamber and the Cl_2 detector to adjust the RH of sample gas into the detector.

3.4.2 In-situ Cl_2 Monitoring Method

In order to understand the effect of the Cl_2 on accelerated Ag and Cu corrosion in the MFG test, it is essential to monitor the Cl_2 concentration reliably and continuously during test. However, historically Cl_2 has not been monitored in-situ during the MFG test and is generally preset before the other gases are added into the chamber. There are two possible reasons why Cl_2 concentration can not be monitored continuously: 1) Cl_2 concentration is relatively low compared with the other corrosive gases; 2) there are interference effects of other gases on the Cl_2 concentration.

There are several commercial Cl_2 detecting technologies available and Chemcassette® (Paper tape) technology from Honeywell is used as the Cl_2 detector in our tests [69]. Figure 3.3 shows the schematic and working mechanism of this type of detector.

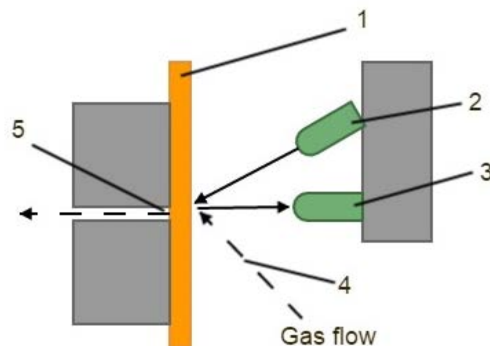

Figure 3.3 Schematic of the Cl_2 detector. (1) Chemcassette® tape (2) LED light which can illuminate sample stain (3) Detector (4) Sample inlet (5) Sample outlet [70].

In the detector, the Cl_2 gas in the sample flow reacts with the Cl_2 Chemcassette® tape and forms a stain where optical density is proportional to the Cl_2 concentration. The operational RH is 30-55% according to the user manual, which suggests that there might be a potential relationship between sample gas RH and detected Cl_2 concentration.

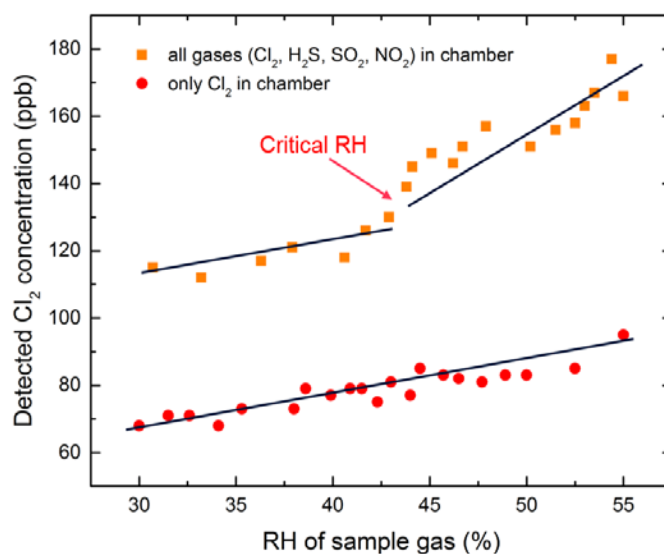

Figure 3.4 Detected Cl_2 concentration from the Chemcassette® detector as a function of sample gas RH under two conditions: all gases present in the chamber (orange) and only Cl_2 in the chamber (red) [70].

To verify this hypothesis, the Cl_2 flowmeter is set and detected Cl_2 concentration from the detector as a function of sample gas RH is recorded (Figure 3.4) under two conditions: 1) Cl_2 is the only gas in the chamber and 2) all gases present in the chamber. When Cl_2 is the only gas present in the chamber, the detected concentration is slightly dependent on the sample gas RH. This result is in good agreement with data provided by the vendor that shows accuracy to within ±20% when RH is between 35-55%. However, when all gases are in the chamber, detected Cl_2 concentration starts increasing dramatically above 40% RH. A possible explanation for this difference is that above this critical RH, the Chemcassette® (paper tape) starts absorbing moisture and becomes susceptible to reaction of H_2S and Cl_2. Since the reaction product, elemental sulfur, is a yellow solid, stain density on the tape will be increased, which therefore falsely indicates an increase in the Cl_2 concentration in the detector. For the conditions below the critical RH, interference effect of the other gases on Cl_2 concentration can still be observed. An interference factor of 1.6 under these gas concentrations is calculated from experimental data. Therefore, we realize that sample gas RH should be carefully controlled during experiments to reliably monitor Cl_2 concentration in the chamber. In the following experiments, the RH of the sample gas is kept constant and set at 35% by adjusting N_2 flow rate in the gas dryer between the MFG chamber and the Cl_2 detector.

3.4.3 Test Conditions for Accelerated Ag and Cu Corrosion in the MFG Chamber

Pure Ag and Cu coupons (Alfa Aesar 99.998% purity) are cut to 0.1mm (thickness) × 2cm (width) × 5cm (length) in size. Coupons are first ultrasonically cleaned in acetone for 5 minutes to remove organic contaminants. Then they are rinsed

by isopropanol followed by DI water. After that, a 5 vol % HNO_3 is used to remove oxides on the coupons before chamber exposure.

Table 3.4 shows seven different test conditions used in the MFG chamber. For all test conditions, H_2S concentration is 1700ppb and SO_2 concentration is 200ppb. Test conditions I and II compare the effect of Cl_2 concentration on Ag and Cu corrosion and test conditions II and III examine the effect of RH. Test IV assesse the effect of NO_2 and test V address the effect of combination of high Cl_2 concentration and high NO_2 concentration. Test conditions VI and VII evaluate the effect of the temperature in the MFG chamber.

For test conditions I to V, one pair of Ag and Cu coupons is placed close to each other and vertically in the chamber at the same time. For test conditions VI and VII, three pairs of Ag and Cu coupons are put in the back, middle and front of the chamber for uniformity validation. Gas concentrations, RH and temperature in the chamber are routinely monitored and recorded during exposure to ensure all these parameters are constant. Cl_2 concentrations shown in Table 3.4 are measured with all gases in the chamber and are corrected by the interference factor.

Table 3.4 Test conditions for accelerated Ag and Cu corrosion in the MFG chamber

Test Condition	Cl_2 Gas Concentration*	NO_2 Gas Concentration	RH	Temperature
I	20 ppb	200 ppb	66%	40°C
II	95 ppb	200 ppb	66%	40°C
III	95 ppb	200 ppb	82%	40°C
IV	20 ppb	700 ppb	66%	40°C
V	95 ppb	850 ppb	66%	40°C
VI	50 ppb	200 ppb	66%	40°C
VII	50 ppb	200 ppb	66%	30°C

* Cl_2 concentrations are measured with all gases in the chamber and are corrected by the interference factor.

Four different exposure times (2 hours, 24 hours, 40 hours and 72 hours) are performed for test conditions I to V. Experiments of 5 hours and 10 hours are added to test condition I in addition to the above times. Test conditions VI and VII are only run for 72 hours.

3.4.4 RH Cycling Experiments

The initial MFG system is designed to perform accelerating tests under constant RH condition. In order to conduct RH cycling experiments, a solenoid valve with an automatic timer is added to the system. There are three ports in this solenoid valve and port 3 is connected with a 0.5L antechamber, which allows premixing of corrosive gases and carrier gas before injection into the MFG chamber. Figure 3.5 shows a schematic of MFG system and flow diagrams for achieving RH fluctuations. Eight L/min (LPM) dry and prepurified air is used as carrier gas and injected into system. When the solenoid valve is in the ‘off’ position, ports 2 and 3 are open and port 1 is closed. In this scenario, carrier gas enters into MFG system and a portion of dry air is diverted into a water bubbler to uptake moisture. After humidified air and dry air join together, the mixture exits from port 2 to port 3. The ratio between dry air and humidified air can be controlled by adjusting the flowmeter. Consequently, maximum RH in a RH cycling experiment is determined. When the solenoid valve is turned on, port 2 is closed and ports 1 and 3 are open. Carrier gas then flows through port 1 directly to port 3. In this case, RH in chamber decreases owing to increasing amount of dry air in MFG chamber. The timer is used to automatically switch ‘on’ and ‘off’ positions of the solenoid valve, which subsequently determines the duration of one RH cycle and the minimum RH that can be achieved. Concentrations of corrosive gases are monitored using commercial gas detectors after

leaving the chamber. A RH sensor is placed along with coupons to routinely monitor the local RH and temperature in the MFG chamber every 30 seconds during experiments.

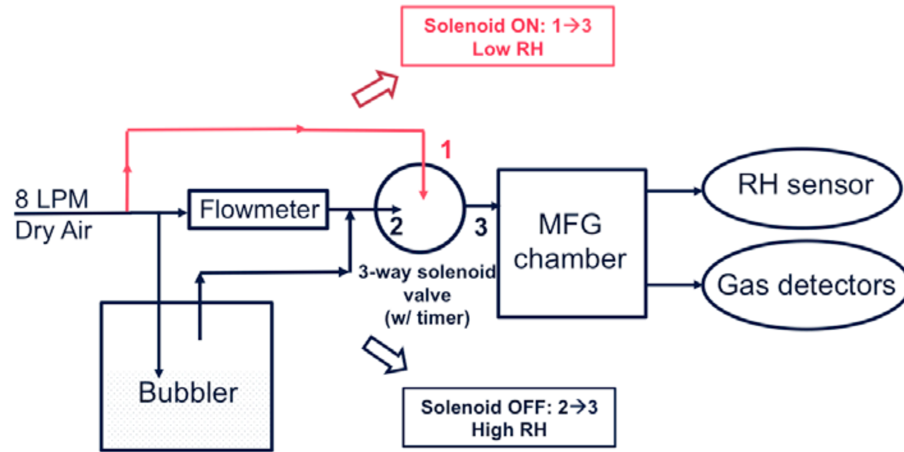

Figure 3.5 Schematic diagram of the MFG system with a 3-way solenoid valve for RH cycling experiments (corrosive gases generation system and antechamber are not shown).

Three RH cycling conditions are set as follow: 1) 52%-35% (maximum RH — minimum RH); 2) 60%-38%; 3) 70%-40%. Each RH cycle is set at 20 mins. Gas concentrations in the MFG chamber are set close to field conditions in challenging environments (see Figure 3.6 (b)), which minimizes possible accelerating effect of high concentration gases on Ag and Cu corrosion but also generates enough corrosion products in two days exposure to be analyzed. Coupons are exposed for 2 days in the MFG chamber under all cycling conditions.

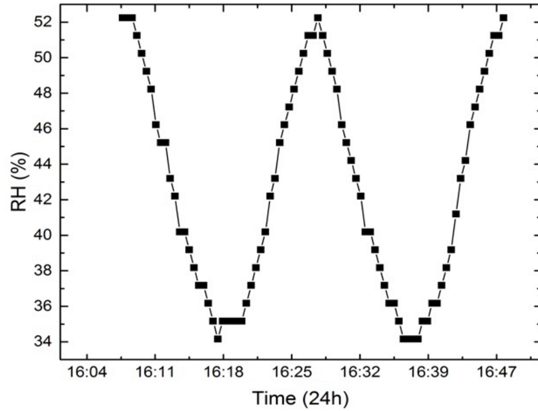

(a)

Gas	Concentration (ppb)
H_2S	50
NO_2	200
Cl_2	20
SO_2	100

(b)

Figure 3.6 (a) 52%-35% RH cycles measured by the RH sensor (only two cycles are shown here). Each cycle is 20 mins and data point is recorded every 30 seconds; (b) Corrosive gas concentrations used in the MFG chamber.

3.4.5 Test Methods for Corrosion Products Quantification

3.4.5.1 Weight Gain Measurement

Weight gain measurement has been widely used to quantitatively determine the mass of corrosion products of Ag or Cu coupons [71]. Well-prepared metal coupons are carefully weighted on a Mettler UTM2 microbalance with 50 μg accuracy before and after exposure in the MFG chamber. A platinum reference weight is used as calibration each time before measurements, and each sample is weighted up to five times. Coupon weight gain is normalized by the coupon area. The weight gain measurement is the most adopted and easiest technique to calculate coupon corrosion rate whereas it can not determine the composition of the corrosion products.

3.4.5.2 Cathodic Reduction

Cathodic reduction (CR) is useful in determining and quantifying compositions of corrosion products. In cathodic reduction, a fixed current is applied to the sample in the electrolyte and resulting variations in potentials are followed as a function of time. A

typical potential vs. time plot will have a number of plateaus and each plateau indicates the reduction potential for a specific substance. Two platinum counter electrodes and a saturated calomel reference electrode (SCE) are used in CR. A 0.1 M KCl solution is used as electrolyte and prepared 24 hours in advance. The KCl solution is deoxygenated by bubbling with N_2 for at least 60 mins before experiments. A PAR 273 (Princeton Applied Research) potentiostat is used to apply the constant reduction current to the sample and to record resulting variations in potentials.

3.4.5.3 Other Analytical Techniques

Scanning electron microscope (SEM) is utilized to compare surface morphology between corrosion products under various testing conditions. Energy-dispersive X-ray spectroscopy (EDX) is also used to compare chemical compositions of corrosion products.

3.4.6 Chamber Validation

Before the actual test conditions are conducted, experiments are performed to validate the MFG results accuracy. Test condition is shown in Table 3.5. Three runs are repeated in the validation tests and for each run, three pairs of Ag and Cu coupons are put in the front, middle and back of the MFG chamber. Figure 3.7 shows that less than 6% error are found for both Ag and Cu MFG results and therefore chamber repeatability and uniformity are confirmed.

Table 3.5 MFG test condition for chamber validation

H_2S	SO_2	NO_2	Cl_2*	RH	Temperature	Time
1000 ppb	200 ppb	1000 ppb	30 ppb	69%	30°C	2 days

* Cl_2 concentrations is measured with all gases in the chamber and is corrected by the interference factor.

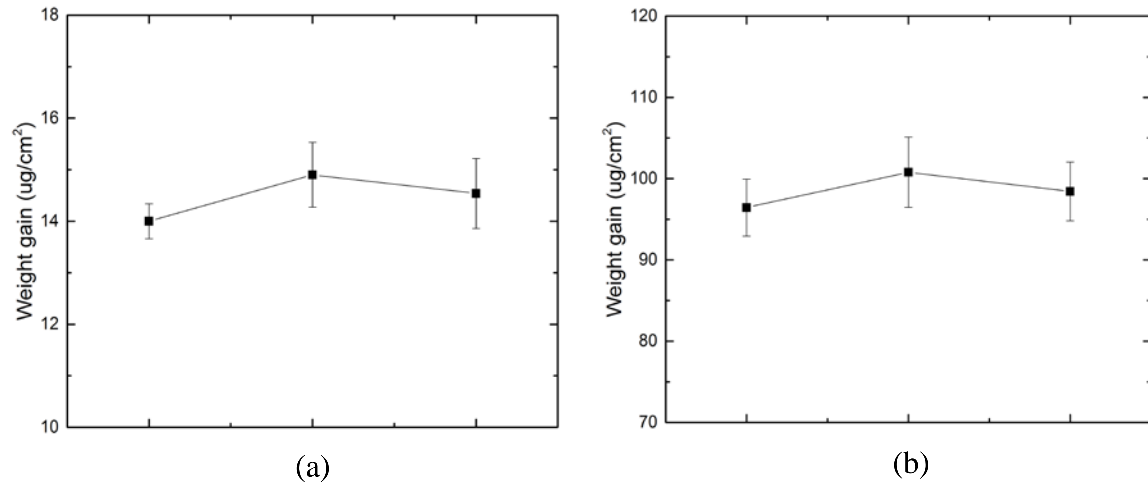

Figure 3.7 Ag (a) and Cu (b) corrosion rates for chamber validation experiments. Each data point shows result from one run.

3.5 Results and Discussion

3.5.1 Effects of Cl_2 Concentration on Accelerated Ag and Cu Corrosion

Figure 3.8 presents the weight gain per area of Ag and Cu coupons after exposure in the MFG chamber under test conditions I and II. All parameters except for the Cl_2 concentrations are the same under these two conditions where condition I has 20 ppb Cl_2 and condition II has 95 ppb Cl_2. As shown in the plot, Ag corrosion kinetics conforms to a parabolic behavior under condition I. However, the kinetics in condition II conforms to a linear law and corrosion rate is much larger than the one in condition I. This suggests that under low Cl_2 concentration, reaction of Ag with H_2S slows down after formation of

sulfide and diffusion of H_2S into the corrosion layer is the rate-controlling step for Ag corrosion. Under high Cl_2 concentration, however, the oxidation of H_2S by Cl_2 on the Ag surface is likely the controlling step. The reaction product, elemental sulfur, can react with Ag to form Ag_2S. Equation (3.1) and (3.2) show the proposed surface reaction mechanism for Ag corrosion under 95 ppb Cl_2. For Cu coupons, corrosion rates show no significant difference between 20 ppb and 95 ppb Cl_2 concentrations. This can be explained by the Cu corrosion mechanism proposed by Sandia National Lab [72]. Figure 3.9 shows that when bare Cu surface is exposed to water and oxygen, a thin Cu_2O layer will form on the Cu surface. [Cu^+] can diffuse through corrosion layers and react with available sulfur contaminants on the surface. The diffusion rate of [Cu^+] is quite high so that it can sustain the sulfidation and corrosion rate therefore is determined by the high H_2S concentration and insensitive to Cl_2 concentration.

$$H_2S + Cl_2 \rightarrow S + 2HCl \quad (3.1)$$

$$Ag + S \rightarrow Ag_2S \quad (3.2)$$

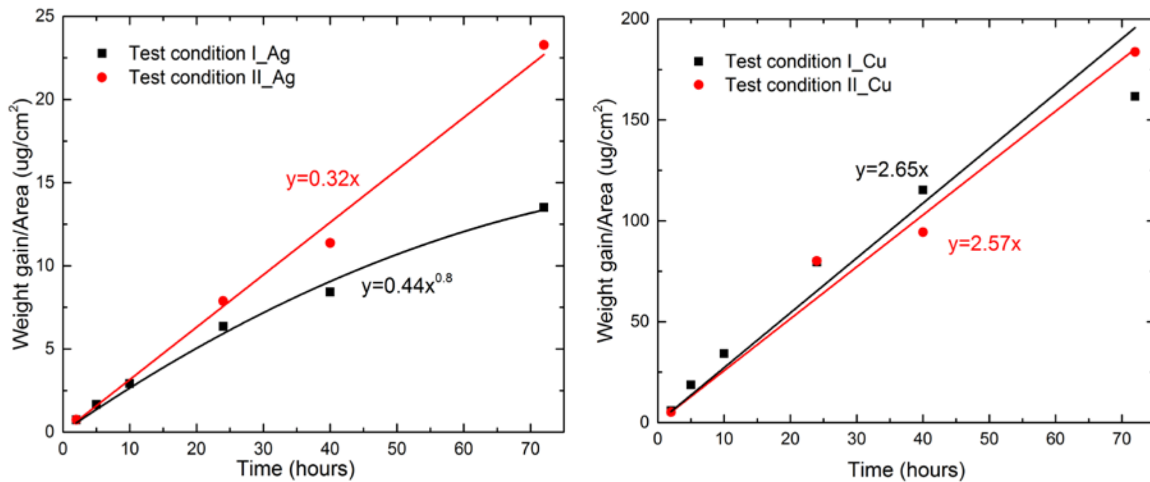

Figure 3.8 Weight gain per area of Ag (left) and Cu (right) coupons under condition I (black, 20 ppb Cl_2) and II (red, 95 ppb Cl_2) [70].

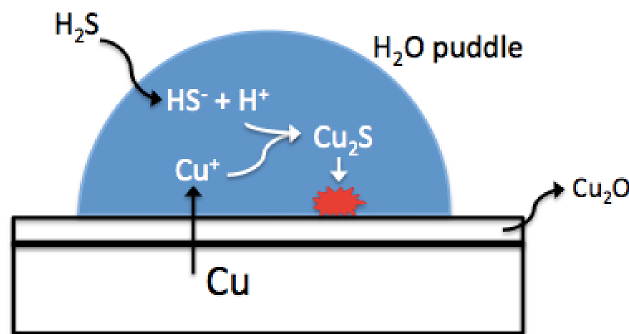

Figure 3.9 Schematic of Cu corrosion mechanism.

Cathodic Reduction is performed on the Ag and Cu coupons exposed to 40 hours in the chamber under test conditions I and II. Depending on the estimated amount of corrosion products, the current density of -0.03mA/cm^2 and -0.19mA/cm^2 are applied to Ag and Cu respectively.

Reduction curves of Ag and Cu are shown in Figure 3.10. For Ag coupons, two evident reduction plateaus are found in both conditions. It is reported that Ag_2S is reduced at -0.78 V vs SCE before hydrogen evolution reaction (HER) occurs at -1.29 V [73][74]. Therefore, the majority of reduction products are Ag_2S under both Cl_2 concentrations. It has been previously reported that the latter plateau at -1.18 V vs SCE has not been assigned to any specific compound and this plateau is reported to always appear after reduction of Ag_2S [74]. For Cu coupons, there are also two evident reduction plateaus before HER: plateau near -0.83 V vs SCE is assigned to Cu_2O and plateau near -1.13 V vs SCE represents reduction of Cu_2S [75]. CR results suggest that high Cl_2 concentration do not change Ag and Cu corrosion products but just accelerates Ag sulfidation.

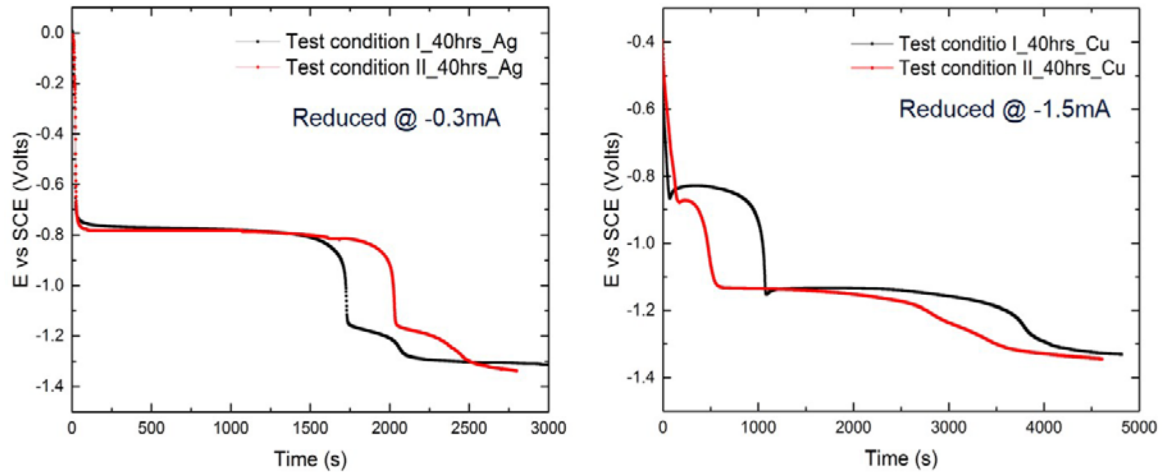

Figure 3.10 Cathodic reduction plots for Ag (left) and Cu (right) after 40 hours exposure in the MFG chamber under test conditions I (black, 20 ppb Cl_2) and II (red, 95 ppb Cl_2) [70].

The mass of the corrosion product can be calculated following equation (3.3) [76].

$$W = it\frac{10^3 M}{NF} \tag{3.3}$$

where W is mass in microgram, i is current in milliamps, t is time to reduce a known substance in seconds, M is gram-molecular weight of reduced substance, F is Faraday's constant (9.65×104 C) and N is number of faradays to reduce a gram-molecular weight of reduced substance.

Table 3.6 compares calculated masses of the corrosion products of Ag and Cu coupons after 40 hours exposure in the MFG chamber by using weight gain and CR. Results from the two techniques reasonably agree with each other.

Table 3.6 Mass comparisons for corrosion products of Ag and Cu after 40 hours exposure in MFG

	Ag		Cu			
		Ag_2S (mg)		Cu_2O (mg)	Cu_2S (mg)	Total (mg)
Test Condition I	Weight gain	0.14	Weight gain	NA	NA	1.99
	CR	0.14	CR	0.27	1.68	1.95
Test Condition II	Weight gain	0.19	Weight gain	NA	NA	1.75
	CR	0.18	CR	0.12	1.54	1.66

Figure 3.11 shows the surface morphology of Ag coupons after different exposure times under test conditions I and II. Only original metal roughness can be observed after 2 hours in the exposure chamber for both conditions. Morphology differences start to be seen after 24 hours exposure with the appearance of a few needle shaped particles on the Ag surface at the 95ppb Cl_2 condition. A more significant morphology difference is seen after 72 hours exposure in the MFG chamber, when it is evident that large particles (spikes) of the corrosion products are formed on the Ag surface under high Cl_2 condition.

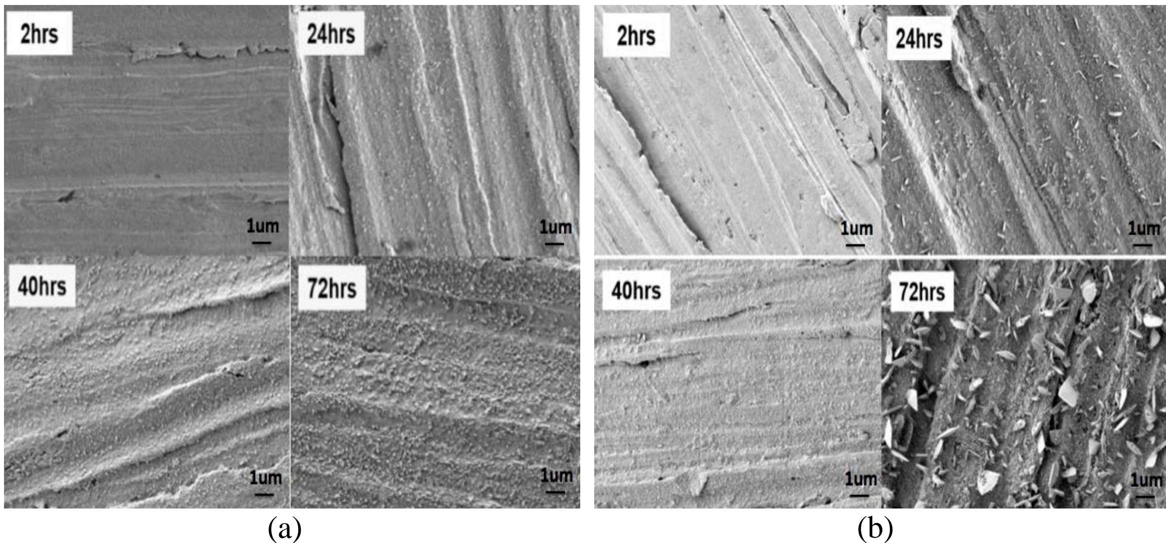

Figure 3.11 The surface morphology comparisons of Ag coupons during different exposure times in the MFG chamber under test conditions I (a) and II (b) [70].

3.5.2 Effects of NO_2 Concentration on Accelerated Ag and Cu Corrosion

Weight gain per area of Ag and Cu coupons due to exposure in the MFG chamber under test conditions I and IV are demonstrated in Figure 3.12. The NO_2 concentration is 200ppb in condition I and 700ppb in condition IV. For Ag coupons, corrosion rate under test condition IV is much higher than the rate under test condition I. The corrosion kinetics is linear under the high NO_2 concentration; however, the kinetics conforms to parabolic behavior under the low NO_2 concentration. This validates results from earlier work where synergistic effect of H_2S and NO_2 on Ag corrosion in MFG was first addressed [77]. NO_2, as the second oxidant in the MFG chamber other than Cl_2, can react with H_2S to form elemental sulfur. Formation of Ag_2S therefore is facilitated and controlled by this oxidation reaction. NO_2 concentration has, however, a negligible effect on Cu corrosion. This is due to the fact that Cu sulfidation is determined by high H_2S concentration and variation of NO_2 has a minor effect on the corrosion rate.

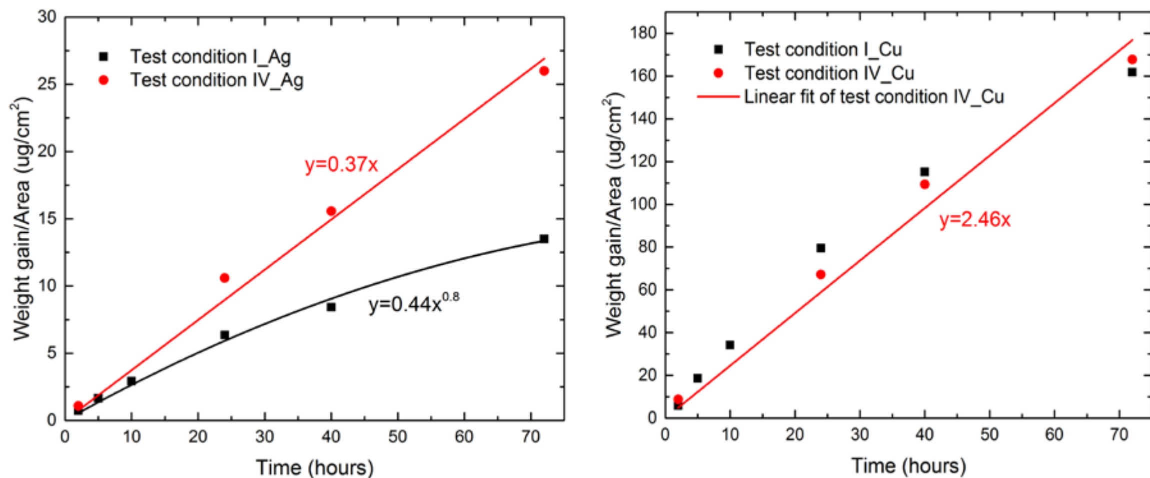

Figure 3.12 Weight gain per area of Ag (left) and Cu (right) coupons under conditions I (black, 200ppb NO_2) and IV (red, 700ppb NO_2) [70].

3.5.3 Effects of High Cl_2 with High NO_2 Concentration on Ag and Cu Corrosion

Figure 3.13 shows the weight gain per area of Ag and Cu coupons after exposure to the MFG test conditions I and V. Condition I has Cl_2 concentration of 20 ppb and NO_2 concentration of 200 ppb whereas condition V has Cl_2 concentration of 95 ppb and NO_2 concentration of 850 ppb. For Ag coupons, corrosion rate is much greater under high Cl_2 and NO_2 concentrations than the rate under relatively low Cl_2 and NO_2 concentrations. After 72 hours exposure, the corrosion under the test condition V is about 3 times larger than that under the test condition I. This is due to the synergistic effect of both Cl_2 and NO_2 with H_2S on accelerating Ag corrosion in the MFG chamber. The Cu corrosion rate is, however, found to have insignificant dependence on Cl_2 and NO_2 concentrations under short exposure time. After 72 hours exposure, however, the Cu corrosion rate in condition V increases dramatically compared with condition I. This result is inconsistent with the results under shorter exposure time and still under investigation.

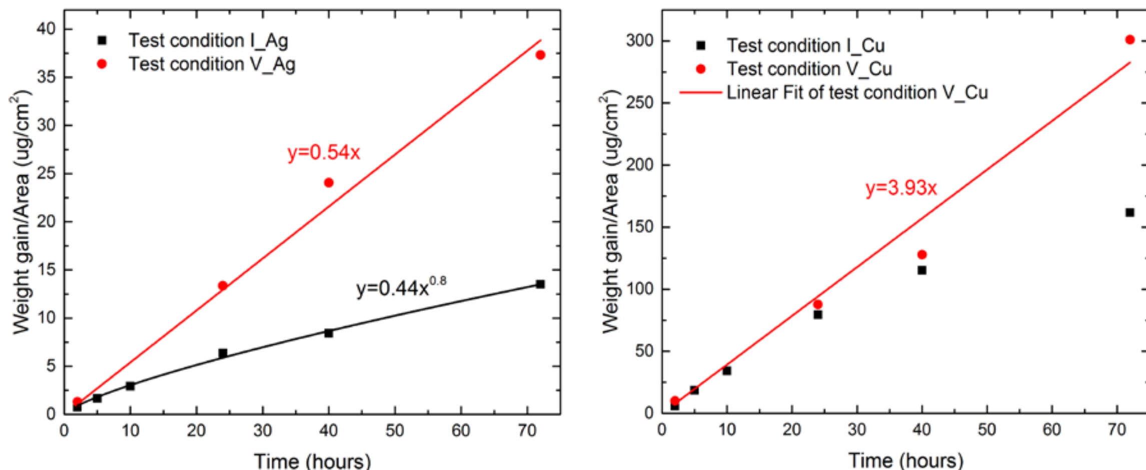

Figure 3.13 Weight gain per area of Ag (left) and Cu (right) coupons under conditions I (black, 20 ppb Cl_2 and 200 ppb NO_2) and V (red, 95 ppb Cl_2 and 850 ppb NO_2) [70].

3.5.4 Effects of RH on Accelerated Ag and Cu Corrosion

Figure 3.14 demonstrates the weight gain per area of Ag and Cu coupons due to exposure to the test conditions II and III in the MFG chamber. In these two conditions, all parameters are the same except the RH is 66% in condition II and 82% in condition III. By comparing the weight gain plots in this range, changes in RH have minor effect on Ag corrosion rate. This might be due to the fact that Ag is directly attacked by reactive sulfur and H_2O is not one of the reactants. However, for Cu coupons, higher RH shows slightly stronger acceleration in the Cu corrosion rate which is in good agreement with previous literature that atmospheric Cu corrosion is sensitive to RH. The possible reason is that at higher RH, more layers of water are present on the Cu surface and more chemically active $[HS^-]$ and $[H^+]$ are formed for Cu sulfidation.

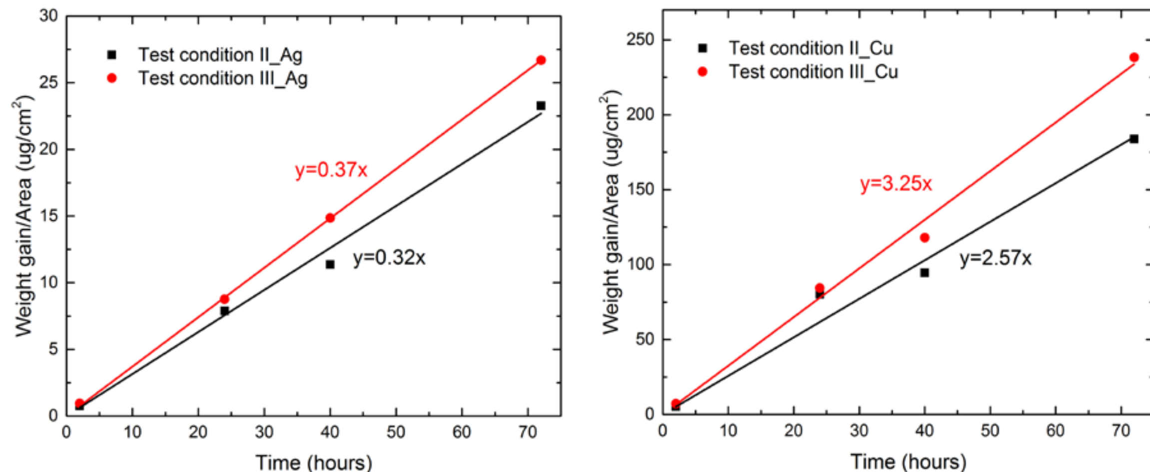

Figure 3.14 Weight gain per area of Ag (left) and Cu (right) coupons under conditions II (black, RH = 66%) and III (red, RH = 82%) [70].

EDX is used to compare chemical compositions of Ag and Cu corrosion products under different RHs. Table 3.7 shows atomic ratio of O, S and Cl for Ag and Cu coupons after 24 hours exposure in the MFG chamber under conditions II and III. For both metals,

elemental compositions of corroded films exposed to different RHs are virtually identical. Corrosion products are mainly silver sulfide or copper sulfide and the presence of Cl is due to exposure to high Cl_2 concentration.

Table 3.7 Atomic ratios of O, S and Cl for Ag and Cu coupons after 24 hours exposure in the MFG chamber under condition II (RH = 66%) and III (RH = 82%)

	Ag		Cu	
Atomic ratio (%)	Condition II	Condition III	Condition II	Condition III
O	2.88	2.63	2.56	3.04
S	13.68	12.95	20.59	19.25
Cl	0.52	0.45	4.34	2.71

3.5.5 Effects of Temperature on Accelerated Ag and Cu Corrosion

Figure 3.15 presents weight gain per area of Ag and Cu coupons exposed for 72 hours in the MFG chamber under test conditions VI and VII. The temperature in condition VI is 40°C whereas in condition VII is 30°C. Three pairs of Ag and Cu coupons are placed in the chamber under two test conditions and error bars are calculated. As shown in the plots, weight gains of Ag and Cu coupons do not have significant difference between 30°C and 40°C. The effect of decreasing temperature on corrosion rates might be compensated by the increase of solubility of the corrosive gases in water under the specific test condition. These results suggest that the temperature in the MFG chamber can be maintained at 30°C rather than 40°C to achieve similar corrosion results. Lower temperature in chamber will make the Cl_2 measurement less challenging since there will be less water condensation in the Teflon tubing between the MFG chamber and the Cl_2 detector.

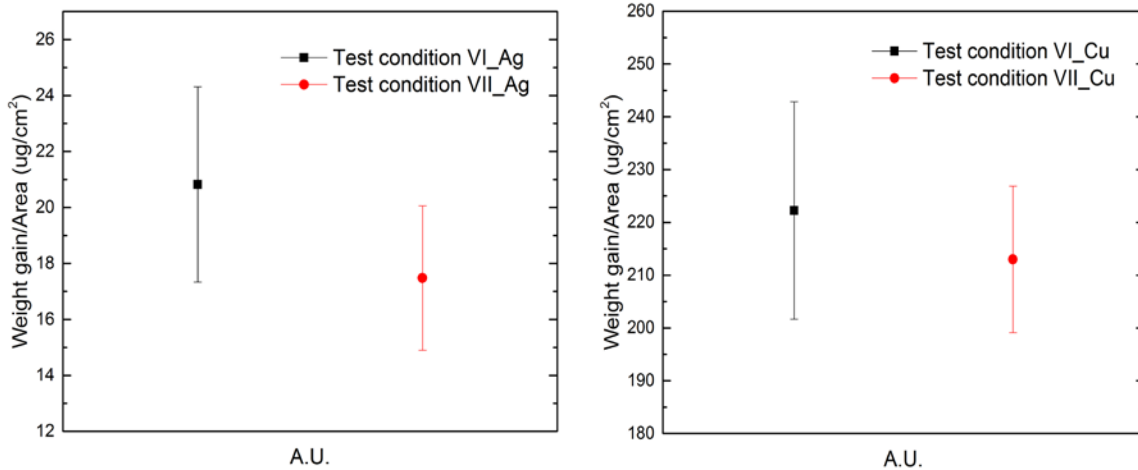

Figure 3.15 Weight gain per area of Ag (left) and Cu (right) coupons after 72 hours exposure in the MFG chamber under conditions VI (black, T = 40°C) and VII (red, T = 30°C) [70].

3.5.6 Effects of RH Cycling on Ag and Cu Corrosion

In order to eliminate the possible acceleration effect of highly corrosive gas concentrations, the MFG condition used in RH cycling effect is different than the previous accelerated experiments (see Figure 3.6 (b)). The weight gain plots of Ag and Cu coupons exposed for 2 days in the MFG chamber under RH fluctuation and constant RH conditions are presented in Figure 3.16. There are three examined cycling ranges and each cycling time is 20 mins. This allows 144 cycles to be run in 2 days and makes relative RH rate of change per hour as high as 102%, 132% and 180% respectively for the three tested conditions.

As we compared weight gains per coupon area, corrosion rates for both Ag and Cu do not increase due to RH cycling compared with maximum RH conditions for all ranges. These results indicate that corrosion rates are only determined by the level of RH rather than cycling of RH. In the second cycling condition where RH ranges from 60% to 38%, 52% RH results are used as maximum RH to compare because there is no

significant difference on Ag and Cu corrosion rates between 52% and 60% RH [46]. The Ag corrosion rate under constant 35% RH is slightly higher than 52% RH and 52%-35% cycling conditions. This shows agreement with SEM results that at 35% RH, the Ag surface has more nucleation sites than in the other two conditions (see Figure 3.18). It is clearly observed in the plots that Ag corrosion rate shows a weak dependence on RH whereas for Cu, corrosion rate is escalated at high RH (70%) compared with 35% RH condition. The decrease of corrosion nucleation density on Ag surface with increasing relative humidity may be related to the transition from direct chemical reaction between Ag and H_2S to an electrochemical reaction between Ag and H_2S.

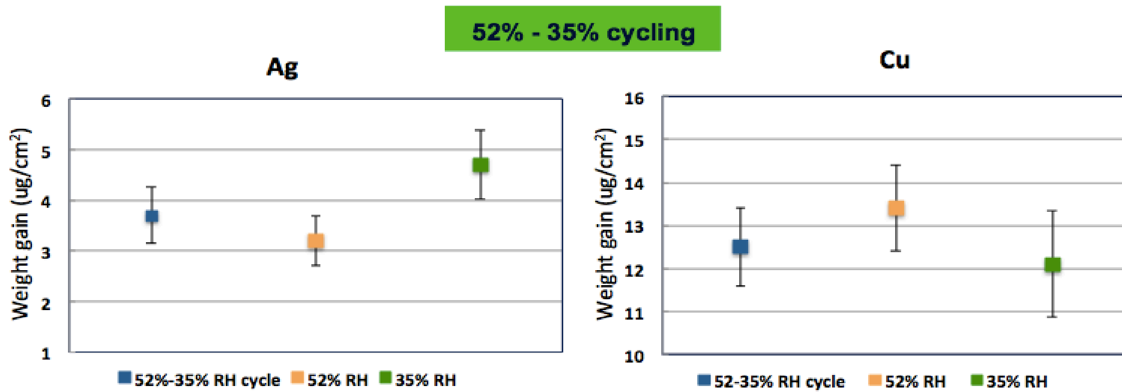

(a)

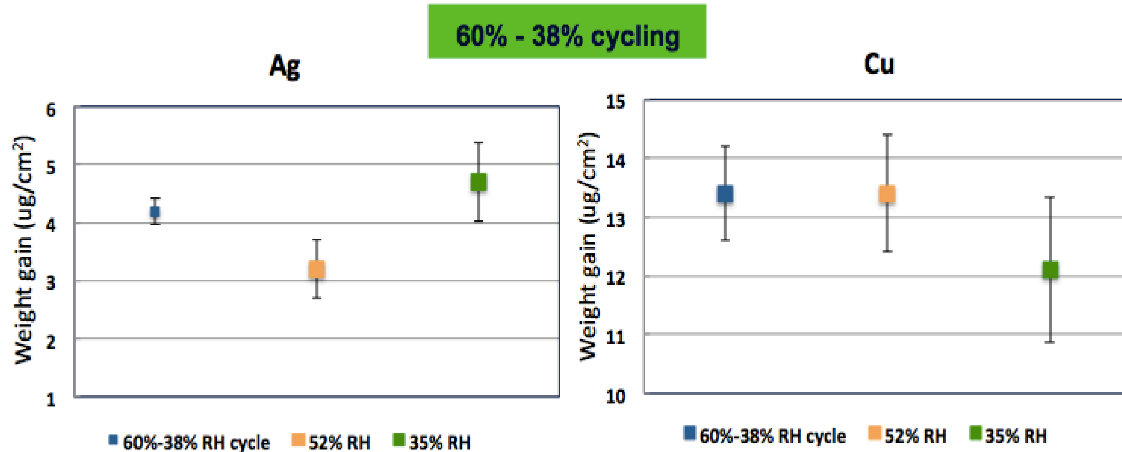

(b)

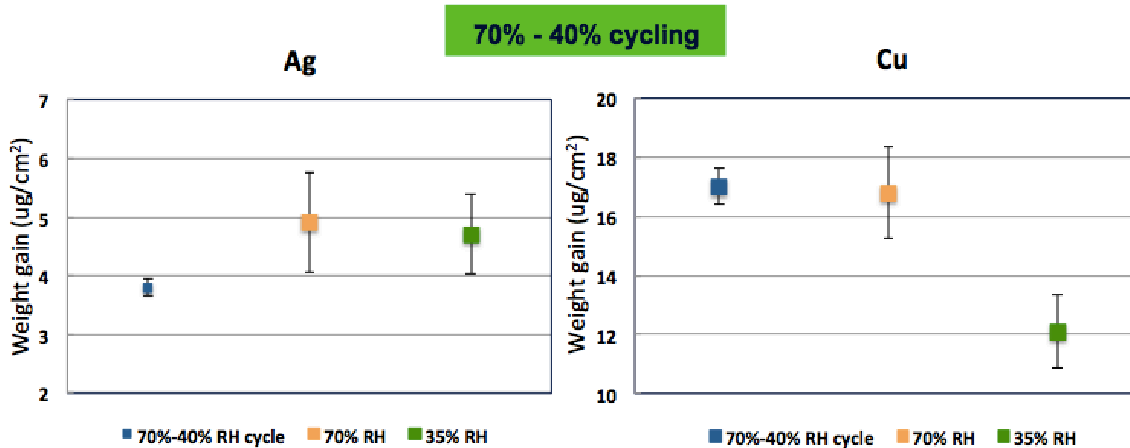

(c)

Figure 3.16 Comparisons of weight gain per area plots of Ag and Cu coupons after 2 days chamber exposure under RH cycling conditions and constant RH conditions.

Figure 3.17 shows cathodic reduction plots for exposed Ag (a) and Cu (b) coupons after 52%-35% RH cycling exposure and constant 52% and 35% RH exposures. Two reduction plateaus are observed for Ag coupons under all three conditions. This suggests that RH cycling do not change corrosion products of Ag. The substance reduced at -0.7 V vs SCE is Ag_2S and the compound reduced at +0.09 V vs SCE is regarded as AgCl. The existence of Cl is further confirmed by a Cl peak in the EDX spectra, which will be discussed later. Cu CR plots are not as straightforward as the Ag CR plots and three reduction plateaus (A, B and C) are presented in each RH condition. There are conflicting reviews regarding reduction order of Cu oxides [78][79]. However, Nakayama et al. [80] clarified that in 0.1 M KCl, CuO is first reduced followed by the reduction of Cu_2O, which assigns plateau A to CuO and plateau B to Cu_2O. He also mentioned that reduction of CuO and Cu_2O occur simultaneously, to some extent, in 0.1 M KCl, which explains different reduced potentials of oxides in different RH conditions. Plateau C is assigned to Cu_2S, which is reduced at -1.0 V vs SCE. The mass of the

corrosion product can be calculated using equation 3.3. Table 3.8 and Table 3.9 compare calculated masses and thicknesses of corrosion products of Ag and Cu under 52%-35% RH cycling condition by using weight gain and CR. Cu_2O is assumed as the only oxide in CR calculation for simplicity. Bulk density is used for calculating film thickness. CR reveals the actual composition of Ag and Cu corrosion products and the calculation results are internally consistent with weight gain measurements.

Table 3.8 Comparison of Ag corrosion products weight gain and thickness after 2 days exposure in MFG under 52%-35% RH cycling by different techniques

Ag	**Mass gain of corrosion product (mg)**			**Thickness of corrosion product (nm)**		
Method	Ag_2S	AgCl	Total	Ag_2S	AgCl	Total
Weight gain	NA	NA	0.059	NA	NA	40
CR	0.037	0.025	0.062	25	12	37

Table 3.9 Comparison of Cu corrosion products weight gain and thickness after 2 days exposure in MFG under 52%-35% RH cycling by different techniques

Cu	**Mass gain of corrosion product (mg)**			**Thickness of corrosion product (nm)**		
Method	Cu_2S	Cu_2O	Total	Cu_2S	Cu_2O	Total
Weight gain	NA	NA	0.21	NA	NA	118
CR	0.08	0.07	0.15	42.4	68.4	110.8

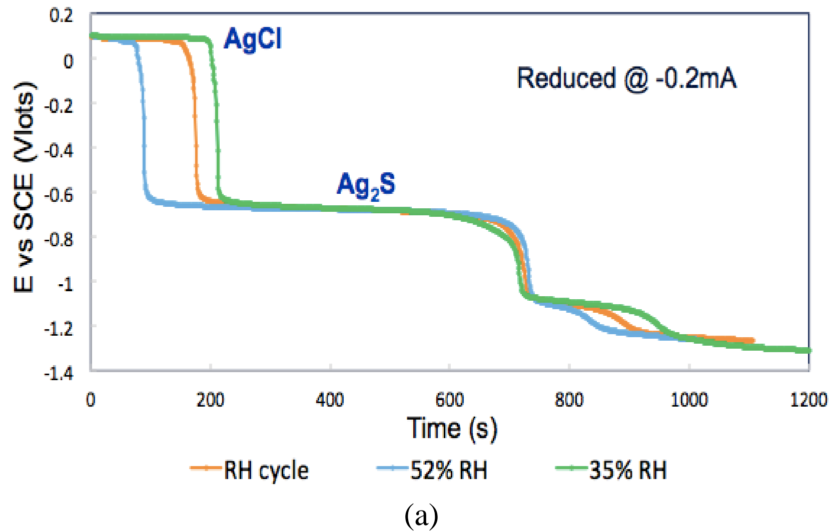

(a)

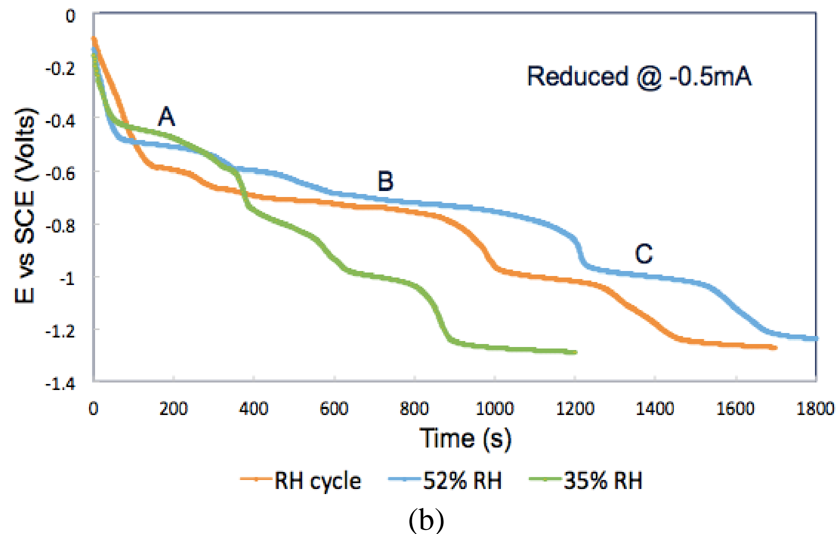

(b)

Figure 3.17 Cathodic reduction plots for corroded Ag (a) and Cu (b) coupons under 52%-35% RH cycling condition and constant 52% and 35% conditions.

Surface morphology changes of Ag coupons after 2 days exposure to MFG chamber under 52-35% RH cycling and constant RH conditions are shown in Figure 3.18. It is found that RH cycling do not change Ag coupon morphology significantly compared with constant RH. There are more nucleation sites on the surface at 35% RH, which is consistent with the weight gain results where the corrosion rate under this RH is higher than other conditions. Interestingly, the density of nucleation sites for the sample under RH cycling exposure is between those of the constant minimum and maximum RH.

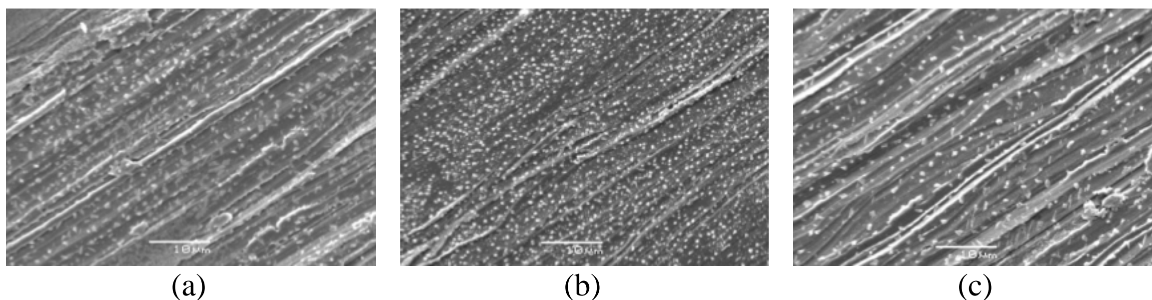

(a) (b) (c)

Figure 3.18 Surface morphology of Ag coupons after 2 days exposure in MFG chamber at (a) 52%-35% RH cycling, (b) constant 35% RH and (c) constant 52% RH. Scale bar is 10 μm.

EDX spectra of Ag and Cu coupons after exposure to these conditions are shown in Figure 3.19. Elemental compositions of corroded films after RH cycling are virtually identical with the samples exposed to constant RH conditions. A Cl peak is observed in all three Ag EDX spectra, which confirms the conclusion from CR that AgCl is one of corrosion products.

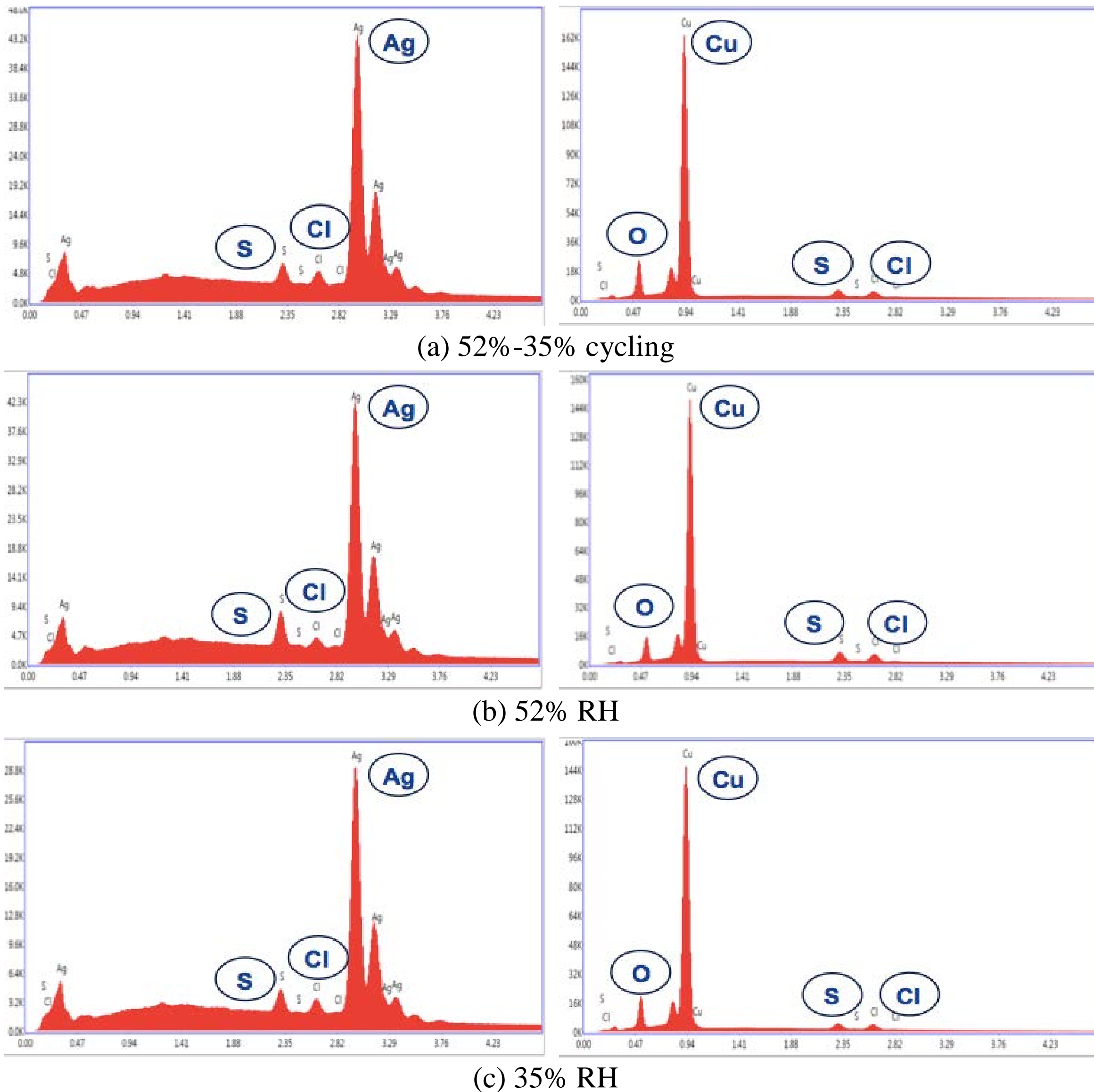

Figure 3.19 EDX spectra for Ag (left) and Cu (right) coupons after 2 days exposure in MFG chamber at (a) 52%-35% RH cycling, (b) constant 52% RH and (c) constant 35% RH.

3.6 Conclusions

In this chapter, corrosion behavior of Ag and Cu coupons under different test conditions are studied in the MFG chamber. A method to continuously monitor Cl_2 concentration in the MFG chamber is first investigated by controlling the RH of the sample gases in the Cl_2 gas detector. It provides Cl_2 monitoring method for the next round-robin testing in the IPC committee. Effects of different parameters on accelerated Ag and Cu corrosion in the MFG chamber are then studied by using a combination of analytical techniques: weight gain, SEM/EDX and cathodic reduction. The results are summarized as below:

- The synergistic effect of Cl_2 and NO_2 with H_2S have been found to accelerate Ag corrosion. Cu corrosion, however, is determined by the H_2S concentration and relatively insensitive to Cl_2 and NO_2 concentrations.
- Higher RH condition shows slightly stronger acceleration for the Cu corrosion rate compared with Ag.
- Corrosion rates of Ag and Cu coupons do not have significant differences between 30°C and 40°C. Maintaining MFG chamber temperature at 30°C makes Cl_2 measurement less challenging.

This work enables a better understanding of Ag and Cu corrosion in the MFG test, which will also contribute to the establishment of new MFG test conditions to predict ImAg surface finishes performance in more aggressive environments.

RH cycling effect on Ag and Cu corrosion is also investigated in the MFG chamber. In all three cycling ranges studied, RH cycling do not increase the corrosion rate compared with constant RH conditions. Based on CR results, the main corrosion

products for Cu and Ag are not changed under RH cycling compared to constant RH. For Ag, the dominant product is Ag_2S and for Cu, copper oxides and Cu_2S are the main corrosion products. SEM also shows no significant surface morphology change between cycling and constant RH conditions. The corrosion rate and mechanism on both Ag and Cu coupons are mostly determined by the level of the RH, rather than the cycling of the RH. The ISA 71.04 statement with respect to RH cycling therefore has been demonstrated to be incorrect. This work also provides guidance for developing more efficient and economical indoor environmental control systems.

Two papers have been published for this work:

- B.Yuan, D.A.Flemming, H.Rubin, R.Popowich, R.L.Opila and C.Xu; "Effects of Cl_2, NO_2, RH and temperature on accelerated Ag and Cu corrosion in mixed flowing gas chamber" *SMTA International Proceedings*, 385-392, Rosemont, IL, 2017
- B.Yuan, D.A.Fleming, J.Franey, R.L.Opila and C.Xu; "RH cycling effect on Ag and Cu corrosion in mixed flowing gas chamber" *ECS transaction*, 77(11), 767-775, 2017

3.7 Acknowledgement

I would like to thank Marc Benowitz and Sherwin Kahn in Nokia Bell Labs for their management support to this work.

Chapter 4

ETCHING PERFORMANCE: ATOMIC LAYER ETCHING OF IRON AND COBALT IN MAGNETIC TUNNEL JUNCTION

4.1 Introduction

4.1.1 Magnetic Random Access Memory (MRAM)

Computer memory has been defined as computer hardware devices used to store information [81]. It can be divided into two categories: volatile memory (VM) and non-volatile memory (NVM). For VM devices, the stored information will be lost if the power is off or interrupted. Dynamic random access memory (DRAM) and static random access memory (SRAM) are the two most commonly used volatile memories. As for NVM, the stored data can be maintained even if the power is interrupted. One of the most important NVM devices is flash memory.

All the aforementioned memories have been commercialized, however each of them has its own advantages and disadvantages. The read/write speed of SRAM is much faster than DRAM and flash, however, it is more expensive than DRAM and is volatile compared with flash memory. The flash can save data when power is off whereas its speed is relatively slow and can consume lots of power. All of these memories are based on the charge-storage mechanism, which provides challenges when the scale goes below 10nm where loss of stored charge might happen [82].

Emerging memories therefore have gained increasing interest from electronic industry. There are several promising candidates: magnetic random access memory (MRAM) [83], phase change memory (PCM) [84] and resistive random access memory (RRAM) [85]. Among them, MRAM has been considered as a potential universal

memory solution due to its unique combination of properties including nonvolatility, fast writing speed and high writing endurance [83]. Magnetic tunnel junction (MTJ) is the key memory element in MRAM, which consists of two ferromagnetic thin film layers separated by a tunnel barrier. The tunnel barrier is the insulating layer between the magnetic layers and MgO is one of the most commonly used materials.

Unlike conventional memory technology, data in MRAM is stored as magnetic orientation rather than charge. The magnetic moment in the bottom layer (reference layer) of MTJ is fixed while the top layer (free layer) can be changed by the applied current. If the magnetic orientations of these two layers are parallel (see Figure 4.1 (a)), the data is stored as “0” and the MTJ is in a low resistance state. If the magnetic orientations are antiparallel (see Figure 4.1 (b)), the data is stored as “1” and the MTJ is in a high resistance state. This phenomenon is also known as tunnel magnetoresistance (TMR). When the magnetic orientations are parallel, the electrons are more likely to tunnel through the tunnel barrier compared with the antiparallel condition. Therefore, different resistance states can be observed. The relative resistance change can be demonstrated as [86]:

$$TMR = \frac{R_{ap} - R_p}{R_p} \tag{4.1}$$

where R_{ap} is the resistance under antiparallel condition, R_p is the resistance under parallel condition.

Large resistance change is favored in the MRAM devices since it indicates that difference of memory states is easier to be sensed therefore the current and power consumption can be decreased [87].

(a) (b)

Figure 4.1 Simplified schematic of magnetic tunnel junction element at two distinct resistance states.

A practical MTJ is often more complicated with the reference and free layers consist of few ferromagnetic layers instead of just one single layer. Depending on the actual applications, the compositions of MTJ stack might be different. As mentioned, MgO is often used as the tunnel barrier due to the high TMR it can achieve. CoFeB and CoPt have been widely used as materials of interest in the ferromagnetic layers. To date, high-density MRAM devices have not been commercialized yet and a key limiting factor is the poor device scalability compared with the existing memory technologies.

4.1.2 Magnetic Tunnel Junction (MTJ) Patterning

To scale semiconductor devices, ultra-thin film, shrinking feature sizes and high aspect ratio of patterns are required. Such miniaturization needs advanced fabrication processes including film deposition and etching. In the MTJ stack, metal alloys such as CoFeB or CoPt are often sputter deposited on the substrate with only a few angstroms thick. In order to achieve high-density MRAM devices, etching of MTJ stack is also critically important. However, these metal materials are known not to form volatile species in the conventional Si-based etch conditions. Extensive efforts from industry and

academia are spent in the past to find a solution to MTJ patterning. A brief review will be given as follow.

Ion beam etching (IBE) is widely implemented to etch magnetic layers [88]. Argon is the most commonly used gas because it needs relative low ionization energy and is chemically inert. The Ar^+ can be accelerated by the electric field and gain enough energy to knock off the atoms on the surface of the substrate. This is a pure physical etching method with no chemistry involved. However, such bombardment will likely induce sidewall redeposition especially on the tunnel barrier, which leads to electrical shorts between the top and bottom magnetic layers. Therefore, wafer tilt and stage rotation are usually utilized in this technique [89]. In order to expand IBE technique to 300mm wafer application, the radius of beam source has to be enlarged which adds the difficulty to control beam divergence [89].

Reactive ion etching (RIE) has then been considered as an alternative method to pattern MTJ stack. Thanks to its use of chemically reactive ions, it involves both physical and chemical etching. There are two categories of RIE chemistry in metal etching application: 1) Halogen-based gas mixtures; 2) Organic-based gas mixtures.

For halogen-based chemistry, different gas mixtures were reported such as $Cl_2/O_2/Ar$ [90], HBr/Ar [91], BCl_3/Ar [92] etc. The metal halides are expected to form, however, these processes often require relatively high temperatures to volatize the metal halides due to their low volatility. Elevated temperature will have detrimental effect on thermal stability of MTJ stack. MTJ materials can be degraded at temperatures above 250°C [93]. Moreover, the introduction of halogens into the system will likely induce

corrosion issue on the magnetic layers or even on the chamber components. Post-etch treatment is usually needed to eliminate the halogen-based residues [94].

Therefore, there is a necessity to develop non-corrosive gas mixtures such as organic compounds to etch MTJ. It is also believed that metal organic complexes will have higher vapor pressures compared with metal halides. Gas mixtures such as CH_3COOH/Ar [95], CO/NH_3 [96] CH_3OH/Ar [97] have been reported. However, under certain plasma conditions, undesired hydrocarbon layers might redeposit on the metal film. RF power, chamber pressure and gas flow have to be tuned to find the optimum process condition. Unsatisfactory slanted profile and surface damage were also found under organic-based plasma condition [98].

In summary, traditional chemical assisted ion etching is not practical at this point for MTJ patterning mainly because of the low volatility of etching product, possible corrosion on metal layers after exposure to halogen chemistry and undesired hydrocarbon layer under organic-based plasma. A more controllable method is needed to etch MTJ stack with a desired profile.

4.1.3 Atomic Layer Etching (ALE)

Following the prediction of Moore's law, semiconductor industry is observing exponential growth of transistors in one integrated circuit (IC). In manufacturing, it means that more rigid requirements on process precision are needed. Now that the technology node is going below 10nm, atomic layer fidelity is undoubtedly mandatory [99].

The most successful atomic layer fabrication process is atomic layer deposition (ALD), which was introduced in 1977 [100]. It turns out to be an indispensable technique

to deposit a variety of materials with exceptional precision in the semiconductor devices [101][102][103]. Compared with traditional continuous deposition process, ALD consists of sequential, self-limiting reactions, which only take place on the available surface sites. This enables the creation of conformal nanostructures with atomic scale control.

Etching is as important as deposition in achieving next generation technology nodes. Atomic layer etching (ALE), a counterpart of ALD, is expected to remove the material one atomic layer each etching cycle using vapor-phase sequential, self-limiting reactions. In a typical ALE cycle (see Figure 4.2), there are two steps involved. In the first step, precursor A is dosed to react with a monolayer of the to-be-etched substrate to form a reactive surface. Then the pump and purge process is used to evacuate the excessive precursor A. In the second step, precursor B can react with the reactive surface from the first step to form volatile species. These volatile products then can be pumped out from the chamber and it concludes one cycle of ALE process. The substrate will recover to the original surface termination. Both of the steps can be pure thermal-driven reactions with sample heating or plasma-enhanced reactions. In some applications, the second step involves only low energy plasma bombardment instead of chemical reaction. More details and examples will be given later. In the ALE cycle, both or at least one of the steps need to be self-limiting to achieve atomic layer control.

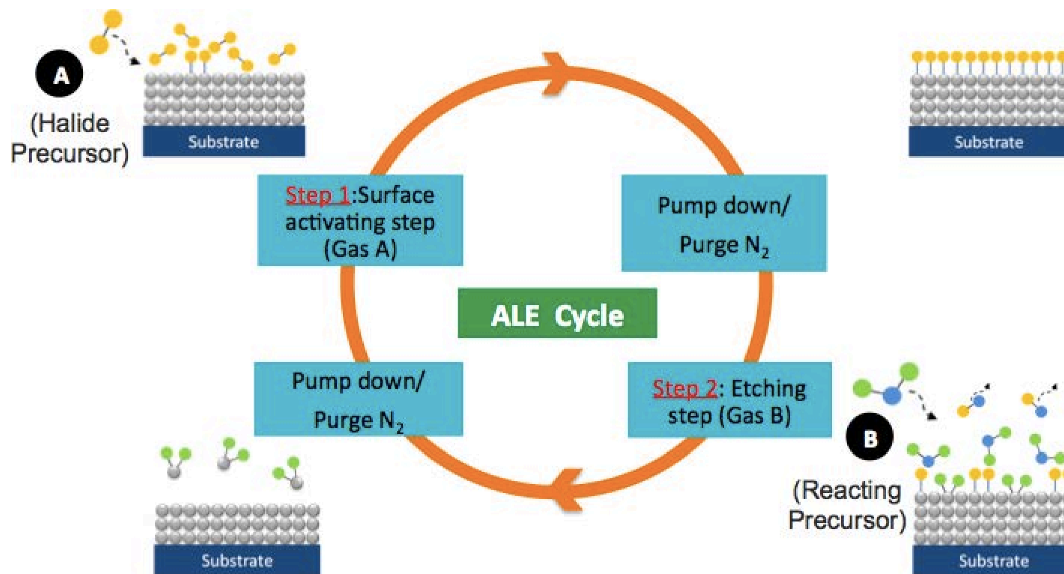

Figure 4.2 Process flow of one ALE cycle.

Even though ALE is not as fully investigated as ALD, there are some literatures reporting the ALE process on various substrates [99][104]. Si is probably the most extensively studied material [104][105][106], where combination of Cl_2 and Argon has been used in the process. The first step is the chlorination step and in the second step, Argon plasma is used to remove the top chlorinated surface rather than the bulk Si. Since chlorine is electronegative, it can weaken the Si-Si bonding energy underneath the SiCl layer so that the top layer is easier to be removed. To achieve ALE of Si, the threshold energy for desorption step needs to be found to remove the top silicon layer while keep the second silicon layer intact. A similar method has been applied for etching of GaAs [107], HfO_2 [108], ZrO_2 [109] etc. Halogen is usually used in the activation step, which is followed by the removal step using low energy plasma (typically Ar^+). The ion energy in the second step has to be carefully controlled so that there will be no sputtering or surface damage during the process.

In order to resolve the possible problems from plasma-driven step, thermal (no plasma) ALE process has gained increasing interest. In the thermal ALE, both activation and desorption steps involve pure chemical reactions. Thermal ALEs of Al_2O_3 [110], HfO_2 [111], ZnO [112] have been extensively reported by Dr. Steven George's group using ligand-exchange reactions. The first step usually contains fluorination or chlorination reaction to activate the surface, and in the second step, a co-reagent is used to perform ligand-exchange reactions with the activated surface to form volatile species. For instance, in Al_2O_3 ALE, HF is used in the first step to fluorinate the Al_2O_3 top layer to form AlF_3, then in the second step, $Sn(acac)_2$ (acac=acetylacetone) is used to react with AlF_3 to form volatile SnF(acac) and $Al(acac)_3$ species which can be pumped out from the system.

The choice of ligand in the removal step is directly dependent on the materials to be etched. Therefore, highly selectivity etching can be achieved in this technique. Selectivity of Al_2O_3, HfO_2 and ZrO_2 has been studied using a combination of HF and trimethylaluminum (TMA) [113]. Since the etching byproducts are volatile, there will be no redeposition on the substrate during the process.

In this work, we first apply the thermal ALE technique to etch Fe and Co films in the MTJ stack using a combination of Cl_2 and Hexafluoroacetylacetone (Hfac) as the first and second step precursor respectively. Cl_2 is a widely used chemical for surface chlorination and since its heavy usage in the electronics industry, semiconductor-grade Cl_2 has fairly easy access. Metal β-diketonates have been reported to have very high vapor pressure and are commonly used as precursors in metal chemical vapor deposition [114][115]. There are three common β-diketonates: acetylacetone (Acac),

trifluoroacetylacetone (Tfac) and Hexafluoroacetylacetone (Hfac). It is reported that the two CF_3 ligands in the Hfac enhance its volatility compared with other two compounds and therefore it is used in our application. Since the etching chemistry is critical for ligand exchange reaction, pure metal samples such as Fe and Co are used instead of metal alloys to eliminate any possible synergistic effects in the alloys.

4.2 Experimental Methods

4.2.1 Etching Chamber Setup

The ALE experiments are conducted in a homemade etching system, which is designed for both plasma and thermal ALE process (see Figure 4.3). The reactor is a stainless-steel spherical chamber that has been modified for gas delivery, vacuum pumping, stage heating and electrical connections. A mechanical pump (Edwards, E2M30) provides the vacuum in the reactor. A butterfly valve is used before the mechanical pump to control the pressure of the reactor. The base pressure of the system is 40 mtorr when the butterfly valve is fully open and no gas is flowing into the chamber. A mass spectrometer is used to analyze the purity of precursors and compositions of etching byproducts. In the gas delivery system, there are six gas lines and the gas dose is precisely controlled by the mass flow controller (1179A, MKS) through LabVIEW. Since Hfac is a liquid precursor under room temperature, it is stored in a stainless-steel bubbler followed by a needle valve before introduction to the chamber. The needle valve is used to control the partial pressure of Hfac. A nitrogen glove box is used during the transportation of liquid Hfac to the bubbler. The freeze-pump-thaw cycles are performed to remove nitrogen from the transfer process before Hfac is used in the experiments.

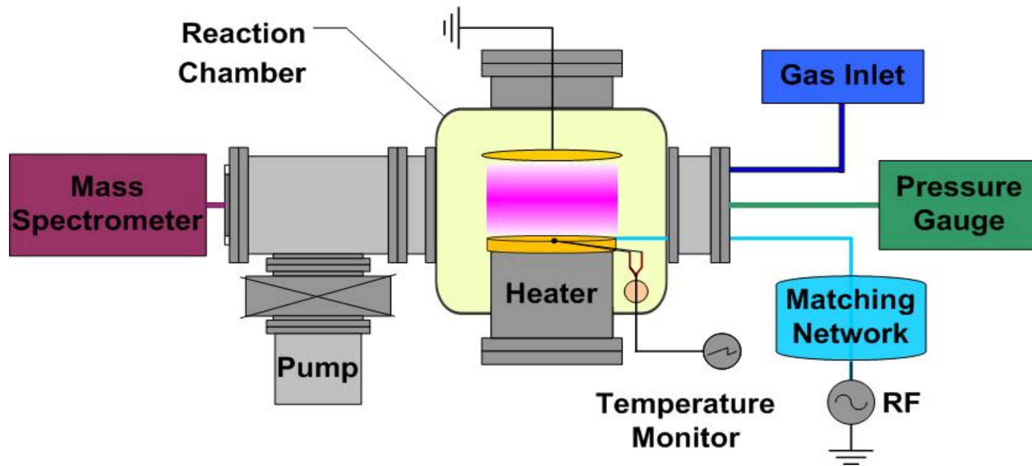

Figure 4.3 Schematic of the ALE tool setup.

The tool is initially designed for plasma ALE and a capacitively-coupled plasma (CCP) design is adopted in the system. Essentially, it consists of two parallel metal electrodes. The bottom electrode (4” diameter aluminum disc) is connected to 13.56 MHz RF power supply through an electrical feed-through at the top flange, and the top electrode is grounded. A temperature controllable heater is installed underneath the bottom electrode to escalate temperature. A ceramic plate (thickness 1/8”) made of boron nitride (BN) is used to make thermal contact between the bottom electrode and the heating block. The BN layer is an excellent electrical insulator and the ceramic size is 4.5” diameter to prevent any risk of arcing between the powered RF electrode and the grounded heating block. The heating block can reach 425°C. In order to minimize the reflected power back from plasma discharge into the RF cables, and maximize the RF power transferred from the RF generator into the plasma discharge, an ATX 600 AE Advanced Energy RF Matching Network (L type) is used for impedance matching. The plasma is generated and sustained by the RF power in the small gap (between the two electrodes) filled with low pressure gases (typically less than 1 torr).

During thermal ALE, the RF power is turned off and there is no plasma in the process therefore the only energy source to initiate the reaction is escalated temperature.

4.2.2 Etching Chamber Validation

4.2.2.1 Temperature Calibration

It is critical to determine the real reaction temperature on the sample surface during thermal ALE. The surface temperature calibration is conducted by placing a 4” Si wafer on the top of stage and the temperatures of five different plots on the wafer are measured using K type thermocouples (see Figure 4.4).

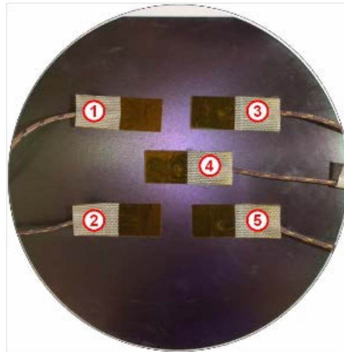

Figure 4.4 Five thermocouples placed on Si wafer surface for temperature calibration.

During the calibration experiments, a 60 sccm of Ar gas flow and 0.6 torr of chamber pressure are set to approach the actual conditions in the thermal ALE experiments. A range of temperatures from 50°C to 425°C are tested. Figure 4.5 illustrates the set temperature of the heater versus the measured temperature on the wafer. We can see that temperatures measured from five thermocouples are almost overlapped together, which indicates good temperature uniformity on the sample surface. This plot also shows almost linear relationship between heater setting temperature and measured

temperature. The temperatures mentioned in the following ALE experiments are calibrated temperatures using this plot.

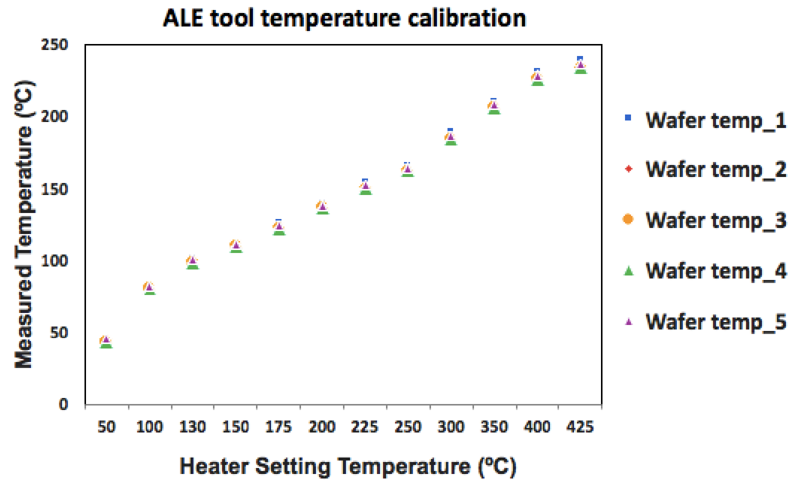

Figure 4.5 ALE tool temperature calibration plot.

4.2.2.2 SiO_2 Etching Rate

In addition to the temperature calibration, chamber uniformity is also tested by mapping the SiO_2 etching rate on the stage. There are twelve 1 inch by 1 inch SiO_2 coupons placed on the sample stage (Figure 4.6 (a)). The thicknesses of these coupons before and after etching are measured by a JA Woollam spectroscopic ellipsometer (SE). Plasma etching conditions are shown in Figure 4.6 (b). The reason why SiO_2 samples are utilized rather than metal coupons is that metal sample thickness is difficult to be measured by ellipsometry due to its absorption of the light from the beam, whereas dielectric thickness measurement by SE is fairly easy. Figure 4.7 demonstrates the etching rates of twelve coupons. Coupon numbers are written in the bottom of the bars. We can see that when comparing the coupons on the same column (column 1 or 2), the etching rate uniformity is excellent. However, there is a trend of etching rate when

comparing coupons on the same line (line 1 or 2). The etching rate of coupon close to gas introduction side is slower than the coupon close to the pumping side. This is likely due to the distribution of gas concentration in the chamber. Therefore, in the following ALE experiments, coupons are placed vertically to the gas flow direction to ensure etching rate uniformity.

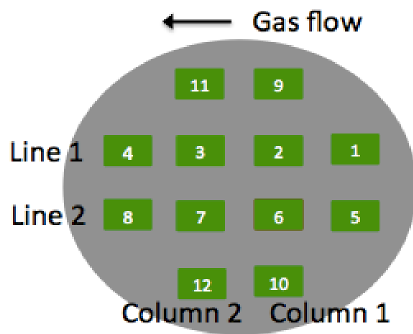

(a)

Wafer temperature	150C
RF power	200 W
Pressure	0.6 torr
Time	600 seconds
Ar	30 sccm
CF_4	20 sccm

(b)

Figure 4.6 (a) SiO_2 coupons map on the sample stage. Gas flow is from right to the left. (b) Etching conditions for SiO_2.

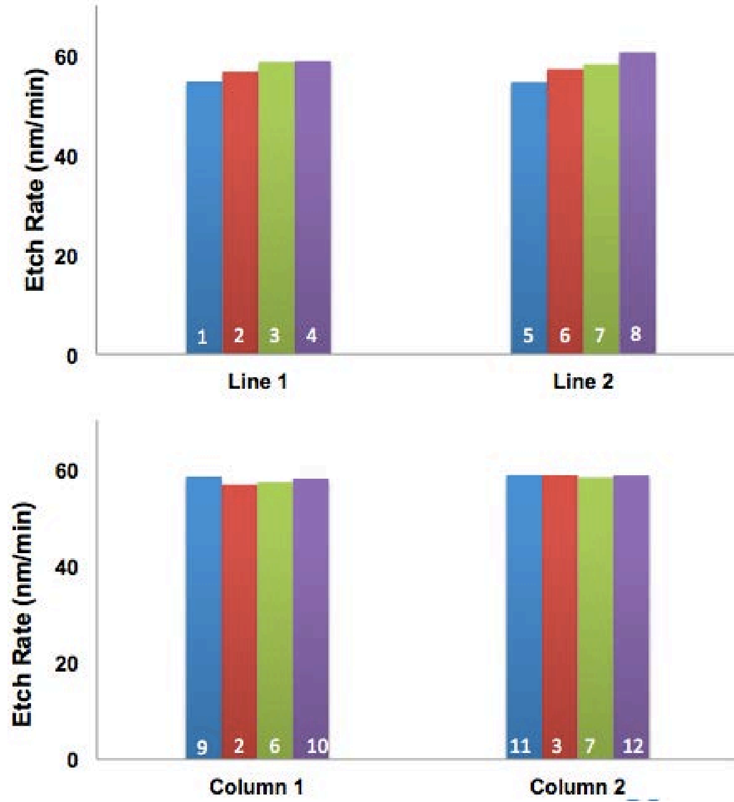

Figure 4.7 Etching rates of SiO_2 coupons at different locations on the stage.

4.2.3 Sample and Materials Information

The sizes of tested Fe and Co coupons are 1 inch (width) × 1 inch (length), cut from a 300mm commercial wafer (Advantiv). There are two types of metal samples: one with 50nm Fe or Co film on the top of 10nm Ti; another has 300nm Fe or Co film on top of 50nm Ta and 500nm thermal SiO_x (see Figure 4.8). Ti and Ta are common adhesion layers for the growth of metal. The 50nm metal samples are used for EDX measurements for obtaining atomic ratio information and the 300nm metal samples are used for cross sectional SEM to calculate film thickness. Figure 4.9 shows an EDX spectrum of a 50nm pristine Co sample and cross-sectional SEM of a 300nm Co film.

Lecture bottle cylinder is used as the Cl_2 (98% purity) source. Hexafluoroacetylacetone (Hfac, 98% purity) is purchased from Sigma Aldrich. Figure 4.10 shows the structure of Hfac.

(a) (b)

Figure 4.8 Cross-section of two types of metal samples.

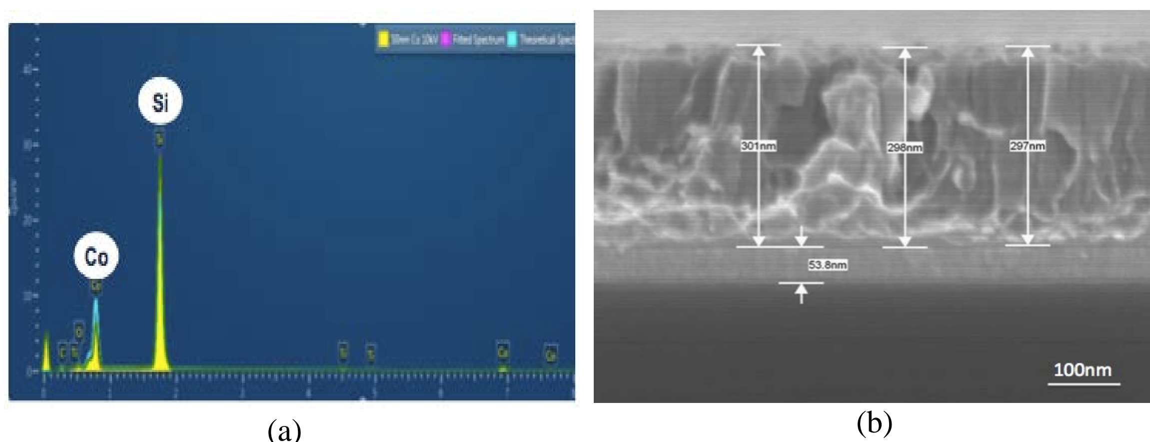

(a) (b)

Figure 4.9 (a) EDX (10kV) spectrum of a 50nm Co sample. (b) Cross-sectional SEM of a 300nm Co film.

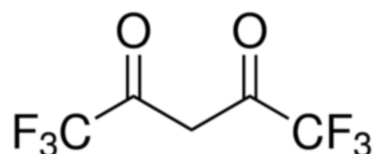

Figure 4.10 Structure of Hexafluoroacetylacetone.

4.3 Results and Discussion

4.3.1 Self-limiting Behavior of ALE Process

An ideal ALE process is based on self-limiting reactions, which means the reactants can only react with the available surface sites on the substrate while keep the bottom layer intact. Therefore, the self-limiting nature regarding the reactant dose and exposure time for both Cl_2 and Hfac steps are first investigated. Table 4.1 presents the etching conditions and the corresponding figures. X indicates the changing parameter in that condition. All the experiments are conducted under 170°C and 15 ALE cycles are performed to ensure enough amount of metal is etched away. A constant purge of N_2 is used at the end of each step to eliminate the excessive precursor from the system. For Figure 4.11 (a), it examines the M/Ti ratio (M = Fe or Co) versus the Cl_2 exposure time. The atomic ratio of Fe, Co and Ti are measured from EDX spectra. M/Ti ratio provides a good indication of the trend of metal etching rate. We can see that with increasing Cl_2 exposure time, the Co or Fe signal in the EDX spectra deceases, which means a decrease of the metal film thickness. M/Ti starts leveling off after 20s Cl_2 exposure, which suggests that this reaction might start reaching surface saturation. With the same logic, Cl_2 flow rate, Hfac exposure time and Hfac partial pressure have all been investigated regarding their self-limiting behavior (see Figure 4.11, Figure 4.12).

Table 4.1 Etching conditions for examining self-limiting behavior of Cl_2 and Hfac reactions in Fe and Co ALE when T = 170°C.

	Step 1			**Step 2**		
Figure #	Ar	Cl_2	Time	Ar	Hfac	Time
4.11 (a)	60 sccm	15 sccm	X	60 sccm	30 mtorr	45s
4.11 (b)	60 sccm	X	20s	60 sccm	30 mtorr	45s
4.12 (a)	60 sccm	15 sccm	20s	60 sccm	30 mtorr	X
4.12 (b)	60 sccm	15 sccm	20s	60 sccm	X	45s

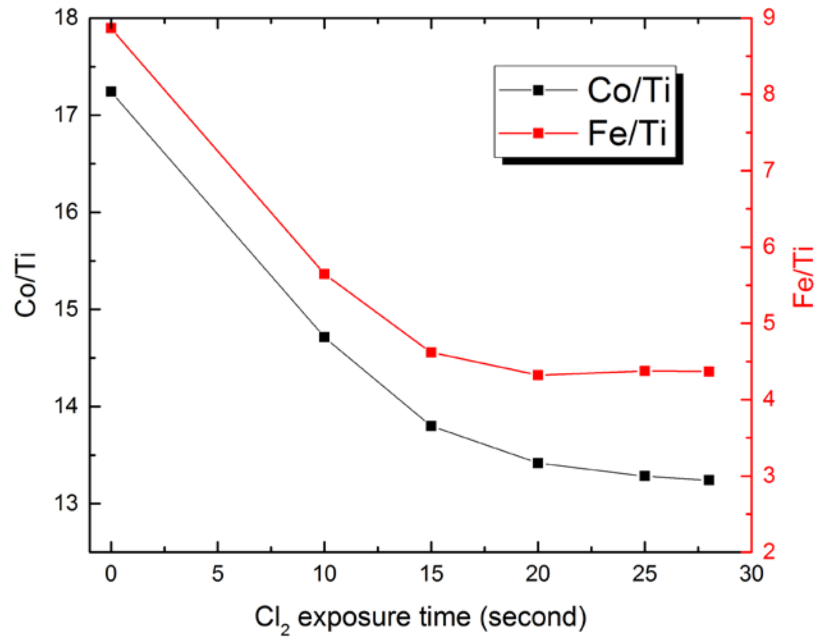

(a)

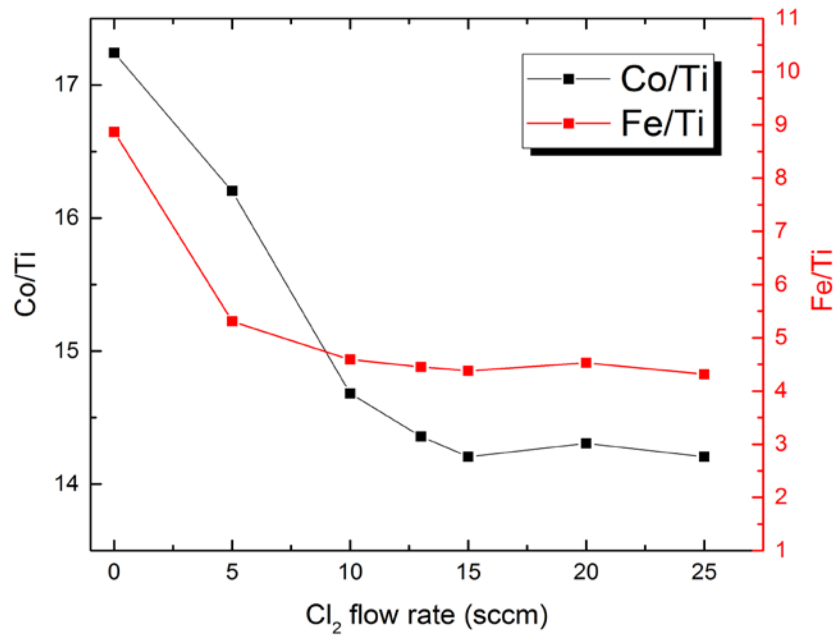

(b)

Figure 4.11 Self-limiting plots for Cl_2 reaction in the Fe and Co ALE. (a) M/Ti ratio versus Cl_2 exposure time; (b) M/Ti ratio versus Cl_2 flow rate. Temperature is at 170°C.

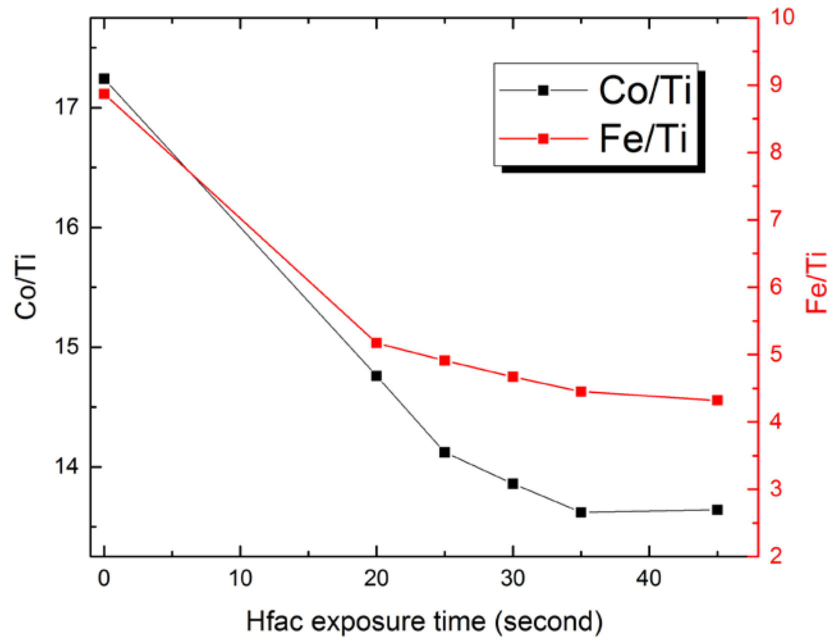

(a)

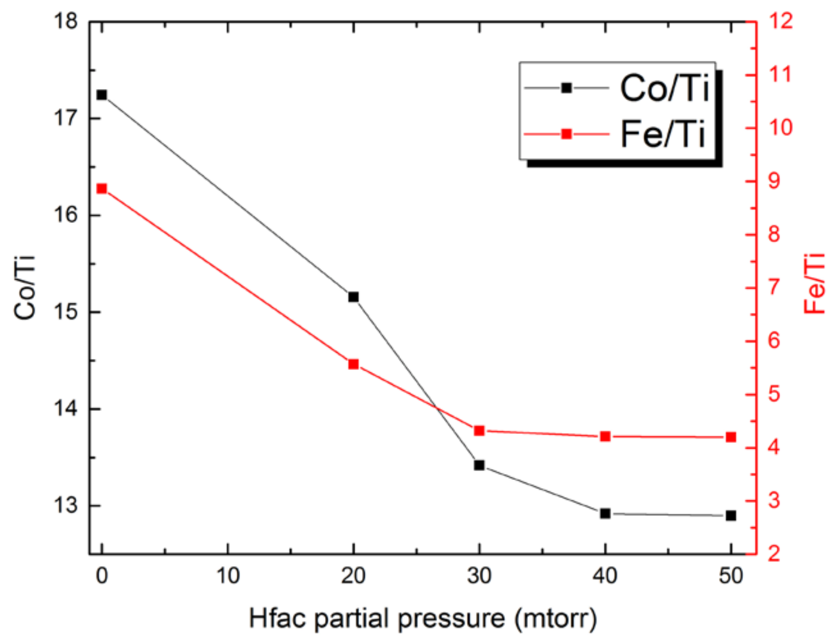

(b)

Figure 4.12 Self-limiting plots for Hfac reaction in the Fe and Co ALE. (a) M/Ti ratio versus Hfac exposure time; (b) M/Ti ratio versus Hfac partial pressure. Temperature is at 170°C.

4.3.2 Thermal Etching Rates of Fe and Co

After examining the self-limiting behavior of Cl_2 and Hfac reactions in the ALE process, optimized process parameters at 170°C are shown in Table 4.2. Fe and Co etching behavior based on these parameters under different temperatures are studied. Cross-sectional SEM is used to measure the film thickness before and after etching. Thicknesses at multiple spots in one sample are measured and error bars are calculated. Figure 4.13 (a) shows the etching behavior of Co under 140°C, 155°C, 170°C and 185°C. We can see that under each temperature, Co is etched linearly using sequential reactions of Cl_2 and Hfac. A proposed mechanism is shown in the following equation (4.2) and (4.3). The final product $M(hfac)_x$ is considered as volatile species that can be pumped out from the chamber. Under 140°C, the etching rate is 0.2nm/cycle which indicates the atomic scale etching control. Figure 4.13 (b) presents the dependency of etching rates on different temperatures. The etching rate ranges from 0.2 nm/cycle at 140°C to 1.6nm/cycle at 185°C. The etching rate trend with temperature seems to be approximately linear except the data point at 155°C. This discrepancy might due to the fact that all etching parameters for self-limiting are optimized under 170°C. Therefore, experiments are needed to validate the self-limiting behavior under other temperature conditions. Step 2 only experiments are also conducted at 170°C, and it shows no change of metal thickness after etching under this condition. It suggests that Co can not directly react with Hfac to form volatile species and sequential reaction with both Cl_2 and Hfac is needed to achieve ALE of Co.

Thermal ALE of Fe is also studied under the above four temperatures (see Figure 4.14 (a)). Linear etching of Fe is observed at each temperature, which validates the precise control advantage of ALE. The etching rate ranges from 0.3 nm/cycle at 140°C to 1.2 nm/cycle at 185°C. As mentioned, self-limiting behavior under different temperatures needs to be investigated to fully understand the relationship between etching rate and temperature. Also, since ALE is a two-step process, understanding of temperature dependence of each step is necessary.

Table 4.2 Optimized ALE conditions for Fe and Co

Step 1			**Step 2**		
Ar	Cl_2	Time	Ar	Hfac	Time
60 sccm	15 sccm	20s	60 sccm	30 mtorr	45s

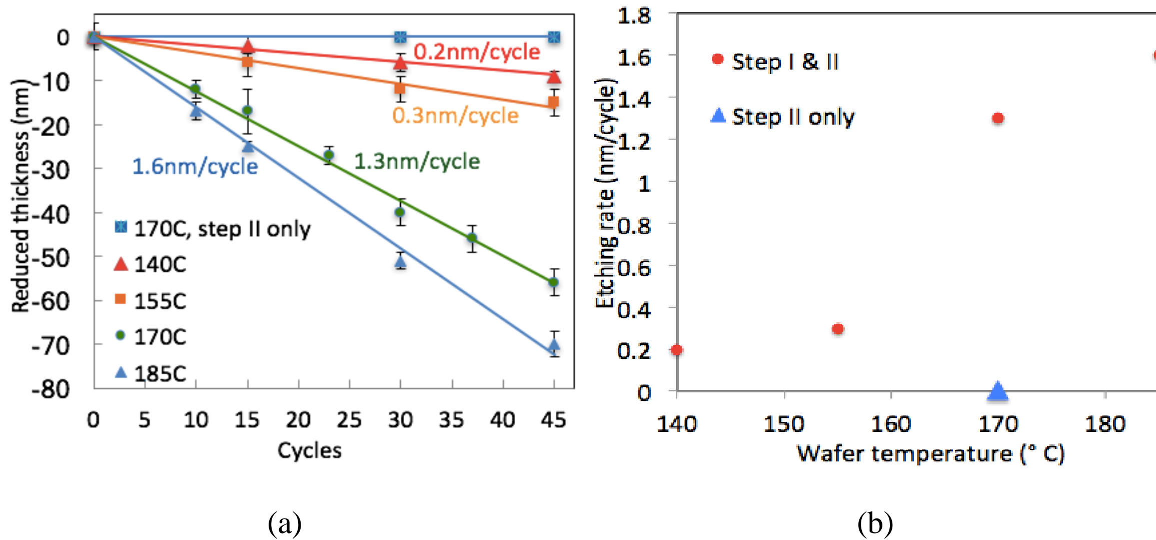

(a) (b)

Figure 4.13 (a) Reduced thickness of Co under different temperatures and ALE cycles. (b) Etching rate of Co as a function of temperature.

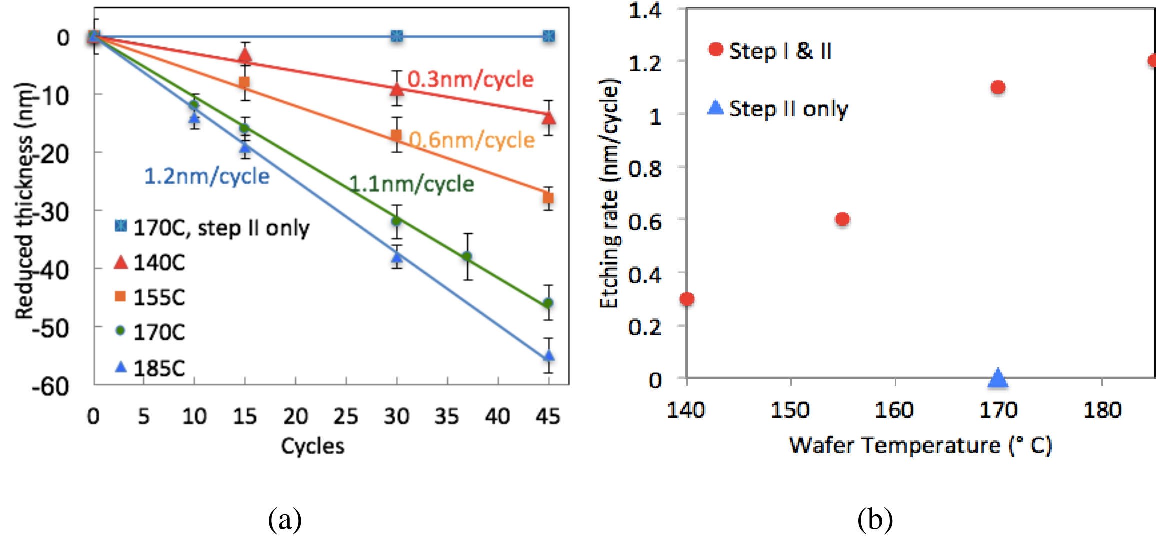

(a) (b)

Figure 4.14 (a) Reduced thickness of Fe under different temperatures and ALE cycles. (b) Etching rate of Fe as a function of temperature.

4.3.3 AFM of Pristine and Etched Co Samples

AFM is used to compare surface roughness of the pristine and etched Co samples to see if the ALE process changes the surface morphology. Figure 4.15 shows AFM images for pristine Co sample and etched Co sample after 45 ALE cycles at 140°C. We can see that there is no obvious surface morphology change between the two samples. The root mean square (RMS) of roughness for pristine Co is 4.8nm and etched Co sample is 6.5nm. Table 4.3 demonstrates the RMS measured by AFM for selected Co samples. We can see that ALE process does not substantially increase the surface roughness compared with the pristine sample, which is a good indication that ALE leads to conformal etching.

Table 4.3 RMS measured by AFM for selected Co samples

	Pristine Co	140°C, 15cycles Co	140°C, 45cycles Co	155°C, 15cycles Co	185°C, 15cycles Co
RMS (nm)	4.8	6.6	6.5	5.8	6

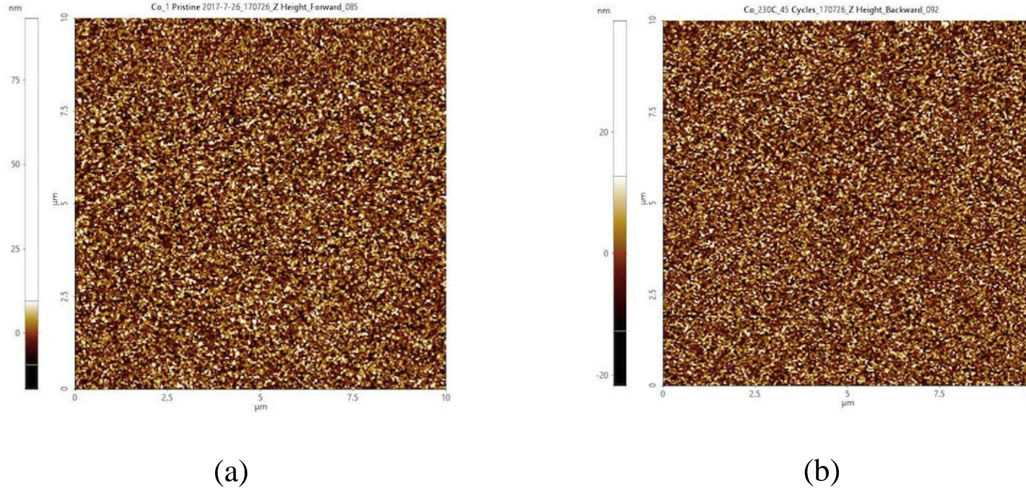

(a) (b)

Figure 4.15 AFM images for (a) pristine Co and (b) etched Co under 140°C after 45 ALE cycles.

4.4 Conclusions

Sequential, self-limiting thermal reactions of Cl_2 and Hfac can etch Fe and Co with atomic layer control. The proposed etching mechanism is that Fe or Co can react with Cl_2 in the first step to form metal chloride, then, the metal chloride can react with Hfac to form $M(hfac)_x$ complexes, which are highly volatile and can be pumped out from the chamber. A range of temperatures from 140°C to 185°C is investigated. The Co etching rate ranges from 0.2 nm/cycle at 140°C to 1.6 nm/cycle at 185°C. The Fe etching rate can range from 0.3 nm/cycle at 140°C to 1.2 nm/cycle at 185°C. As shown, there is a relationship between the metal etching rate with reaction temperature. However, since all etching conditions for self-limiting are optimized under 170°C, validation experiments are needed to confirm the surface saturation under other temperature conditions. This includes parts of the future work to understand the dependency of Cl_2 and Hfac reaction rates on different temperatures respectively. AFM results show no obvious surface roughness change after the ALE process, which confirms its inherent advantage of

conformal etching. Future work in this project will be focusing on using in-situ XPS to understand the etching mechanism and applying this ALE technique to pattern the real MTJ stack in MRAM devices.

4.5 Acknowledgement

I would like to thank the funding support from the National Science Foundation and American Air Liquide Delaware Research and Technology Center (DRTC).

Chapter 5

SUMMARY AND FUTURE WORK

In this dissertation, I sought to improve the performances of electronic devices upon the points that were not previously understood. Three different aspects are considered: optical, reliability, and etching performance. In this chapter, the conclusions and future work of these topics is summarized. Final remarks is also made.

5.1 Optical Performance

III-V tandem solar cells on Si substrate have been widely investigated due to unique integration of high efficiency III-V solar cells and low-cost Si substrate. Ta_2O_5 moth-eye anti-reflection coatings (ARCs) are first fabricated on dual junction GaAsP/SiGe solar cells on Si substrate to minimize surface reflection of the device. Deep UV lithography and reactive ion etching are utilized in the fabrication processes. The optical performance of such moth-eye nanostructures is also optically modeled by using finite difference time domain (FDTD) method. The optimized moth-eye ARCs can achieve solar cells reflection as low as 2.2% from 400-1100 nm at an incident angle of 8°. This result outperforms the optimized traditional double layer antireflection coatings (DLARCs).

Future work in this part will focus on testing anti-reflective performances of moth-eye structures at different incident angles and evaluating tandem solar cells efficiency by patterning Ta_2O_5 moth-eye ARCs.

5.2 Reliability Performance

Since corrosion is a growing concern in the electronic industry, accelerated laboratory testing is developed to understand equipment reliability in a compressed time. We use mixed flowing gas (MFG) chamber to study effects of Cl_2, NO_2, relative humidity (RH) and temperature on accelerated Ag and Cu corrosion. A combination of analytical techniques: weight gain, SEM/EDX and cathodic reduction is utilized to study the corrosion behavior of Ag and Cu. Ag is sensitive to Cl_2 and NO_2 concentrations whereas Cu is not. This work enables a better understanding of Ag and Cu corrosion in the MFG test, which will contribute to the establishment of new MFG test conditions to predict ImAg surface finishes performance in more aggressive environments.

RH cycling effect on Ag and Cu corrosion is also investigated in the MFG chamber. Three different cycling ranges are studied in this work and RH cycling has been approved not to increase the corrosion rate compared with constant RH conditions. Based on the cathodic reduction results, the main corrosion products for Cu and Ag are not changed under RH cycling compared to constant RH. The corrosion rate and mechanism on both Ag and Cu coupons are mostly determined by the level of the RH, rather than the cycling of the RH. This work provides guidance for developing more efficient and economical indoor environmental control systems.

5.3 Etching Performance

Magnetic tunneling junction (MTJ) patterning is a critical factor to achieve high-density magnetic random access memory (MRAM). Fe and Co are the most common materials used in the MTJ stack. In this work, sequential, self-limiting thermal reactions of Cl_2 and Hfac are used to etch Fe and Co with atomic layer control. A range of process

temperatures from 140°C to 185°C is investigated. The etching rate of Fe and Co can be achieved as low as 0.3nm/cycle and 0.2nm/cycle at 140°C respectively. AFM results show no obvious surface roughness change on Co sample after the atomic layer etching (ALE) process, which confirms its inherent advantage of conformal etching.

Future work will consist of two parts. The first part will be focusing on applying this ALE process to pattern the real MTJ stack and evaluating its selectivity over different materials in the MTJ. The second part is to understand etching mechanism using in-situ XPS. An in-situ XPS system has been designed and built. Figure 5.1 shows the schematic of in-situ XPS system.

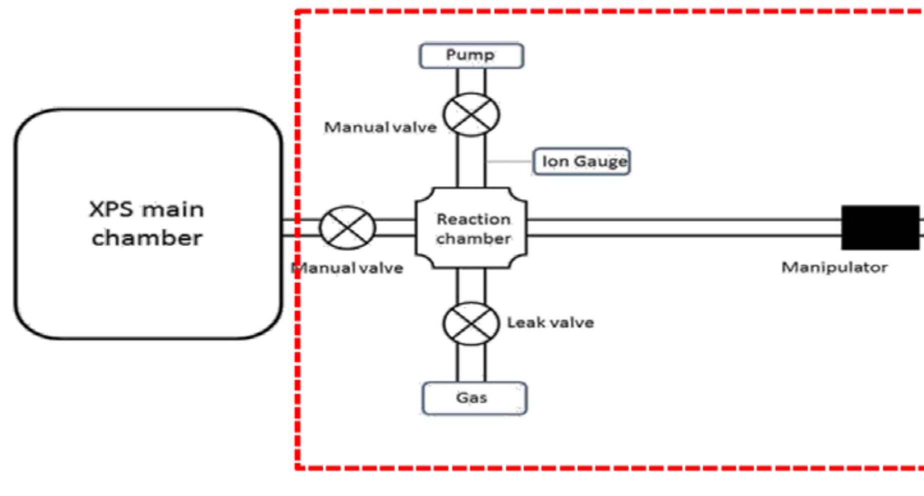

Figure 5.1 Schematic of in-situ XPS system.

A reaction chamber is attached to the XPS main chamber and separated by a manual valve. Cl_2 and Hfac will be dosed to the reaction chamber through a leak valve and a needle valve respectively. A heater is placed underneath the sample stage for sample heating. The manipulator is used to transfer the sample from reaction chamber to the XPS main chamber without exposure of the sample to the atmosphere. The base

pressure of the reaction chamber is 10^{-6} torr. There are several reasons for deploying such in-situ system to understand etching mechanism:

- The in-situ study can eliminate the possible contaminations from atmosphere (usually adventitious carbon).
- The pristine metal sample can be sputtered clean in the XPS chamber before transferring to reaction chamber to remove the possible oxide on the surface.
- The temperature dependencies of step 1 and 2 in the ALE process can be studied independently in this XPS system.

5.4 Final Remarks

Over the course of this dissertation, surface studies in different areas of the electronic industry have been discussed. All of the projects are connected by surface science and under the overarching theme that it is critically important to conduct fundamental surface chemistry research to solve real-world problems.

REFERENCES

[1] Somorjai, G. A. and Y. M. Li, "Impact of surface chemistry." *Proceedings of National Academy of Sciences* 108 no. 3 (2011): 917-924.

[2] Yates, J. T. and C. T. Campbell, "Surface chemistry: Key to control and advance myriad technologies." *Proceedings of National Academy of Sciences* 108 no. 3 (2011): 911-916.

[3] Hollander, J. M. and W. L. Jolly. "X-ray photoelectron spectroscopy." *Accounts of chemical research* 3, no. 6 (1970): 193-200.

[4] Lee, H. L. and N. T. Flynn. "X-ray photoelectron spectroscopy." *Handbook of Applied Solid State Spectroscopy* (2006): 485-507.

[5] Meyer, E. R. N. S. T. "Atomic force microscopy." *Progress in surface science* 41, no. 1 (1992): 3-49.

[6] Donnelly, V. M. and A. Kornblit. "Plasma etching: Yesterday, today, and tomorrow." *Journal of Vacuum Science & Technology A: Vacuum, Surfaces, and Films* 31, no. 5 (2013): 050825.

[7] Park, J. S., W. J. Maeng, H. S. Kim, and J. S. Park. "Review of recent developments in amorphous oxide semiconductor thin-film transistor devices." *Thin solid films* 520, no. 6 (2012): 1679-1693.

[8] Pierson, H. O. "Handbook of chemical vapor deposition: principles, technology and applications." William Andrew, 1999.

[9] Hopwood, J. "Review of inductively coupled plasmas for plasma processing." *Plasma Sources Science and Technology* 1, no. 2 (1992): 109.

[10] Watt, F., A. A. Bettiol, J. A. Van Kan, E. J. Teo, and M. B. H. Breese. "Ion beam lithography and nanofabrication: a review." *International Journal of Nanoscience* 4, no. 03 (2005): 269-286.

[11] Fraunhofer ISE: Photovoltaics Report, updated: 12 July 2017.

[12] Shockley, W., and H. J. Queisser. "Detailed balance limit of efficiency of p-n junction solar cells." *Journal of applied physics* 32, no. 3 (1961): 510-519.

[13] Kerr, M. J., A. Cuevas, and P. Campbell. "Limiting efficiency of crystalline silicon solar cells due to Coulomb-enhanced Auger recombination." *Progress in Photovoltaics: Research and Applications* 11, no. 2 (2003): 97-104.

[14] Richter, A., M. Hermle, and S. W. Glunz. “Reassessment of the limiting efficiency for crystalline silicon solar cells.” *IEEE Journal of Photovoltaics* 3, no. 4 (2013): 1184-1191.

[15] Yoshikawa, K., H. Kawasaki, W. Yoshida, T. Irie, K. Konishi, K. Nakano, T. Uto, D. Adachi, M. Kanematsu, H. Uzu and K. Yamamoto, “Silicon heterojunction solar cell with interdigitated back contacts for a photoconversion efficiency over 26%.” *Nature Energy* 2 (2017): 17032.

[16] Masuko, K., M. Shigematsu, T. Hashiguchi, D. Fujishima, M. Kai, N. Yoshimura, T. Yamaguchi, Y. Ichihashi, T. Mishima, N. Matsubara, T, Yamanishi, T. Takahama, M. Taguchi, E. Maruyama and S. Okamoto. “Achievement of more than 25% conversion efficiency with crystalline silicon heterojunction solar cell.” *IEEE Journal of Photovoltaics* 4, no. 6 (2014): 1433-1435.

[17] Green, M. A., Y. Hishikawa, W. Warta, E. D. Dunlop, D. H. Levi, J. Hohl-Ebinger, and A. W. H. Ho-Baillie. “Solar cell efficiency tables (version 50).” *Progress in Photovoltaics: Research and Applications* 25, no. 7 (2017): 668-676.

[18] Létay, G. and A. Bett. “EtaOpt–a program for calculating limiting efficiency and optimum bandgap structure for multi-bandgap solar cells and TPV cells.” in *Proceedings of 17th European Photovoltaic Solar Energy Conference*, Munich, Germany, 2001.

[19] Jackson, E. D. “Areas for improvement of the semiconductor solar energy converter.” in *Transactions of the Conference on the Use of Solar Energy*, Tucson, Arizona, 1955.

[20] Tibbits, T. ND, P. Beutel, M. Grave, C. Karcher, E. Oliva, G. Siefer, A. Wekkeli, M. Schachtner, F. Dimroth, A. W. Bett, R. Krause, M. Piccin, N. Blanc, M. Munoz-Rico, C. Arena, E. Guiot, C. Charles-Alfred, C. Drazek, F. Janin, L. Farrugia, B. Hoarau, J. Wasselin, A. Tauzin, T. Signamarcheix, T. Hannappel, K. Schwarzburg and A. Dobrich. “New efficiency frontiers with wafer-bonded multi-junction solar cells.” in *Proceedings of the 29th European Photovoltaic Solar Energy Conference and Exhibition*, Amsterdam, Netherlands, 2014

[21] Cotal, H., C. Fetzer, J. Boisvert, G. Kinsey, R. King, P. Hebert, H. Yoon, and N. Karam. “III–V multijunction solar cells for concentrating photovoltaics.” *Energy & Environmental Science* 2, no. 2 (2009): 174-192.

[22] Jain, N., and M. K. Hudait. “III–V multijunction solar cell integration with silicon: Present status, challenges and future outlook.” *Energy Harvesting and Systems* 1, no. 3-4 (2014): 121-145.

[23] Connolly, J. P., D. Mencaraglia, C. Renard, and D. Bouchier. “Designing III–V multijunction solar cells on silicon.” *Progress in Photovoltaics: Research and Applications* 22, no. 7 (2014): 810-820.

[24] Fitzgerald, E. A., Y. H. Xie, M. L. Green, D. Brasen, A. R. Kortan, J. Michel, Y. J. Mii, and B. E. Weir. "Totally relaxed Ge_xSi_{1-x} layers with low threading dislocation densities grown on Si substrates." *Applied Physics Letters* 59, no. 7 (1991): 811-813.

[25] Diaz, M., L. Wang, A. Gerger, A. Lochtefeld, C. Ebert, R. Opila, I. Perez-Wurfl, and A. Barnett. "Dual-junction GaAsP/SiGe on silicon tandem solar cells." *in Proceedings of 40th Photovoltaic Specialist Conference*, Colorado, Denver, 2014.

[26] Schmieder, K. J., A. Gerger, M. Diaz, Z. Pulwin, C. Ebert, A. Lochtefeld, R. Opila, and A. Barnett. "Analysis of tandem III–V/SiGe devices grown on Si." *in Proceedings of 38th Photovoltaic Specialists Conference*, Austin, Texas, 2012.

[27] Schmieder, K. J., A. Gerger, Z. Pulwin, L. Wang, M. Diaz, M. Curtin, C. Ebert, A. Lochtefeld, R. L. Opila, and A. Barnett. "GaInP window layers for GaAsP on SiGe/Si single and dual-junction solar cells." in *Proceedings of 39th Photovoltaic Specialists Conference*, Tampa, Florida, 2013.

[28] Brendel, R. and A. Goetzberger, "Thin-film Crystalline Silicon Solar Cells: Physics and Technology" Weinheim, Germany: Wiley-VCH 2003.

[29] NREL ASTM G173-03 "Reference Solar Spectral Irradiance: Air Mass 1.5" http://rredc.nrel.gov/solar/spectra/am1.5/

[30] Balanis, C. "Advanced Engineering Electromagnetics." John Wiley and Sons, 1989.

[31] Schubert, M. F., F. W. Mont, S. Chhajed, D. J. Poxson, J. K. Kim, and E. F. Schubert. "Design of multilayer antireflection coatings made from co-sputtered and low-refractive-index materials by genetic algorithm." *Optics express* 16, no. 8 (2008): 5290-5298.

[32] Aiken, D. J. "Antireflection coating design for series interconnected multi-junction solar cells." *Progress in photovoltaics* 8, no. 6 (2000): 563-570.

[33] Saylan, S., T. Milakovich, S. A. Hadi, A. Nayfeh, E. A. Fitzgerald, and M. S. Dahlem. "Multilayer antireflection coating design for $GaAs_{0.69}P_{0.31}$/Si dual-junction solar cells." *Solar Energy* 122 (2015): 76-86.

[34] Diedenhofen, S. L., G. Grzela, E. Haverkamp, G. Bauhuis, J. Schermer, and J. G. Rivas. "Broadband and omnidirectional anti-reflection layer for III/V multi-junction solar cells." *Solar Energy Materials and Solar Cells* 101 (2012): 308-314.

[35] Perl, E. E., W. E. McMahon, J. E. Bowers, and D. J. Friedman. "Design of antireflective nanostructures and optical coatings for next-generation multijunction photovoltaic devices." *Optics express* 22, no. 105 (2014): A1243-A1256.

[36] Chen, Q., G. Hubbard, Philip A. Shields, Chaowang Liu, Duncan WE Allsopp, Wang N. Wang, and S. Abbott. “Broadband moth-eye antireflection coatings fabricated by low-cost nanoimprinting.” *Applied Physics Letters* 94, no. 26 (2009): 263118.

[37] Clapham, P. B. and M. C. Hutley, “Reduction of Lens Reflexion by the “Moth Eye” Principle”, *Nature* 244 (1973): 281-282.

[38] Yee, K. “Numerical solution of initial boundary value problems involving Maxwell's equations in isotropic media.” *IEEE Transactions on antennas and propagation* 14, no. 3 (1966): 302-307.

[39] Chu, S. T., and S. K. Chaudhuri. “Finite-difference timedomain method for optical waveguide analysis.” *Progress in Electromagnetics Research* 11 (1995): 255-300.

[40] Conrad, B., T. Zhang, A. Lochtefeld, A. Gerger, C. Ebert, M. Diaz, L. Wang, I. Perez-Wurf, and A. Barnett. “Double layer antireflection coating and window optimization for GaAsP/SiGe tandem on Si.” in *Proceedings of 40th Photovoltaic Specialist Conference,* Denver, Colorado, 2014.

[41] Wikipedia, “Data center”, https://en.wikipedia.org/wiki/Data_center

[42] Shehabi, A., S. J. Smith, N. Horner, I. Azevedo, R. Brown, J. Koomey, E. Masanet, D. Sartor, M. Herrlin, W. Lintner, “United States Data Center Energy Usage Report.” Lawrence Berkeley National Laboratory, Berkeley, California. LBNL-1005775, 2016

[43] ANSI/ASHRAE/IES Standard 90.1-2016: Energy Standard for Buildings Except Low-Rise Residential Buildings.

[44] ASHRAE 2011: Gaseous and Particulate Contamination Guidelines for Data Centers.

[45] Lin, H. and G. S. Frankel. “Atmospheric corrosion of Cu by UV, ozone and NaCl” *Corrosion Engineering, Science and Technology* 48, no.6 (2013): 461-468

[46] Rice, D. W., P. Peterson, E. Be Rigby, P. B. P. Phipps, R. J. Cappell, and R. Tremoureux. “Atmospheric corrosion of copper and silver.” *Journal of the Electrochemical Society* 128, no. 2 (1981): 275-284.

[47] Salas, B.V., M. S. Wiener, R. Z. Koytchev, G. L. Badilla, R. R. Irigoyen, M. C. Beltran, N. R. Nedev, M. C. Alvarez, N. R. Gonzalez and J. M. B. Rull. “ Copper Corrosion by Atmospheric Pollutants in the Electronics Industry,” ISRN Corrosion, 2013.

[48] Wang, W. Q., A. Choubey, M. H. Azarian, and M. Pecht. “An assessment of immersion silver surface finish for lead-free electronics.” *Journal of electronic materials* 38, no. 6 (2009): 815-827.

[49] Kellner, R. "Alternative surface finishes – options and environmental considerations.", *Circuit World*, vol. 30 issue 2 (2004): 30-33

[50] Zhang, S. N., M. Osterman, A. Shrivastava, R. Kang, and M. G. Pecht. "The Influence of H_2S Exposure on Immersion-Silver-Finished PCBs Under Mixed-Flow Gas Testing." *IEEE transactions on device and materials reliability* 10, no. 1 (2010): 71.

[51] Xu, C., J. Smetana, J. Franey, G. Guerra, D. Fleming, W. Reents, D. Willie, A. Garcia, G. Encinas, and X. D. Jiang. "Creep corrosion of PWB final finishes: Its cause and prevention." in *Proceedings of IPC APEX Expo*, Las Vegas, NV, 2009.

[52] Zhang, S. N., R. Kang, A. Shivastava, M. Osterman, and M. Pecht. "A method of reliability assessment on creep corrosion for immersion silver finished PCBs." in *Proceedings of 8th International Conference on Reliability, Maintainability and Safety*, Chengdu, China, 2009.

[53] Schueller, R. "Creep corrosion on lead-free printed circuit boards in high sulfur environments." *Journal of Surface Mount Technology* 21, no. 1 (2008): 21.

[54] Franey, J. P., G. W. Kammlott, and T. E. Graedel. "The corrosion of silver by atmospheric sulfurous gases." *Corrosion science* 25, no. 2 (1985): 133-143.

[55] Graedel, T. E. "Corrosion mechanisms for silver exposed to the atmosphere." *Journal of the Electrochemical Society* 139, no. 7 (1992): 1963-1970.

[56] Liang, D., H. C. Allen, G. S. Frankel, Z. Y. Chen, R. G. Kelly, Y. Wu, and B. E. Wyslouzil. "Effects of sodium chloride particles, ozone, UV, and relative humidity on atmospheric corrosion of silver." *Journal of the electrochemical society* 157, no. 4 (2010): C146-C156.

[57] ISA-71.04-2013, "Environmental Conditions for Process Measurement and Control Systems: Airborne Contaminants," 2013.

[58] Singh, P., L. Klein, D. Agonafer, J. M. Shah, and K. D. Pujara. "Effect of Relative Humidity, Temperature and Gaseous and Particulate Contaminations on Information Technology Equipment Reliability" in *Proceedings of the ASME 2015 International Technical Conference and Exhibition on Packaging and Integration of Electronic and Photonic Microsystems and ASME 2015 13th International Conference on Nanochannels, Microchannels, and Minichannels InterPACKICNMM*, San Francisco, CA, 2015.

[59] ASTM B809-95 "Standard Test Method for Porosity in Metallic Coatings by Humid Sulfur Vapor", 2008

[60] Hindin, B., J. Fernandez. “Testing of Conformal Coatings Using The Flowers of Sulfur Test”, in *Proceedings of Tri-Service Corrosion Conference*, Las Vegas, Nevada, 2003.

[61] Cole, M., L. Hedlund, G. Hutt, T. Kiraly, L. Klein, S. Nickel, P. Singh, and T. Tofil. “Harsh environment impact on resistor reliability.” in *Proceedinsg of SMTA International*, Rosemont, IL, 2010.

[62] Abbott, W. H. “The development and performance characteristics of mixed flowing gas test environment.” *IEEE Transactions on Components, Hybrids, and Manufacturing Technology* 11, no. 1 (1988): 22-35.

[63] Telcordia Technologies Generic Requirements GR-63-CORE, “NEBS TM Requirements : Physical Protection.” 2006.

[64] Derkits, G. E., J. P. Franey, and W. D. Reents. “Biased mixed flowing gas testing for world class reliability.” *Bell Labs Technical Journal* 11, no. 3 (2006): 105-120.

[65] Demirkan, K., G. E. Derkits, D. A. Fleming, J. P. Franey, K. Hannigan, R. L. Opila, J. Punch, W.D. Reents, M. Reid, B. Wright and C. Xu, “Corrosion of Cu under highly corrosive environments.” *Journal of the Electrochemical Society* 157, no. 1 (2010): C30-C35.

[66] Coles, H.C., T. Han, P. N. Price, A. J. Gadgil and W. F. Tschudi, “Air Corrosivity in U.S. Outdoor-Air-Cooled Data Centers is Similar to That in Conventional Data Centers.” Department of Energy (EERE), March 2011 Rev.

[67] Franey, J. P., G. W. Kammlott, and T. E. Graedel. “The corrosion of silver by atmospheric sulfurous gases.” *Corrosion science* 25, no. 2 (1985): 133-143.

[68] Franey, J. P. “A novel system for atmospheric corrosion experiments.” *Corrosion Science* 23, no. 1 (1983): 1-8.

[69] Belanger, J. and J. Cox, “Gas Monitoring Solutions-Beyond Basic Compliance,” Honeywell, 2009.

[70] Yuan, B., D. A. Flemming, H. Rubin, R. Popowich, R. L. Opila and C. Xu. “Effects of Cl_2, NO_2, RH and temperature on accelerated Silver and Copper corrosion in mixed flowing gas test” in *Proceedings of SMTA International*, Rosemont, IL, 2017.

[71] ASTM B810-01a “Standard Test Method for Calibration of Atn
Test Chambers by Change in Mass of Copper Coupons,” 2011.

[72] Barbour, J. C., J. P. Sullivan, M. J. Campin, A. F. Wright, N. A. Missert, J. W. Braithwaite, K. R. Zavadil, N. R. Sorensen, S. J. Lucero, W.G. Breiland and H. K. Moffat. "Mechanisms of atmospheric copper sulfidation and evaluation of parallel experimentation techniques." No. SAND2002-0699. Sandia National Labs, Albuquerque, NM (US); Sandia National Labs., Livermore, CA (US), 2002.

[73] Chen, Z. Y., D. Liang, G. Ma, G. S. Frankel, H. C. Allen, and R. G. Kelly. "Influence of UV irradiation and ozone on atmospheric corrosion of bare silver." *Corrosion Engineering, Science and Technology* 45, no. 2 (2010): 169-180.

[74] Lin, H., G. S. Frankel, and W. H. Abbott. "Analysis of Ag corrosion products." *Journal of the Electrochemical Society* 160, no. 8 (2013): C345-C355.

[75] Sharma, S. P. "Reaction of copper and copper oxide with H_2S." *Journal of The Electrochemical Society* 127, no. 1 (1980): 21-26.

[76] ASTM B285-97 "Standard Test Method for Coulometric Reduction of Surface Films on Metallic Test," 2002.

[77] Kim, H. "Corrosion process of silver in environments containing 0.1 ppm H_2S and 1.2 ppm NO_2." *Materials and Corrosion* 54, no. 4 (2003): 243-250.

[78] Lambert, R. H. and D. J. Trevoy. "Analysis of Films on Copper by Coulometric Reduction." *Journal of the Electrochemical Society* 105, no. 1 (1958): 18-23.

[79] Rickett, B. I., and J. H. Payer. "Composition of copper tarnish products formed in moist air with trace levels of pollutant gas: sulfur dioxide and sulfur dioxide/nitrogen dioxide." *Journal of The Electrochemical Society* 142, no. 11 (1995): 3713-3722.

[80] Nakayama, S., T. Kaji, M. Shibata, T. Notoya, and T. Osakai. "Which is easier to reduce, Cu_2O or CuO?" *Journal of The Electrochemical Society* 154, no. 1 (2007): C1-C6.

[81] Wikipedia, "Computer memory", https://en.wikipedia.org/wiki/Computer_memory

[82] Yu, S. M., and P. Y. Chen. "Emerging memory technologies: Recent trends and prospects." *IEEE Solid-State Circuits Magazine* 8, no. 2 (2016): 43-56.

[83] Zhu, J. G. "Magnetoresistive random access memory: The path to competitiveness and scalability." *Proceedings of the IEEE* 96, no. 11 (2008): 1786-1798.

[84] Wong, H. S., S. Raoux, S. B. Kim, J. Liang, J. P. Reifenberg, B. Rajendran, M. Asheghi, and K. E. Goodson. "Phase change memory." *Proceedings of the IEEE* 98, no. 12 (2010): 2201-2227.

[85] Wong, H. S., H. Y. Lee, S. M. Yu, Y. S. Chen, Y. Wu, P. S. Chen, B. Lee, F. T. Chen, and M. J. Tsai. "Metal–oxide RRAM." *Proceedings of the IEEE* 100, no. 6 (2012): 1951-1970.

[86] Wikipedia "Tunnel magnetoresistance", https://en.wikipedia.org/wiki/Tunnel_magnetoresistance

[87] Heidecker, J. "MRAM technology status." Jet propulsion lab, Pasadena, CA, 2013.

[88] Takahashi, S., T. Kai, N. Shimomura, T. Ueda, M. Amano, M. Yoshikawa, E. Kitagawa, Y. Asao, S. Ikegawa, T. Kishi, H. Yoda, K. Nagahara, T. Mukai, H. Hada. "Ion-beam-etched profile control of MTJ cells for improving the switching characteristics of high-density MRAM." *IEEE transactions on magnetics* 42, no. 10 (2006): 2745-2747.

[89] Kinoshita, K., H. Utsumi, K. Suemitsu, H. Hada, and T. Sugibayashi. "Etching magnetic tunnel junction with metal etchers." *Japanese Journal of Applied Physics* 49, no. 8S1 (2010): 08JB02.

[90] Park, I. H., S. R. Min, W. H. Park, K. H. Shin, and C. W. Chung. "Nanometer-sized etching of magnetic tunnel junction stack for magnetic random access memory." *Journal of Magnetism and Magnetic Materials* 304, no. 1 (2006): e264-e266.

[91] Kim, E. H, Y. B. Xiao, S. M. Kong, and C. W. Chung. "Investigation on etch characteristics of nanometer-sized magnetic tunnel junction stacks using a HBr/Ar plasma." *Journal of nanoscience and nanotechnology* 11, no. 7 (2011): 6616-6620.

[92] Min, S. R., H. N. Cho, K. W. Kim, Y. J. Cho, S. H. Choa, and C. W. Chung. "Etch characteristics of magnetic tunnel junction stack with nanometer-sized patterns for magnetic random access memory." *Thin Solid Films* 516, no. 11 (2008): 3507-3511.

[93] Liu, X. Y., D. Mazumdar, W. Shen, B. D. Schrag, and G. Xiao. "Thermal stability of magnetic tunneling junctions with MgO barriers for high temperature spintronics." *Applied physics letters* 89, no. 2 (2006): 023504.

[94] Jung, K. B., J. Marburger, F. Sharifi, Y. D. Park, E. S. Lambers, and S. J. Pearton. "Long term stability of dry etched magnetoresistive random access memory elements." *Journal of Vacuum Science & Technology A: Vacuum, Surfaces, and Films* 18, no. 1 (2000): 268-272.

[95] Garay, A. A., J. H. Choi, S. M. Hwang, and C. W. Chung. "Inductively coupled plasma reactive ion etching of magnetic tunnel junction stacks in a CH_3COOH/Ar gas." *ECS Solid State Letters* 4, no. 10 (2015): P77-P79.

[96] Matsui, N., K. Mashimo, A. Egami, A. Konishi, O. Okada, and T. Tsukada. “Etching characteristics of magnetic materials (Co, Fe, Ni) using CO/NH_3 gas plasma for hardening mask etching.” *Vacuum* 66, no. 3 (2002): 479-485.

[97] Kim, E. H., T. Y. Lee, and C. W. Chung. “Evolution of etch profile of magnetic tunnel junction stacks etched in a CH_3OH/Ar plasma.” *Journal of The Electrochemical Society* 159, no. 3 (2012): H230-H234.

[98] Kinoshita, K., H. Honjo, S. Fukami, H. Sato, K. Mizunuma, K. Tokutome, M. Murahata, S. Ikeda, S. Miura and N. Kasai. “Process-induced damage and its recovery for a CoFeB–MgO magnetic tunnel junction with perpendicular magnetic easy axis.” *Japanese Journal of Applied Physics* 53, no. 10 (2014): 103001.

[99] Kanarik, K. J., T. Lill, E. A. Hudson, S. Sriraman, S. Tan, J. Marks, V. Vahedi, and R. A. Gottscho. “Overview of atomic layer etching in the semiconductor industry.” *Journal of Vacuum Science & Technology A: Vacuum, Surfaces, and Films* 33, no. 2 (2015): 020802.

[100] Suntola, T., J. Antson, Method for producing compound thin films, Patent 4058430, November 15, 1977.

[101] Suntola, T. “Atomic layer epitaxy.” *Thin Solid Films* 216, no. 1 (1992): 84-89.

[102] George, S. M. “Atomic layer deposition: an overview.” *Chem. Rev* 110, no. 1 (2010): 111-131.

[103] Leskelä, M., and M. Ritala. “Atomic layer deposition (ALD): from precursors to thin film structures.” *Thin solid films* 409, no. 1 (2002): 138-146.

[104] Oehrlein, G. S., D. Metzler, and C. Li. “Atomic layer etching at the tipping point: an overview.” *ECS Journal of Solid State Science and Technology* 4, no. 6 (2015): N5041-N5053.

[105] Park, S. D., K. S. Min, B. Y. Yoon, D. H. Lee, and G. Y. Yeom. “Precise depth control of silicon etching using chlorine atomic layer etching.” *Japanese journal of applied physics* 44, no.1R (2005): 389.

[106] Tan, S., W. B. Yang, K. J. Kanarik, T. Lill, V. Vahedi, J. Marks, and R. A. Gottscho. “Highly selective directional atomic layer etching of silicon.” *ECS Journal of Solid State Science and Technology* 4, no. 6 (2015): N5010-N5012.

[107] Ko, K. K., and S. W. Pang. "Controllable layer-by-layer etching of III–V compound semiconductors with an electron cyclotron resonance source." *Journal of Vacuum Science & Technology B: Microelectronics and Nanometer Structures Processing, Measurement, and Phenomena* 11, no. 6 (1993): 2275-2279.

[108] Park, J. B., W. S. Lim, B. J. Park, I. H. Park, Y. W. Kim, and G. Y. Yeom. "Atomic layer etching of ultra-thin HfO_2 film for gate oxide in MOSFET devices." *Journal of Physics D: Applied Physics* 42, no. 5 (2009): 055202.

[109] Lim, W. S., J. B. Park, J. Y. Park, B. J. Park, and G. Y. Yeom. "Low Damage Atomic Layer Etching of ZrO_2 by Using BCl_3 Gas and Ar Neutral Beam." *Journal of nanoscience and nanotechnology* 9, no. 12 (2009): 7379-7382.

[110] Lee, Y. H., and S. M. George. "Atomic layer etching of Al_2O_3 using sequential, self-limiting thermal reactions with $Sn(acac)_2$ and hydrogen fluoride." *ACS nano* 9, no. 2 (2015): 2061-2070.

[111] Lee, Y. H., J. W. DuMont, and S. M. George. "Atomic layer etching of HfO_2 using sequential, self-limiting thermal reactions with $Sn(acac)_2$ and HF." *ECS Journal of Solid State Science and Technology* 4, no. 6 (2015): N5013-N5022.

[112] Zywotko, D. R., and S. M. George. "Thermal Atomic Layer Etching of ZnO by a "Conversion-Etch" Mechanism Using Sequential Exposures of Hydrogen Fluoride and Trimethylaluminum." *Chemistry of Materials* 29, no. 3 (2017): 1183-1191.

[113] Lee, Y. H., C. Huffman, and S. M. George. "Selectivity in Thermal Atomic Layer Etching Using Sequential, Self-Limiting Fluorination and Ligand-Exchange Reactions." *Chemistry of Materials* 28, no. 21 (2016): 7657-7665.

[114] Igumenov, I. K., T. V. Basova, and V. R. Belosludov. "Volatile precursors for films deposition: vapor pressure, structure and thermodynamics." in *Application of Thermodynamics to Biological and Materials Science*, InTech, 2011.

[115] Putkonen, M., A. Szeghalmi, E. Pippel, and M. Knez. "Atomic layer deposition of metal fluorides through oxide chemistry." *Journal of Materials Chemistry* 21, no. 38 (2011): 14461-14465.

Appendix

COPYRIGHT PERMISSIONS

Reprint permission of figure 3.5, 3.6, 3.16, 3.17, 3.18 and 3.19.

ECS Advancing solid state and electrochemical science and technology

Journal of The Electrochemical Society

HOME | CURRENT ISSUE | FOCUS ISSUES | ARCHIVE | COLLECTIONS | SUBSCRIBE | HELP | FEEDBACK

User Name
Password
LOG-IN

ECS Digital LIBRARY

Search for Keyword: Go
Advanced Search

ECS Copyright and Permissions

NOTICE: Beginning Monday, April 10, 2017, ECS has partnered with the Copyright Clearance Center (CCC) in order to manage permission requests.

- This service will allow authors to immediately receive permission, and will eliminate the need to complete ECS's permission request form.
- As of Monday, April 10, 2017, ECS will no longer accept permission request forms through email. All future requests must be made through CCC.
- Please note that there may be fees involved, depending on the type of material and reuse requested.
- **As has always been ECS's policy, authors are NOT required to request permission to reproduce their own figures or tables.**

Before requesting permission, please confirm the open access status of the article. **ECS does not hold the copyright on the open access articles published in its journals.** Please follow reuse instructions given by Creative Commons for its various licenses.

Latest Articles

Volume 165, Issue 4, 2018

Alert me to new issues of J. Electrochem. Soc.

ABOUT ECS

ABOUT THIS JOURNAL / EDITORIAL BOARD

SUBSCRIPTION INFORMATION

Reprint permission of figure 3.3, 3.4, 3.8, 3.9, 3.11, 3.12, 3.13, 3.14 and 3.15.

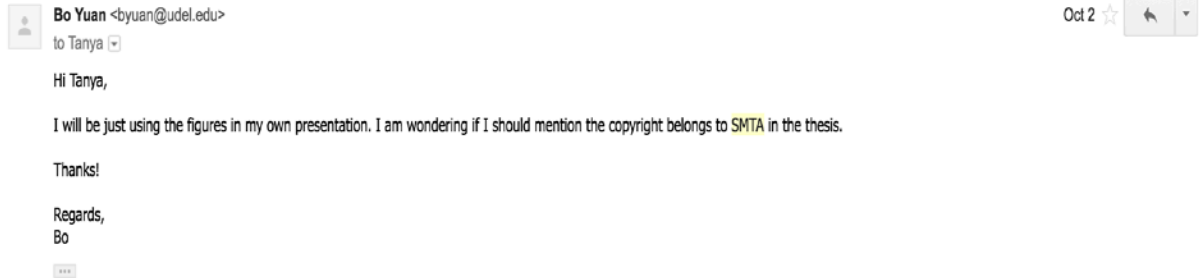
Bo Yuan <byuan@udel.edu> Oct 2

to Tanya

Hi Tanya,

I will be just using the figures in my own presentation. I am wondering if I should mention the copyright belongs to SMTA in the thesis.

Thanks!

Regards,
Bo

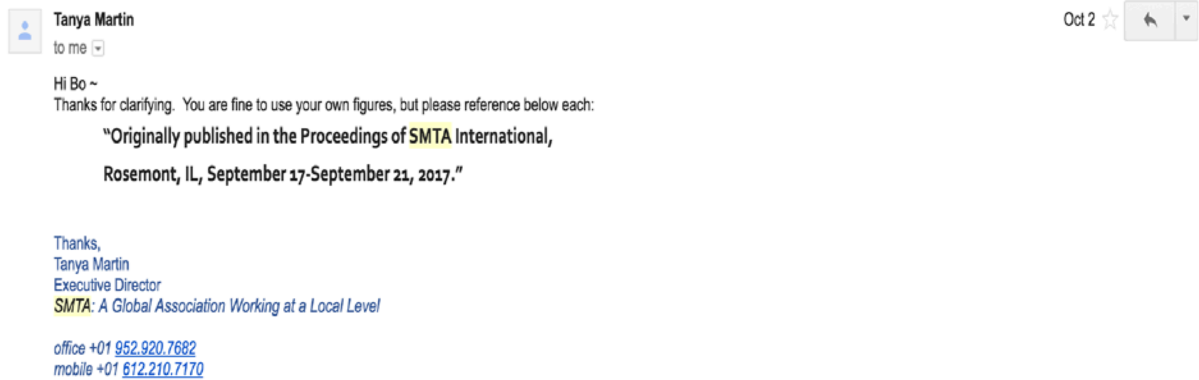
Tanya Martin Oct 2

to me

Hi Bo ~
Thanks for clarifying. You are fine to use your own figures, but please reference below each:

"Originally published in the Proceedings of SMTA International,

Rosemont, IL, September 17-September 21, 2017."

Thanks,
Tanya Martin
Executive Director
SMTA: A Global Association Working at a Local Level

office +01 952.920.7682
mobile +01 612.210.7170